Study of Muon-induced Single Event Upsets in SRAMs and their Fundamental Physical Process

真鍋, 征也

https://hdl.handle.net/2324/4475179

出版情報：Kyushu University, 2020, 博士（工学）, 課程博士
バージョン：
権利関係：

Study of Muon-induced Single Event Upsets in SRAMs and their Fundamental Physical Process

Seiya Manabe
Department of Advanced Energy Engineering Science
Interdisciplinary Graduate School of Engineering Sciences
Kyushu University

February 2021

Contents

List of Figures

List of Tables

1 Introduction

1.1 Soft Error

A modern advanced information society is sustained by a large number of electric equipment. A major policy for the economy, society, and general public, called "Super Smart Society," is being strongly promoted by the Council for Science, Technology and Innovation; Cabinet Office, Government of Japan in the 5th Science and Technology Basic Plan [1]. A great amount of information will be collected and shared using the Internet-of-Things (IoT) technology with numerous sensors. Necessary products and services will be distributed to those who need them, and all will receive high-quality services and live a comfortable life. The number of IoT devices is expected to dramatically increase, as shown in Figure 1.1. Electric devices play an important role as an infrastructure in the modern and future society. Our society might face serious damage if something goes wrong with digital integrated circuits (ICs) built into the electric equipment. Supercomputers and data servers are required to provide a long-term and reliable operation. Moreover, human damages might occur if automatic control systems or medical equipment operate improperly. Therefore, the reliability and safety must be assessed and ensured in addition to performance improvement in electric devices.

The problem of soft errors [2] in very-large scale integrated (VLSI) circuits subjected to the terrestrial radiation environment is a major threat to the electronics used at the ground level. A radiation-induced soft error means a temporary malfunction in the VLSI circuits due to the single event upsets (SEUs) [3] caused by the transient signal induced by energetic ionizing radiation (e.g., resulting in an upset of memory information in static random-access memories (SRAMs)), as will be explained in Section 1.2. Such a soft error corrupts the data stored in the device, but does not damage the device itself. The device operation can be recovered by rebooting. The soft error problem is expected to become more obvious in future-technology devices.

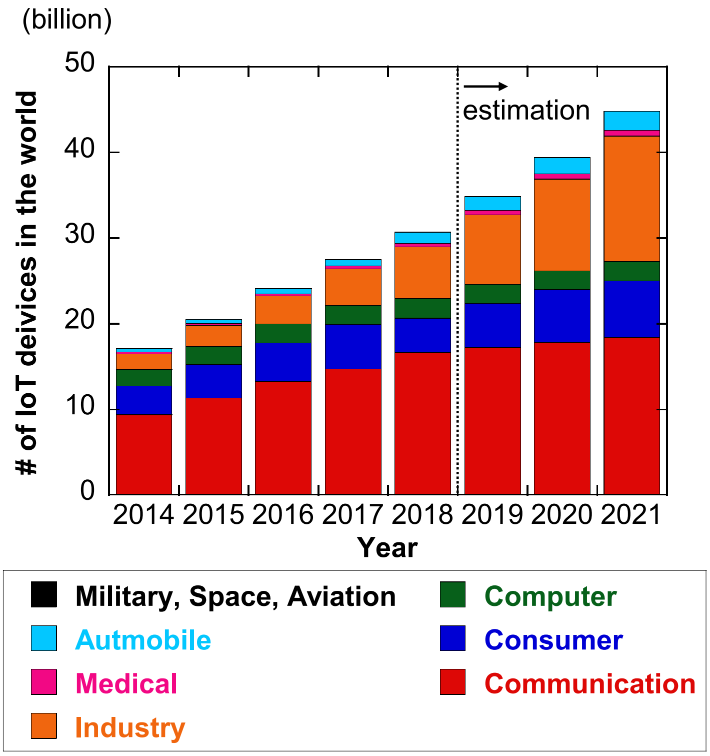

Figure 1.1: World market for Internet-connected devices. The data are taken from [4].

1.2 Mechanism of Single Event Upset

Figure 1.2 shows the physical process of a single event upset induced by a charged particle. When an energetically charged particle passes through a semiconductor, it interacts with the material in the semiconductor via the Coulomb force and transmits a large amount of energy to the orbital electrons. These electrons create electron-hole pairs along the incident particle path. In a semiconductor, a large amount of the deposited energy is thus converted to into many electron-hole pairs. Other particles, such as neutrons, do not ionize the matter along their passage. However, due to the probability of a nuclear reaction with the nuclei in the semiconductor devices, they can produce SEUs by indirect ionization. The deposited charge resulting from the indirect ionization is generated by the secondary ions from the nuclear reaction in the same manner as direct ionization. The deposited charges in or around the depletion layer are collected to the memory node. When the collected charge exceeds the critical charge (Q_c) defined as the minimum charge to induce the SEU, the state of the SRAM undergoes a change, that is, $0 \rightarrow 1$ or $1 \rightarrow 0$.

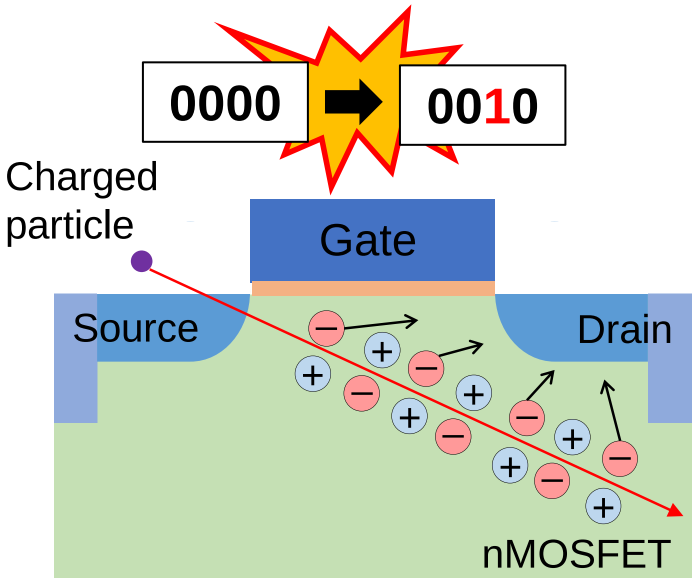

Figure 1.2: Schematic illustration of a single event upset induced by a charged particle.

1.3 Cosmic Rays at Ground Level

In a terrestrial environment, the secondary cosmic rays are recognized as a cause of soft errors. Figure 1.3 shows a schematic illustration of the generation process of secondary cosmic rays. The primary cosmic rays consist of high-energy proton, helium nuclei, and heavy ions, which come from all directions of deep space or the Sun. The interaction of primary cosmic rays with atomic nuclei in the Earth's upper atmosphere is the origin of secondary cosmic rays. The incident high-energy particle strikes a molecule in the air and produces a cascade of new particles. Each constituent of this secondary flux can consequently interact with air nuclei or decay according to its mean lifetime. A fraction of them eventually reaches the ground. Figure 1.4 shows typical energy spectra of secondary cosmic rays calculated by Excel-based program for calculating atmospheric cosmic-ray spectrum (EXPACS) [5–7].

A major component of secondary cosmic rays at the ground level is known as muons and its fraction is about three-quarter of the total cosmic-ray flux with the average kinetic energy of a few GeV. However, the effect of muons on soft errors has not been considered serious because only a small amount of energy is deposited in devices due to their small stopping power, and the deposited charge cannot exceed the Q_c. Until recently, the effect of cosmic-ray neutrons has been recognized as a major cause of soft errors because they can deposit sufficient charge to the small sensitive volumes of SRAMs through the nuclear reaction.

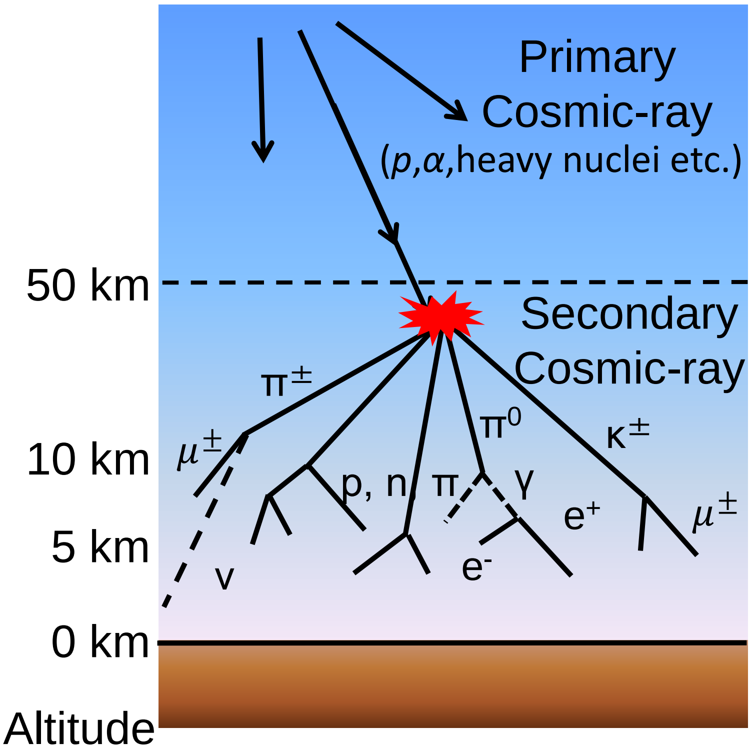

Figure 1.3: Generation process of the secondary cosmic rays.

1.4 Characteristic of Muons

1.4.1 Basic Properties of Muons

Muons are elementary particles classified together with electrons as lepton. The muon mass is 105.7 MeV/c^2, which is 207 times larger than the electron mass. Muons are classified into negatively charged muons (negative muons) and positively charged antiparticles (positive muons). Negative and positive muons are denoted by μ^- and μ^+, respectively. A muon is produced in the decay of the pion ($\pi^\pm$) or the kaon ($K^\pm$) according to:

$$\pi^+ \rightarrow \mu^+ + \nu_\mu, \tag{1.1}$$

$$\pi^- \rightarrow \mu^- + \overline{\nu_\mu}, \tag{1.2}$$

$$K^+ \rightarrow \mu^+ + \nu_\mu,$$

$$K^- \rightarrow \mu^- + \overline{\nu_\mu},$$

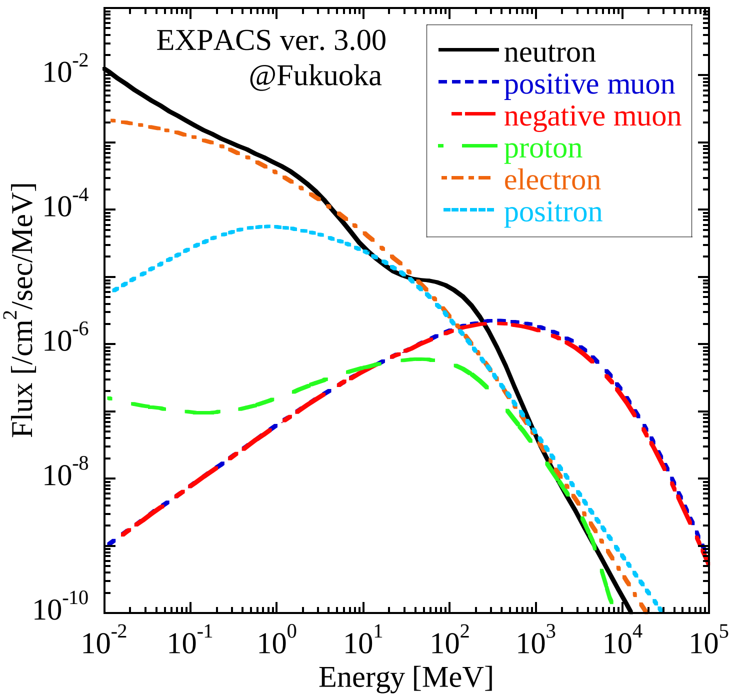

Figure 1.4: Energy spectra of the secondary cosmic rays at ground level. The spectrum was calculated with EXPACS [5–7].

where, ν_μ and $\overline{\nu_\mu}$ denote the muon and anti-muon neutrinos, respectively. Muons are unstable particles and decay into three particles with a mean lifetime of 2.2 μs:

$$\begin{aligned} \mu^+ &\to e^+ + \nu_e + \overline{\nu_\mu}, \\ \mu^- &\to e^- + \overline{\nu_e} + \nu_\mu, \end{aligned} \tag{1.3}$$

where ν_e and $\overline{\nu_e}$ denote the electron and anti-electron neutrinos, respectively. The cosmic-ray muons are produced at a high altitude in the atmosphere (typically 15 km). The range of muons with the speed of light is only 660 m in the mean lifetime of 2.2 μs; however, the lifetime of a high-energy muon is extended due to the special relativity theory. Hence, a large amount of muons can reach the ground level.

We use the momentum to express the muon kinetic energy in the following description. The relationship between the momentum P_μ and the kinetic energy

E_k is presented as follows:

$$P_\mu = \sqrt{2m_\mu E_k + E_k^2},$$
$$E_k = \sqrt{P_\mu^2 + m_\mu^2} - m_\mu, \tag{1.4}$$

where m_μ is the muon mass (= 105.7 MeV/c^2). Also, the relationship is shown in Fig. 1.5.

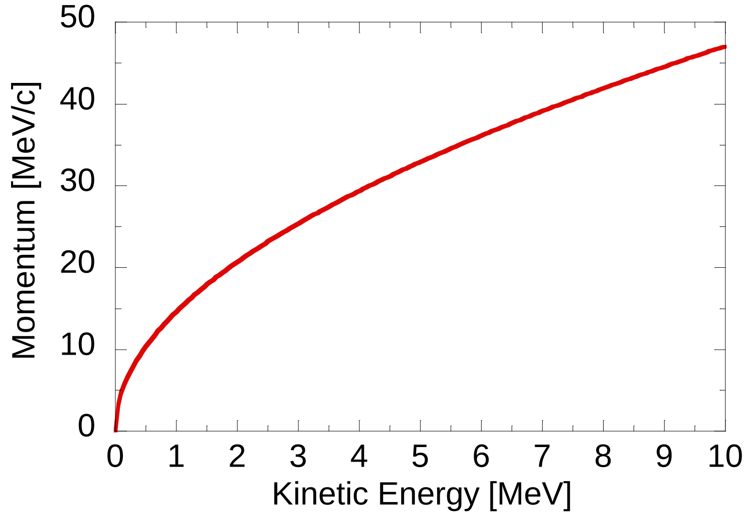

Figure 1.5: Relationship of muon momentum P_μ and kinetic energy E_k.

1.4.2 Negative Muon Capture Reaction

Figure 1.6 schematically shows the negative muon capture process. A muon passing through matter loses its kinetic energy by generating electron-hole pairs along the track. After losing the incident kinetic energy and stopping in matter, the positive muon decays into a positron and two neutrinos as shown in Eq. (1.3). On the contrary, the negative muon is captured by an atom in matter into high orbital momentum states, forming a *muonic atom*. Strictly speaking, when the muon velocity is less than that of the valence electrons, the negative muon can exchange energy with the valence electrons and rapidly stop in approximately 10^{-13} s. Once the muon reaches a state of zero kinetic energy, it is captured by the host atom into high orbital momentum states. The captured muon cascades down to the 1s orbital while emitting characteristic X-rays because all low-lying muonic states are unoccupied. A part of the captured negative muons decays into an electron and two neutrinos in the 1s orbital as shown in Eq. (1.3). The remaining negative muons are finally absorbed by the nucleus, and a highly excited nucleus is formed. Subsequently, the nucleus is de-excited by the emission of neutrinos, photons, neutrons, and other light ions. The muon captured in the nuclei is reviewed from the viewpoint of nuclear physics in [8]. When the negative muons stop in silicon, approximately 35% of them decay into electrons and neutrinos in the 1s orbital. The remaining muons are captured by the nucleus. Hence, the excited aluminum nucleus are produced, and the reaction is:

$$\mu^- +^{28}\text{Si} \rightarrow^{28}\text{Al}^* + \nu_\mu + 100.5\ \text{MeV}. \tag{1.5}$$

The capture reaction generates a heavy recoiled nucleus with the simultaneous emission of secondary light ions following the de-excitation modes of ^{28}Al:

$$\begin{aligned} ^{28}\text{Al}^* \quad &\rightarrow \quad ^{27}\text{Al} \ + \ n\ (12.4\ \text{MeV}) \\ &\rightarrow \quad ^{27}\text{Mg} \ + \ p\ (14.2\ \text{MeV}) \\ &\rightarrow \quad ^{24}\text{Na} \ + \ \alpha\ (15.5\ \text{MeV}) \\ &\rightarrow \quad ^{26}\text{Mg} \ + \ d\ (18.4\ \text{MeV}), \end{aligned} \tag{1.6}$$

where the energy listed with each final state is the ground state energy with respect to the ^{28}Si ground state. Measday expressed the global pattern of the capture reaction in percentage (Table 1.1) [8]. Figure 1.7 shows the energy spectra calculated by the Particle and Heavy Ion Transport Code System (PHITS) [9, 10] for the secondary light and heavy ions from the negative muon capture reaction in silicon. The H and He ions are energetically favored, while the heavy recoiled nuclei (i.e., Al, Mg and Na) have kinetic energies lower than 5 MeV. In Figure 1.8, the stopping power for muons is compared with that for the secondary ions as a function of the kinetic energy. All secondary ions have a much larger stopping power than muons; thus, the secondary ions are expected to deposit sufficient charge in the small sensitive volume of SRAMs to cause single event effects.

Table 1.1: Global pattern for the negative muon capture reactions in ^{28}Si [8].

Reaction	%	Reaction	%	Reaction	%	Reaction	%
$(\mu,\nu)^{28}$Al	26	$(\mu,\nu p)^{27}$Mg	2.0	$(\mu,\nu d)^{26}$Mg	3.1	$(\mu,\nu 2pn)^{25}$Na	0.1
$(\mu,\nu n)^{27}$Al	45	$(\mu,\nu pn)^{26}$Mg	4.9	$(\mu,\nu dn)^{25}$Mg	1.0	$(\mu,\nu\alpha)^{24}$Na	1.0
$(\mu,\nu 2n)^{26}$Al	12	$(\mu,\nu p2n)^{25}$Mg	1.4	$(\mu,\nu d2n)^{24}$Mg	0.3	$(\mu,\nu\alpha n)^{23}$Na	0.8
$(\mu,\nu 3n)^{25}$Al	1.0	$(\mu,\nu p3n)^{24}$Mg	0.6			$(\mu,\nu\alpha 2n)^{22}$Na	0.5
		$(\mu,\nu p4n)^{23}$Mg	0.1			$(\mu,\nu\alpha 3n)^{21}$Na	0.2
$\sum$(n)	84	$\sum$(p)	9.0	$\sum$(d)	4.4	$\sum$(Na)	2.6

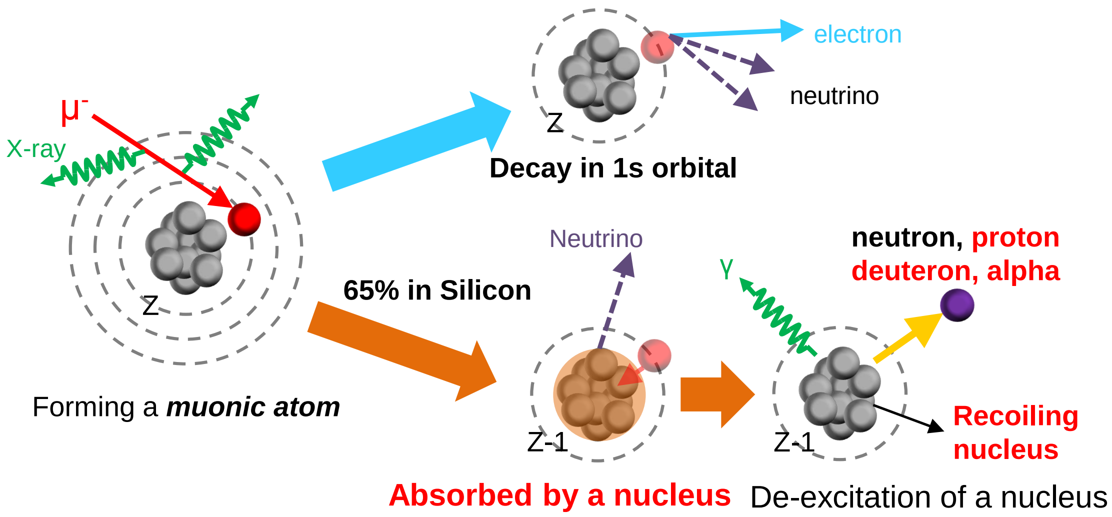

Figure 1.6: Schematic illustration of the negative muon capture process.

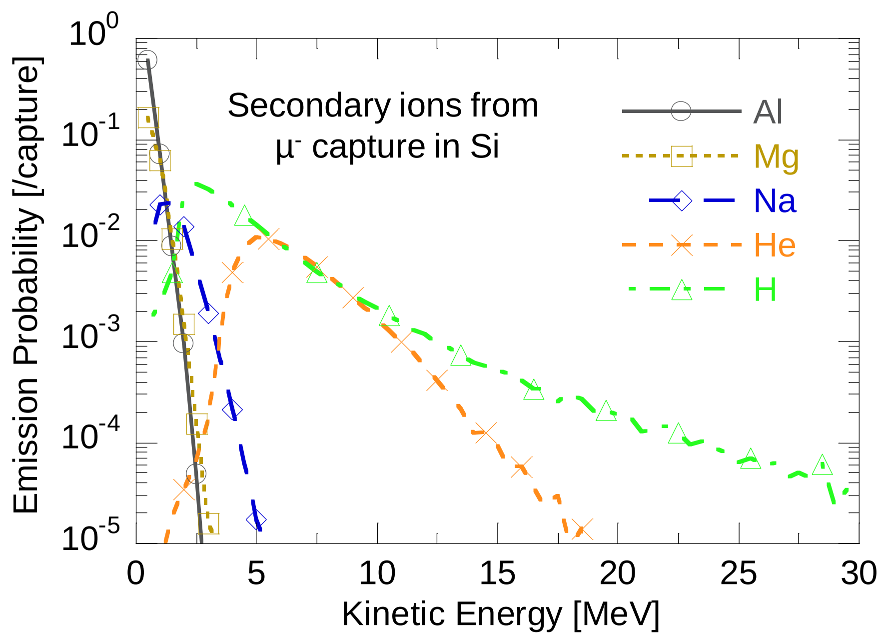

Figure 1.7: Calculated energy spectra of the secondary light and heavy ions from the negative muon capture reaction in silicon. The spectra were calculated with QMD [11] plus GEM [12] implemented in PHITS [9].The H ion represents the sum of proton, deuteron and triton. The He ion represents the sum of alpha particle and He-3.

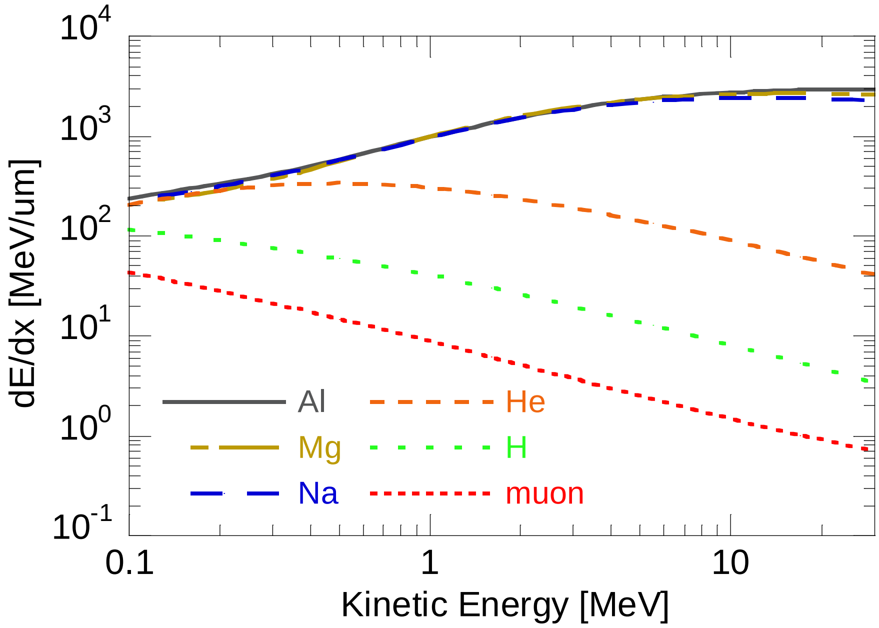

Figure 1.8: Stopping power (dE/dx) for muons and secondary ions in silicon as a function of the kinetic energy calculated using the SRIM code [13].

1.5 Previous Works

As mentioned in Section 1.3, neutrons are recognized as a major threat for the soft error at the ground level, and a large number of works on neutron-induced soft errors have been performed [14]. The standard for neutron-induced soft error rate testing of ICs has been established by JEDEC Solid State Technology Association [15]. International Telecommunication Union defined the test method for telecommunication equipment [16]. More recently, Nippon Telegraph and Telephone Corporation started the neutron-induced soft error test service [17]. The test service reproduces soft errors in any devices by irradiating equipment under test with neutrons to measure the equipment's resilience against soft errors in the real world. Thus, the neutron-induced soft error has been investigated well, and the test method has been practically implemented.

The pioneer work on the muon-induced soft error was performed by Ziegler and Lanford in 1979 [18]. They provided a survey of the effects of cosmic rays on the typical computer memory circuits at that time and investigated the relative contribution to the error rate, including the effects of the electrons, muons, protons, and neutrons by considering the direct ionization, recoils, and capture. Moreover, they predicted that devices would be susceptible to the direct ionization of cosmic-ray muons because of the dramatic decrease of Q_c. After this excellent survey work, Dicello et al. published a series of papers on the experimental investigations on muon- and pion-induced soft error and contribution of cosmic-ray muons and pions to the sea level soft error rate [19–22]. The irradiation experiments were performed at the LAMPF [23] facility in the 1980s. In [19], negative and positive muon beams with the momentum of 109 MeV/c were irradiated on the 4K NMOS SRAM. The positive muon with the fluence of 4×10^{11} cm^{-2} produced only three errors. Moreover, the negative muon beam with the fluence of 8×10^{10} cm^{-2} produced no errors. The observed errors were due to the pion contamination. In [20], 4K NMOS, 16K NMOS and 64K NMOS/complementary metal oxide semiconductor (CMOS) SRAMs were tested with a 90 MeV/c positive muon beam. However, only two errors were observed in 4K NMOS under the positive muon irradiation with the fluence of 1.4×10^{10} cm^{-2}. Dicello et al. provided an estimate of the SEU rate at sea level and 10 km based on the experiment result in [22]. An NMOS SRAM was irradiated, and the effects of the stopping negative and positive muons on the SEUs were investigated. Based on this experiment, the soft error rate induced by stopping muon was estimated at only 2% of the total rate from all species.

To sum up the previous works in the 1980s, only a few errors were observed during muon irradiation because the beam intensity was not enough, and the critical charge of the devices used in the irradiation tests was relatively high compared to that of modern devices. The experimental data have a large uncertainty due to a lack of statistics.

For a while after the works performed in the 1980s, the effect of cosmic-ray muons on soft errors had not been considered serious because only a small amount of energy is deposited in devices due to their small stopping power, and the deposition charge cannot exceed the critical charge. In the recent years, a progressive reduction in the radiation tolerance on soft errors has become evident because the critical charge was decreased by the miniaturization and low voltage operation of circuits. Thus, a muon-induced soft error is drawing attention again, and several papers have been published [24–29] from 2010. A series of muon-induced SEU experiments were performed by Sierawski et al. [24–26] using low-energy positive muon beams at the TRIUMF and the RIKEN-Rutherford Appleton Laboratory (RAL) facility. They demonstrated the effects of muon direct ionization for bulk SRAMs of different technology nodes (i.e., 65, 55, 45, and 40 nm). Figure 1.9 shows the their experimental results at TRIUMF [24]. The kinetic energy dependence of the SEU probability had peak around a certain kinetic energy (700 keV in their experiment) which the Brag peak of the muons was close to the SRAM sensitive volumes, and the sufficient charge was deposited in the volumes (Figure 1.9a). The SEU probability increased with the reducing the supply voltage due to the reduction of the critical charge (Figure 1.9b). Similar SEU experiments with a low-energy positive muon beam were conducted at TRIUMF: 28-nm UTBB FDSOI and bulk SRAMs [27] and SRAMs built on 32-nm planar and 22- and 14-nm 3D Tri-Gate technologies [28]. Their experimental results [27, 28] showed the advantage of the FD-SOI and 3D Tri-Gate technologies with respect to tolerance on muon-induced SEUs.

A numerical simulation on 65-nm SRAMs was recently performed by Serre et al. [29]. The impact of low-energy negative muons on SRAMs was studied from the physical point-of-view and investigated using the TIARA code fully rewritten using the Geant4 toolkit. In the simulation, the negative muon with the kinetic energy under 1 MeV was incident on the 65-nm SRAM. Figure 1.10 shows their simulation result in Figure 5 of [29]. Their result showed that negative muons with energies around 0.4 MeV can be stopped and captured in the vicinity of the sensitive volumes of SRAMs. The soft error rate then became a peak. Thus, the residual heavy nucleus and light particles generated by negative muon capture reactions significantly caused SEUs if muons are stopped and captured by the nuclei near the sensitive drain region.

1.6 Muon Experimental Facilities

As mentioned in Section 1.5, positive muon irradiation tests were performed at two accelerator facilities, namely TRIUMF and RIKEN-RAL. The number of muon facilities is limited, and only five muon facilities have been built worldwide (Table 1.2). Japan has two facilities: Muon Science Establishment (MUSE) in Japan Proton Accelerator Complex (J-PARC) [30, 31] and Muon Science Innovation Channel (MuSIC) in Research Center for Nuclear Physics (RCNP) [32]. Muon beams with different time structures, namely pulsed and direct current (DC) beams, are available at MUSE and MuSIC, respectively. Figure 1.11 illustrates the time structures of the muon beams available at the two facilities. At MUSE, muons are bunched in a pulse with a full width of 100-130 ns [30]. The repetition rate of the pulse is 25 Hz. The beam flux of the decay muon is approximately 10^6-10^7/s. The most intensive pulsed muon beam in the world is available at MUSE. However, measuring the phenomena that occur in a short time ($\sim$100 ns) after muons stop in targets, such as muonic X-ray and particle emission from nuclear reaction, using the pulsed muon beam is difficult because a pile-up of the signals from the detectors happens due to a large number of muons being bunched in a pulse. In contrast, a DC muon beam is available at MuSIC. A single muon flies continuously with a repetition rate of 10-100 μs. The beam intensity is 10^4-10^5/sec at a proton current of 1 μA used for muon generation [32]. At the DC muon beam, the physical event in a detector caused by a single muon is easily detected by ap-

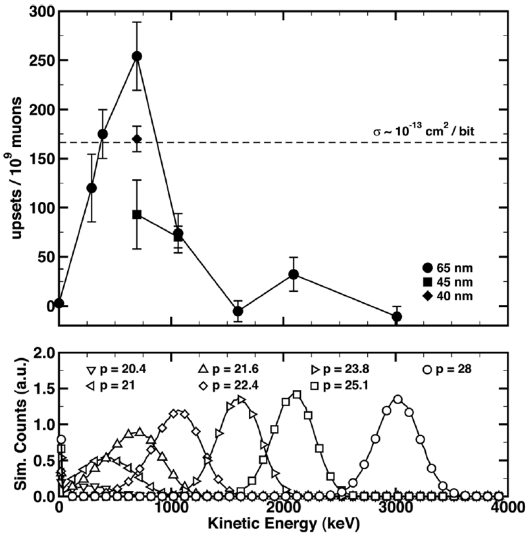

(a) Energy dependence for the 65, 45 and 40 nm SRAMs

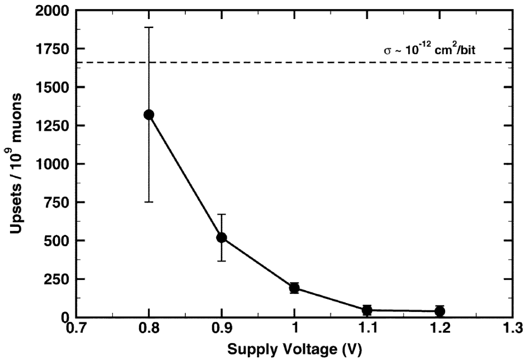

(b) Supply operation voltage dependence for a 65 nm SRAM

Figure 1.9: Measured positive muon-induced SEU probabilities as the functions of (a) the kinetic energy and (b) the supply voltage. The figures are taken from Figures 4 and 5 in [24]. The kinetic energy dependence (a) was measured with an operation voltage of 1.0 V. A top and bottom figures of (a) show the kinetic energy dependence of the SEU probability and the muon kinetic energy distributions in the cases of several momenta irradiation, respectively. The supply voltage dependence (b) was measured under the approximately 400 keV muon irradiation (21 MeV/c momentum selection).

plying a gate generated from an incoming muon. Therefore, phenomena, such as muonic X-ray and particle emission from nuclear reaction, can be more easily measured compared to a measurement with a pulsed beam.

In this work, two experiments were performed at different facilities. An irradiation test for the SRAM device was performed at MUSE using an intensive muon beam available at MUSE, as described in Chapter 2. In Chapter 4, the experimental data of an important fundamental physical process of muon-induced soft error were measured at MuSIC by taking an advantage of the DC muon beam.

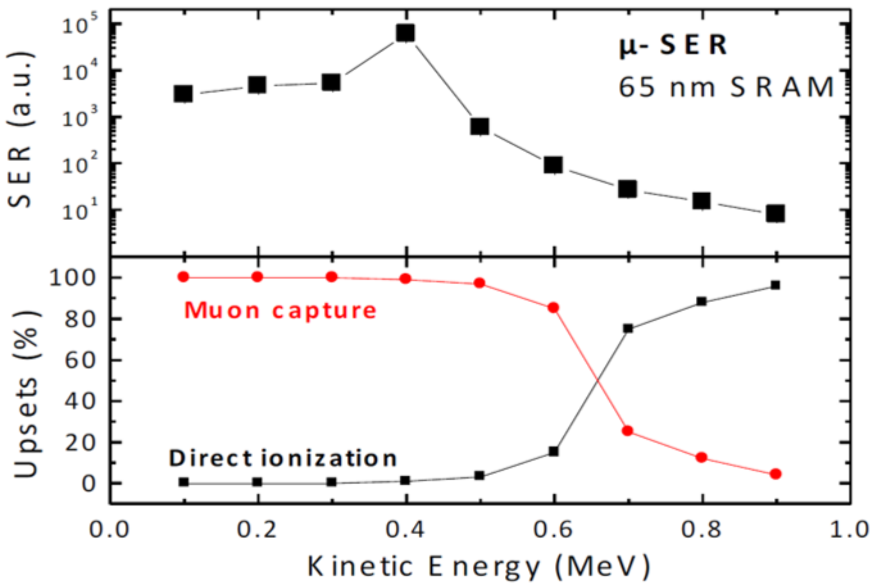

Figure 1.10: Estimated mono-energetic negative muon-induced soft error rate on the 65-nm SRAM as a function of the kinetic energy (upper). Percentage of the SEU induced by the secondary ions from the negative muon capture reaction by nuclei or muon direct ionization (lower). The figure is taken from Figure 5 in [29].

Table 1.2: Muon experimental facilities in the world.

Name	Location	Beam type
RIKEN-RAL	United Kingdom	Pulse
PSI	Switzerland	DC
TRIUMF	Canada	DC
J-PARC MUSE	Japan	Pulse
RCNP-MuSIC	Japan	DC

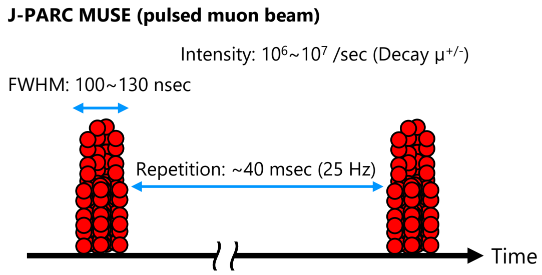

(a) J-PARC MUSE

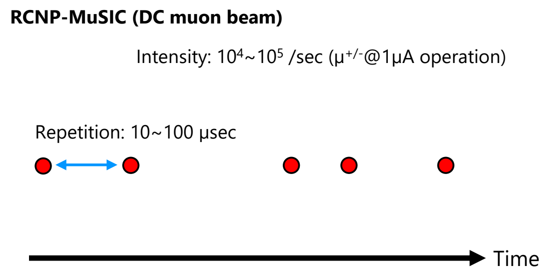

(b) RCNP-MuSIC

Figure 1.11: Schematic illustration of the time structure of the muon beams at (a) J-PARC MUSE and (b) RCNP-MuSIC. The beam characteristics shown in each figure are taken from [30] and [32].

1.7 Objective

As mentioned earlier, the cosmic-ray muon is drawing attention as a new cause of soft error at the ground level, and many works have been reported. However, the negative muon-induced soft error is not well understood. The nuclear negative muon capture reaction is expected to have a significant effect on the occurrence of SEUs with only the simulation [29]. The experimental investigation on the capture reaction-induced SEUs is insufficient.

Considering these circumstances, the effect of the muons on the soft error was investigated herein with both experiments and simulations, with particular attention to the negative muon. Furthermore, the experimental data of the nuclear negative muon capture reaction were accumulated to improve simulation-based estimations of muon-induced soft errors at the ground level. The purposes of this work are as follows:

- to experimentally investigate the effect of the secondary particles emitted from the nuclear negative muon capture reaction on the SEU occurrence by measuring the negative and positive muon-induced SEU cross-section for a 65-nm SOTB SRAM;
- to estimate the negative and positive muon-induced SEU rates at the ground-level radiation environment by means of a simulation based on the experimental SEU data; and
- to measure the energy spectra of the secondary ions from the nuclear negative

muon capture reaction on the silicon nucleus, which is the main constituent element of semiconductor devices, to benchmark the theoretical model.

This thesis is composed of five parts, including this introduction. Chapter 2 is devoted to a work on the experimental investigation of the negative muon-induced soft error. Chapter 3 presents the experimental data analyzed with a simulation and the estimated muon-induced SEU rates. Chapter 4 describes the measurement of the experimental data of the nuclear negative capture reaction. Chapter 5 provides the summary and conclusions.

2 Measurement of SEU Cross-sections for the 65-nm UTBB-SOI SRAM

2.1 Introduction

As mentioned in Chapter 1, many works are devoted to the muon-induced soft error from 2010. The positive muon irradiation tests for the several technologies SRAM were performed to investigate the direct ionization effect of muons on the SEU [24–28]. In contrast, no negative muon irradiation test with modern devices has been reported until now. In a recent numerical simulation on 65-nm SRAMs, Serre et al. [29] showed that the residual heavy nucleus and light particles generated by the negative muon capture reactions significantly cause SEUs if the muons are stopped and captured by the nuclei near the sensitive drain region. Thus, negative muon irradiation tests are needed for reliable simulation-based estimations of muon-induced soft errors at the ground level.

Under these circumstances, this work performs a series of irradiation experiments with both "positive" and "negative" muon beams at the Muon Science (MUSE) Facility [30, 31], in the Materials and Life Science Experimental Facility of the Japan Proton Accelerator Research Complex (J-PARC). The SEU cross-sections for the 65-nm UTBB-SOI SRAMs were measured as a function of the incident muon kinetic energy and the operating supply voltage. The main purpose of this experiment was to investigate the effect of negative muon capture reactions on SEUs by a comparison with positive muon-induced SEUs through measurement.

2.2 Experiment

2.2.1 Muon Science Facility

This subsection introduces the accelerator facility used for our experiment. The accelerator complex of J-PARC was constructed in the south part of the Tokai-JAEA site. The facility consists of a 400-MeV LINAC and 3 and 50 GeV proton synchrotron rings (2.1) [33]. Approximately 90% of the 3 GeV proton beam was sent to the Material and Life Science Facility (MLF) for the production of intense pulsed muon and neutron beams.

The Muon Science Facility (MUSE) [30, 31] is located in the MLF building. Figure 2.2 shows a layout of the muon beam lines in the MUSE. The experiment was performed in one superconducting decay/surface muon channel, called the D-line. The primary proton beam was bombarded on a graphite target to generate pions through proton-proton or proton-neutron reactions in the carbon nucleus. A quadrupole triplet was used to capture the pions into the beam line. The following bending magnet transported pions to the superconducting solenoid magnet. Decay muons (negative and positive muons, 5-120 MeV/c) were obtained through the in-flight decay of the negative/positive pions confined by a strong longitudinal magnetic field of several tesla from a superconducting solenoid magnet following Eqs. 1.1 and 1.2. Three quadrupole triplets and two bending magnets were used to select the muons momenta and transport them to the experimental area. The obtained muon beam at the D2 experimental area was used for our irradiation experiment. Table 2.1 shows the properties of the decay muon beam at the D2 experimental area. The momentum distribution of the muon beam can be approximated as a normal distribution with 5% standard deviation (Figure. 2.3). The temporal width of the pulsed muon beam was 100 to 130 ns. In the experiment, the 3 GeV proton synchrotron was operated in a single bunch mode with a repetition rate of 25 Hz and an average power of 150 kW. Intense and high-quality negative and positive muon beams are available over a wide range of energy. Thus, the experimental data with high statics can be taken in the facility during short irradiation time.

Table 2.1: Decay muon beams available at D-line. The data are taken from [30]

	Decay muon ($\mu^{\pm}$)
Beam Energy Range	2∼54 MeV
Energy Width (1σ)	5%
Pulse Width	100∼130 ns
Pulse Interval	40 ms
Beam Size	70 mm × 70 mm
Beam Intensity	$10^6 \sim 10^7$

2.2.2 Device Under Test

The SRAM device used in the experiment is described herein. Silicon on thin buried oxide (SOTB) SRAM chips was used in the experiment. SOTB is an ultra-thin body and thin buried oxide silicon-on-insulator (UTBB-SOI) device. The

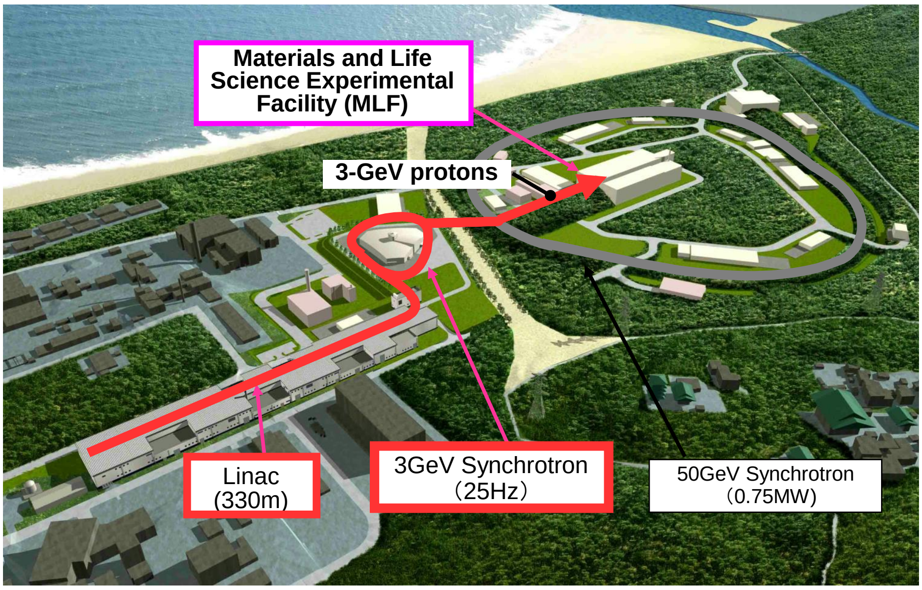

Figure 2.1: Bird's-eye view of the Japan Proton Accelerator Research Complex (J-PARC).

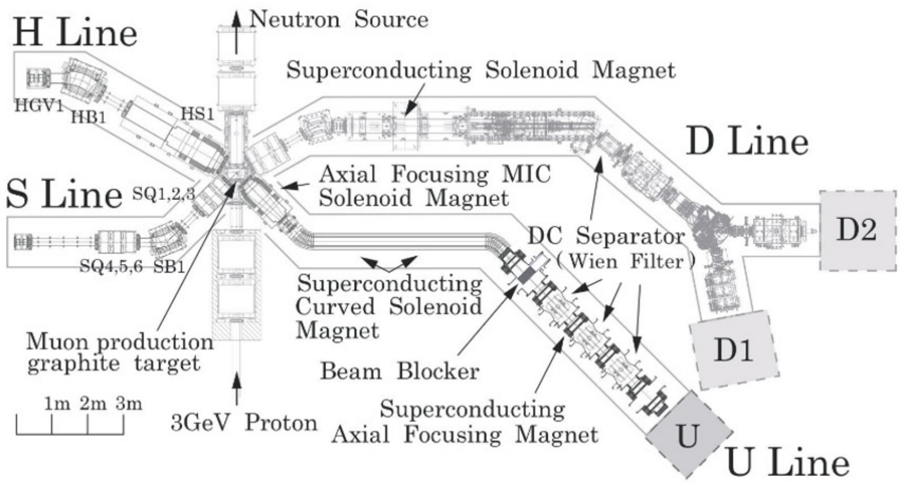

Figure 2.2: Layout of the D-Line, U-Line, H-Line, and S-Line in the MUSE [31].

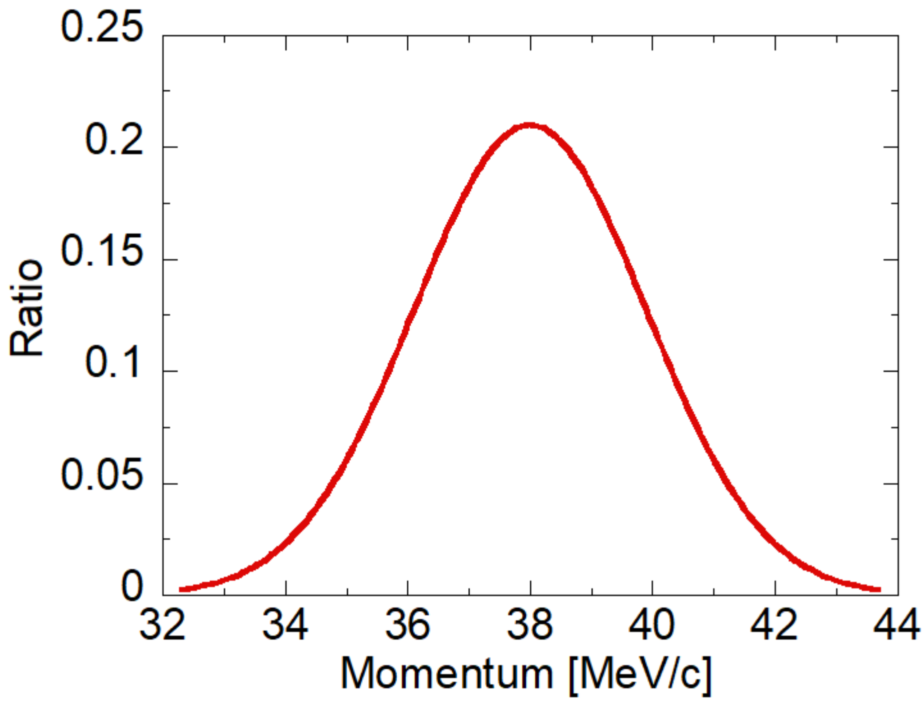

Figure 2.3: Estimated momentum distribution of a muon beam in the case of 38 MeV/c irradiation (6.6 MeV in kinetic energy) at the D2 experimental area of MUSE.

SOTB device structure was compared with that of a conventional bulk device in Figure 2.4. The SOTB device has a thick insulation layer, called BOX layer under the gate. The experimental investigation [34, 35] demonstrated that SOTB devices are more robust than the conventional bulk devices under neutrons and α-ray irradiation. The SOTB device has a higher tolerance on soft errors than the bulk because only the deposited charge in the thin SOI layer affects the SEU occurrence. In the case of the bulk devices, the deposited charges in a larger area compared to the SOI layer are collected to the drain region due to the funneling effect [36].

Figure 2.5 shows the device board under test, on which 16 chips of SOTB SRAMs were configured. The chips were bonded on the device board and covered with black resins for protection. The chip measured 5.2 mm × 3.1 mm and had a thickness is 0.3 mm. The test chips were fabricated in 65-nm SOTB CMOS technology. Figure 2.6 depicts the structure of a SRAM chip. Each chip contained 42 SRAM macros comprising one SRAM test element group (TEG). Each SRAM macro consisted of a memory array, including traditional 6T SRAM cells, read/write circuitry, control unit, and data/address shift registers. Each TEG contained 32 kbit. The SRAM cells (bits) in the TEG were arranged in 64BL × 512WL, and the cells in every 2BL × 64WL share the same well tap, where BL and WL stand for bitline and wordline, respectively. Each chip had a total of 12-Mbit memories.

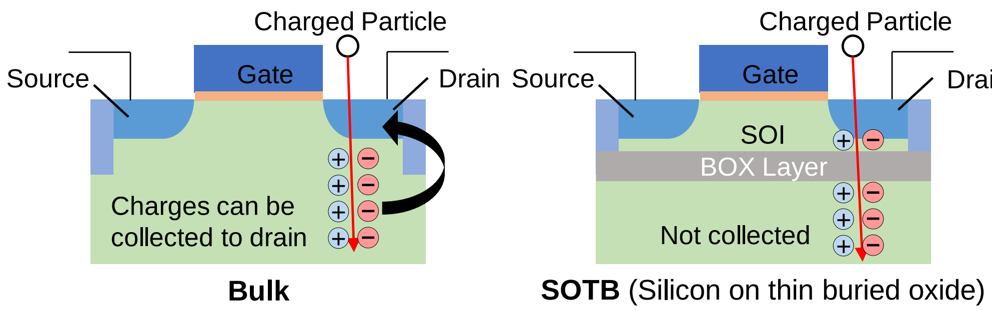

Figure 2.4: Structures of MOSFETs fabricated in bulk and SOTB.

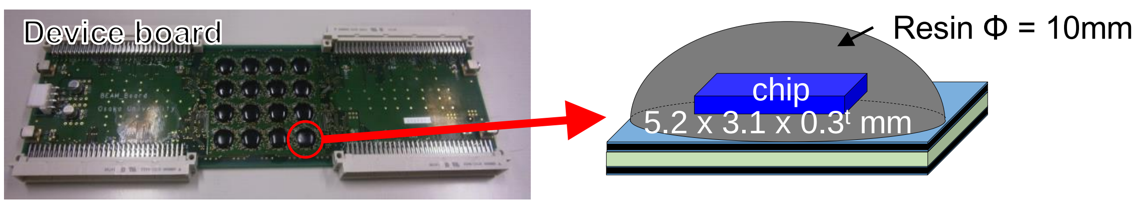

Figure 2.5: Structure of the device board under test. (left) Photograph of the device board. (right) Schematic illustration of a chip in the resin region.

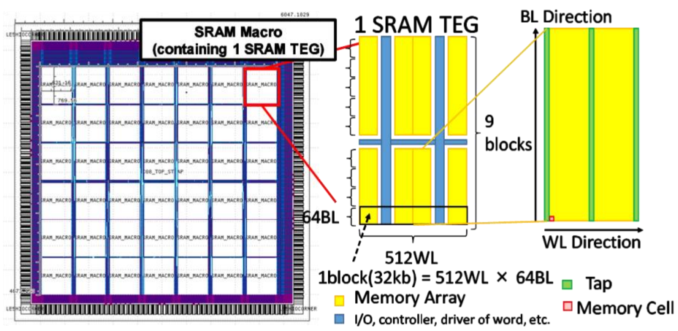

Figure 2.6: Structure of a SRAM chip under test. Each chip consists of 42 SRAM TEGs.

2.2.3 Measurement of SEU Cross Sections

Figure 2.7 illustrates a photograph of our experimental setup at the D2 experimental area. Two kinds of detectors, namely a plastic scintillator and two germanium detectors, were placed downstream of the device board. The details of the detectors will be described in Subsection 2.2.5. The VLSI tester was placed in the experimental area and connected to the device board to read/write the stored data in the chips on the device board.

Figure 2.8 schematically illustrates the muon irradiation configuration. The beam collimator was placed between the beam exit and the device board. The collimator consisted of a 5 mm-thick aluminum front plate and piled up 150 mm-thick lead blocks. The collimator slit was a 50 mm $\times$ 50 mm square-shaped slit. Figure 2.9 shows the beam collimator structure. The front and base plates were made of aluminum. The front plate was fixed vertically on the base plate. The pile-up lead blocks were placed on the base plate. The slit sizes of the lead blocks and the front plate were 60 mm $\times$ 60 mm. All inner surfaces of the lead block slit were covered with the other 5 mm thick-Al plates. Thus, all surfaces, where a muon beam is exposed, were covered with the aluminum plate. The 5 mm-thick Al plates were thick enough to fully stop the muons used in the experiment (i.e., all muons stopped in the aluminum plates). The aluminum plate was chosen such that the emission of the background particles (e.g., neutrons and light ions) from the negative muon capture by nuclei in the plate can be reduced because low-Z materials have a lower capture rate of negative muons. The lead blocks played a role in shielding the decay electrons/positrons from the aluminum plate and background γ-rays. The device board was placed behind the lead block from 35 mm. The device board was fixed vertically to a muon beam with a dedicated fixture (Figure 2.10). Twelve chips in the device were irradiated. The remaining four chips were placed behind the lead blocks to see the influence of the background radiation in the environment. The resin layer was shaped like a hemisphere. The resin thickness varied with the chip position. Hence, the reverse side of the device board was irradiated with the muon beam passing through the collimator (Figure 2.8) to make the muons stop at a similar depth.

Next, the muon irradiation procedure will be described. Prior to the muon irradiation, the error bits (i.e., the SRAM bits which could not properly hold information) of the chips were checked without the muon beam. First, all SRAM bits were initialized by writing data ‘0’. The information in all SRAM bits were read out after a one-second hold operation. A bit with information ‘1’ was then regarded as an error bit. We repeated the checking procedure for ten times. As a result, only an error bit was observed at operating supply voltages from 0.25 to 1.1 V. The error bit was excluded in the following the irradiation and the analysis. Background runs with an aluminum plate placed in the collimator entrance were also conducted under some conditions with different muon kinetic energies and operating voltages. In these cases, the incident muons stopped completely in the aluminum plate, and radiation, other than muons (decay electrons and positrons, neutrons, γ-rays, etc.), bombarded the device board. However, no SEU occurred by these radiations. Moreover, during the muon irradiation on the device board, no SEU was observed in the four chips placed behind the lead blocks (Figure 2.8). Thus, we confirmed that any background noises did not affect the SEU measurement results.

Figure 2.11 illustrates a flow chart of the irradiation tests. In this flow, the supply voltages are first set for the "write" operation. The SRAM memories were initialized by writing a data '0' before each irradiation run for the test through the data/address shift registers. The supply voltage was then changed for the "hold" operation and the SRAM was turned into a "hold" operation. Muon irradiation was performed during this "hold" operation. After which, the voltages were set back for the "read" operation, and the data stored in the SRAM were read through the shift registers. Finally, the number of bit errors was counted.

In the measurement, the kinetic energy of the muon beam was changed from 5.3 to 8.8 MeV (34 to 44 MeV/c in the momenta) at one supply voltage of SRAMs. In two typical momenta, the supply voltage of SRAMs was changed from 0.25 to 1.1 V. Thus, the kinetic energy and the supply voltage dependence of the experimental muon-induced SEU cross-sections were measured. The muon beam in the MUSE had a momentum distribution, which can be 5% standard deviation; thus, the experimental SEU cross-section is defined by the following expression:

$$< \sigma_{\mathrm{SEU}}(E_{\mathrm{mean}}) >= \frac{\int_0^\infty \sigma_{\mathrm{SEU}}(E) \cdot \phi(E, E_{\mathrm{mean}}) dE}{\int_0^\infty \phi(E, E_{\mathrm{mean}}) dE}, \tag{2.1}$$

where $< \sigma_{\mathrm{SEU}}(E_{\mathrm{mean}}) >$ represents the mean SEU cross-section with the muon beam in the MUSE, which has the momentum distribution with the mean kinetic energy E_{mean}, σ_{SEU} is the mono-energetic muon SEU cross-section at the kinetic energy E and $\phi(E, E_{\mathrm{mean}})$ is the fluence of the incident muons with the kinetic energy E in the case of the muon beam irradiation with the mean kinetic energy E_{mean}. The experimental muon-induced SEU cross-sections for the SRAMs were derived by dividing the number of the observed bit errors by the incident muon fluence. The fluence was derived by multiplying the beam flux per proton by the number of triggers from the proton accelerator during the measurement. Subsection 2.2.4 and Section 2.3 will describe the measurement and analysis methods for the beam flux.

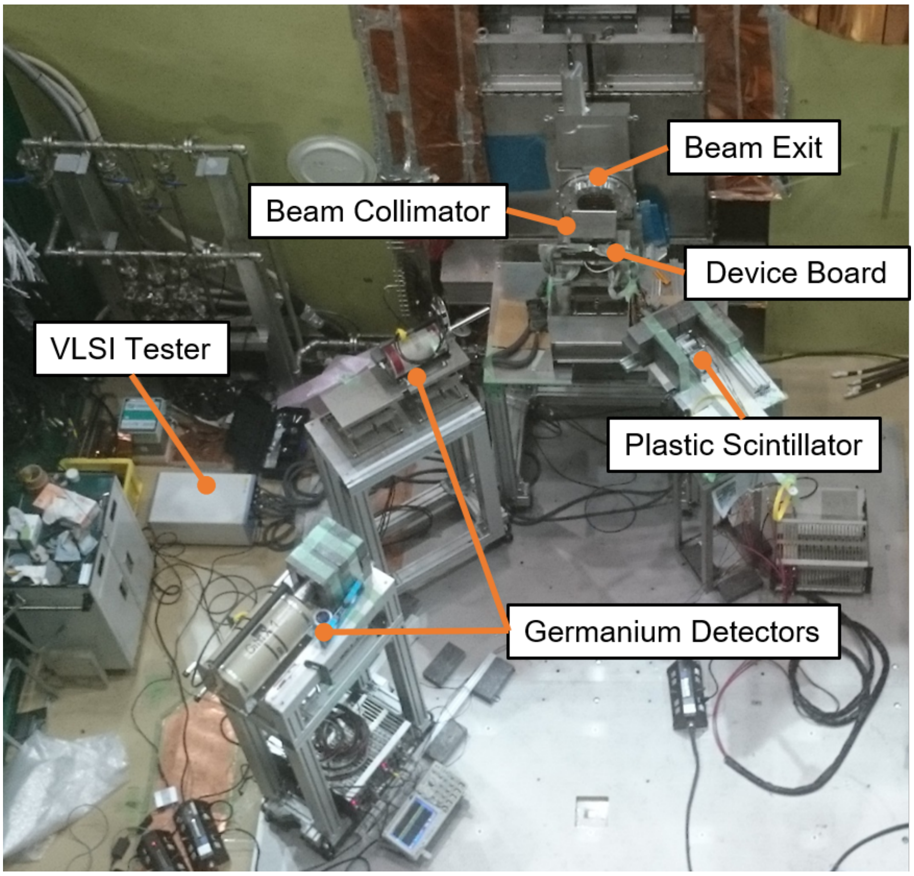

Figure 2.7: Photograph of the experimental setup at the D2 area.

2.2.4 Measurement of Beam Fluxes

The flux per proton beam pulse was determined from the total counts of decay electrons/positrons corrected by the solid angle subtended by the scintillator detector. Some of the stopped negative muons were captured by the nuclei, and the electron was not emitted. The capture rate of negative muons depends on the constituent elements in their stopping position. The device board contains a variety of elements such as silicon, carbon, oxygen, and copper. Therefore, it is difficult to accurately know the capture rate of the negative muons in the stopping position if the detailed information on the structural components are not available. In the present irradiation experiment, we measured the flux of incident negative and positive muons per proton pulse by placing a pure aluminum plate instead of the device board. The pure Al plate measured 100 mm $\times$ 100 mm $\times$ 5 mm^t. We then determined the muon beam flux. The details of the decay electrons/positrons measurement will be described in Subsection 2.2.5.

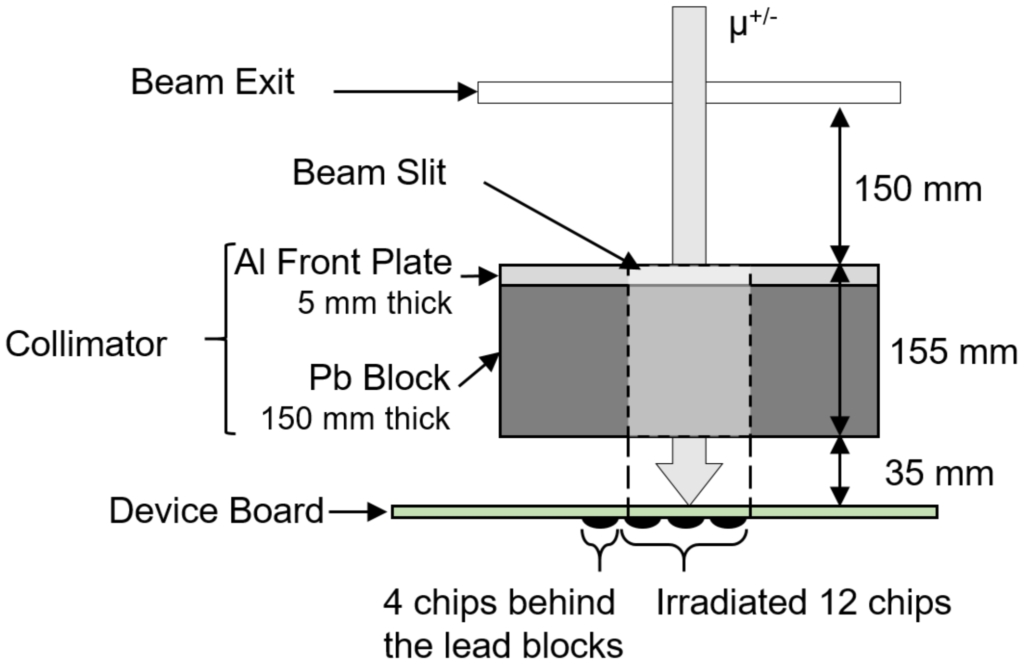

Figure 2.8: Schematic illustration of muon irradiation on the device board.

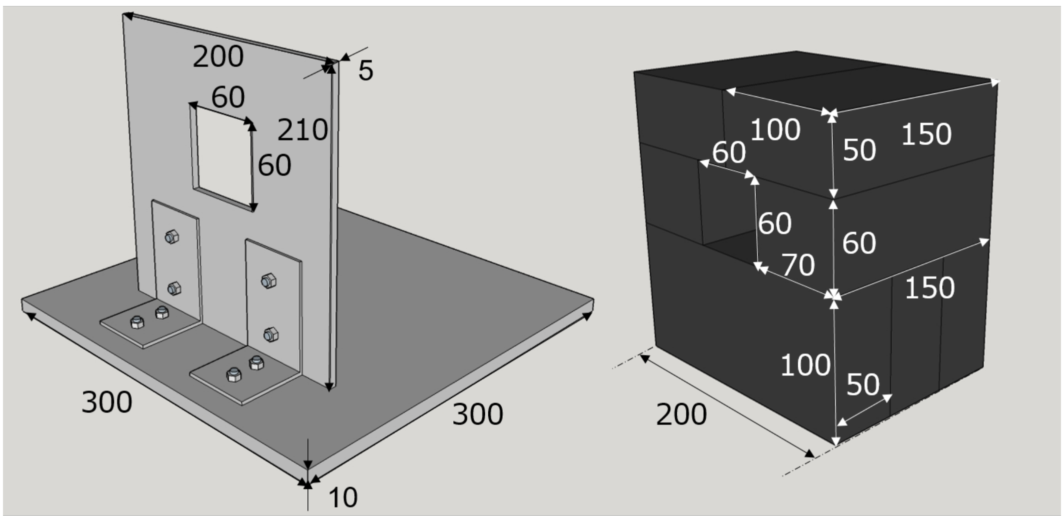

Figure 2.9: Schematic illustration of the beam collimator: (left) Al plate and (right) pile-up lead blocks. The unit of lengths is [mm].

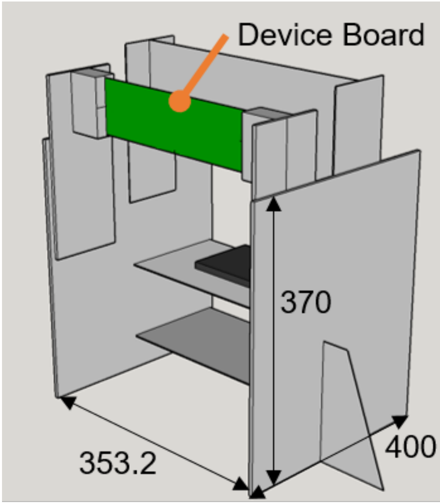

Figure 2.10: Schematic illustration of the fixture of the device board. The unit of lengths is [mm].

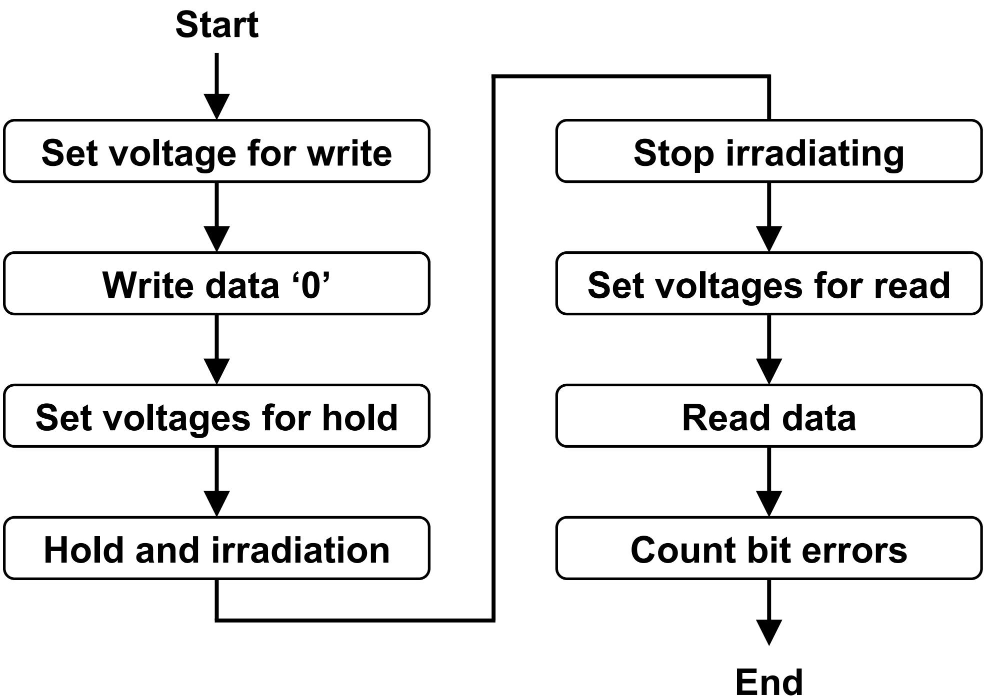

Figure 2.11: Flow chart of the muon irradiation process.

2.2.5 Detectors

Figure 2.12 schematically depicts the detector arrangement. The plastic scintillator was used to derive the muon beam flux by counting the decay electrons/positrons. Two germanium detectors were also used to measure the muonic X-rays emitted from the stopped negative muons.

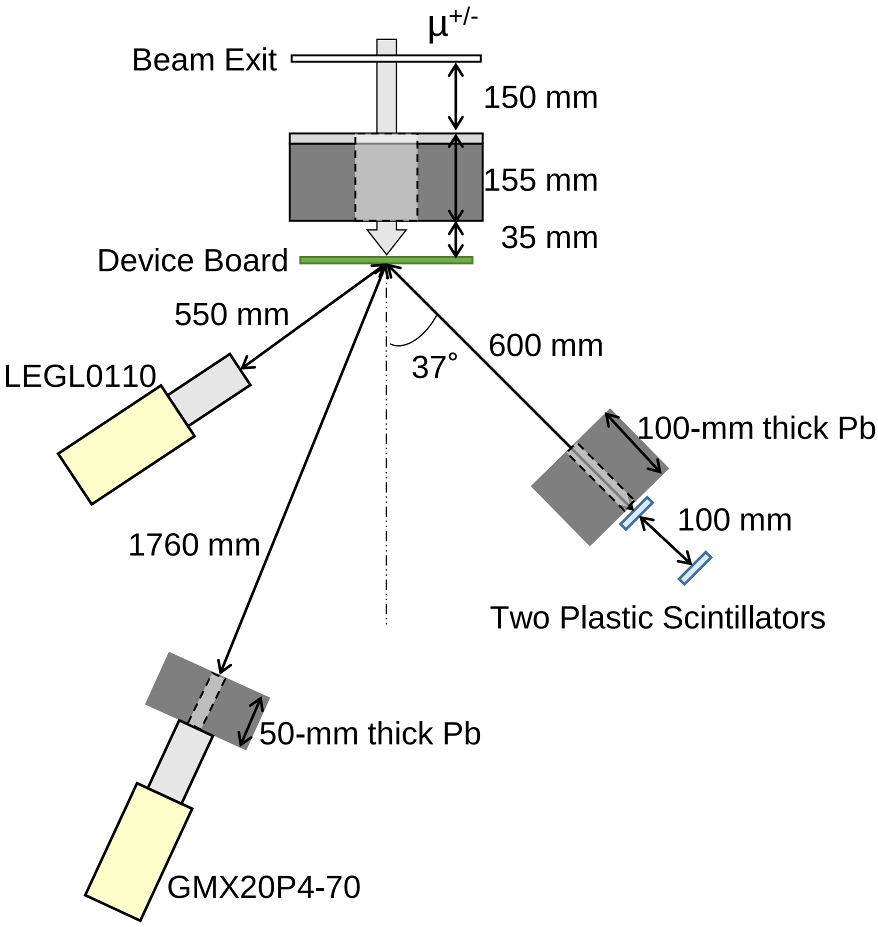

Figure 2.12: Arrangement of the detectors during the experiment.

Plastic Scintillator

Plastic scintillators are the most widely-used organic scintillators. First, a decay electron/positron passed thorough the plastic scintillator and lost their energy. The scintillation light emitted in the plastic scintillator was converted to electrical pulses by photomultiplier tubes (PMTs) connected to one side of the scintillator. In the experiment, the decay electrons/positrons were measured by coincidence counting with two plastic scintillators. They were placed 600 mm from the device board at an angle of approximately 37° (Figure 2.12). The 100 mm-thick piled-up Pb blocks with a 50 mm × 30 mm slit were placed at the front of the scintillators to shield the background radiation (Figure 2.13). The distance between both plastic scintillators was 100 mm The scintillator measured 25 mm × 25 mm (Figure 2.14). The scintillator thickness is 2 mm. Table 2.2 presents general technical data of the scintillator used in the experiment. The BC400 plastic scintillator, which is suitable for electron counting, was used for the experiment. The H3165-10 PMTs manufactured by Hamamatsu Photonics were adopted. The rated voltage of -1000 V was applied between the anode and cathode of the PMTs during the test. A data acquisition system with nuclear instrumentation module (NIM) was adopted to measure the decay electrons/positrons. Figure 2.15 illustrates a schematic block diagram. PMTs 1 and 2 were connected to the forward and backward plastic scintillators, respectively. Electrical pulses from PMTs 1 and 2 were sent to the discriminator (Discri.) 1 and 2, respectively. When the voltages of the electrical pulses from the PMTs exceeded the threshold voltage of the discriminators, the digital signals were sent to the gate generators (G.G). First, a radiation frequency (RF) trigger from the 3 GeV proton synchrotron was sent to the NIM timing-to digital converter (TDC) as a start signal of counting. The trigger indicates the timing when the proton beam is sent to MLF. The trigger was also sent to the G.G 3. Figure 2.16 shows a timing chart of the output signals of three G.Gs. G.Gs 1 and 2 sent the rectangular pulse of width 4.0 μs to the coincidence module when G.Gs received the signals from the discriminators. The width of the pulse from G.G 3 was set to 64 μsec which is enough longer compared to the lifetime of muons to make coincidence count with two signals from two PMTs. When the three signals from the G.Gs were coincidence in time, the signal was sent to the NIM TDC module. Thus, the temporal distribution of decay electrons/positrons was acquired.

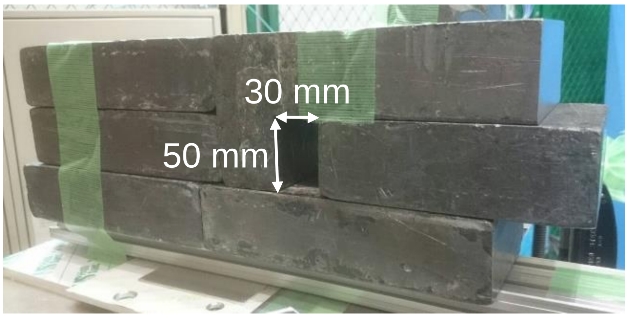

Figure 2.13: The pile-up Pb blocks as the collimator of the plastic scintillators.

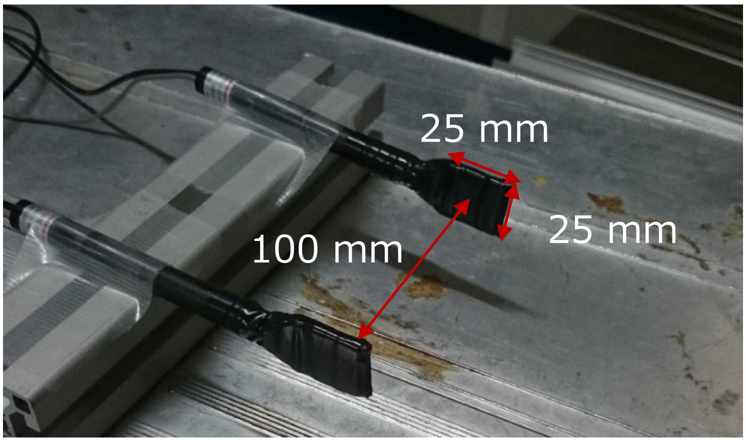

Figure 2.14: Photograph of the two plastic scintillators used in the experiment.

Table 2.2: General technical data of the plastic scintillator used in the experiment.

Model number	BC400
Base	Polyvinyltoluene
Composition formula	$(CH_2CH(C_6H_4CH_3))_n$
Density[g/cm^3]	1.032
Size	25 mm $\times$ 25 mm $\times$ 2 mm^t

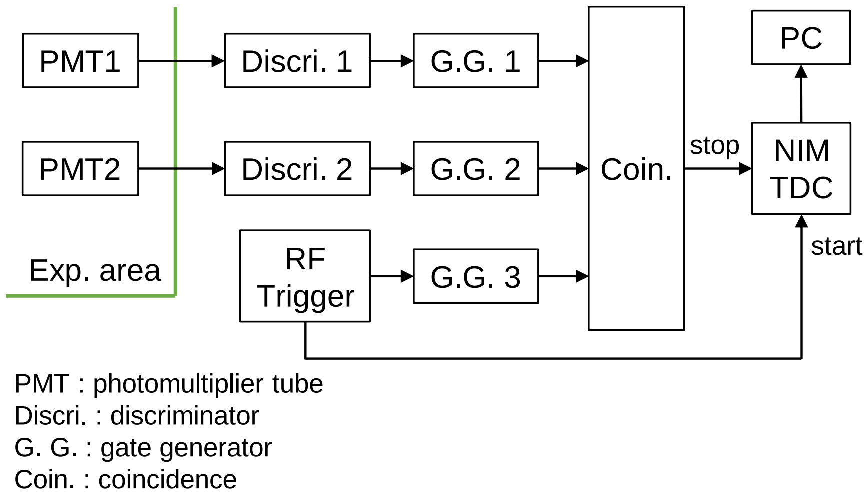

Figure 2.15: Schematic diagram of the data acquisition circuit of the two plastic scintillators.

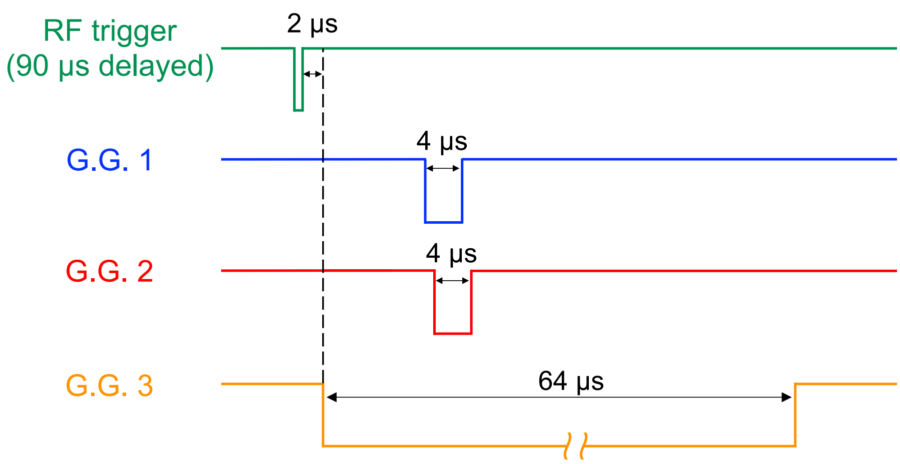

Figure 2.16: Timing chart of the output signals of three gate generator.

Germanium Detector

The muonic characteristic X-rays were measured using the two germanium detectors (i.e., GMX20P4-70 and LEGL0110) with the data acquisition circuit. The energy calibration was performed with a standard radiation source of ^{152}Eu. The two detectors covered different energy ranges. GMX20P4-70 can detect X-rays with an energy under 5000 keV, while LEGL0110 can detect X-rays with an energy under 500 keV, albeit with a higher-energy resolution compared to GMX20P4-70. Figure 2.12 presents the arrangement of the two detectors. LEGL0110 was placed 550 mm from the device board, while GMX20P4-70 was placed 1760 mm from the device board with the 50 mm-thick shielding lead blocks with a 50 mm $\times$ 18 mm square-shaped slit (Figure 2.17). The role of the lead blocks was to reduce the X-ray count rates. The measurement results of the muonic X-ray can provide additional information on the position where the negative muons stopped in the device board. However, the measurement time was not enough to obtain sufficient statistics, and the quantitative analysis of X-rays has not been performed.

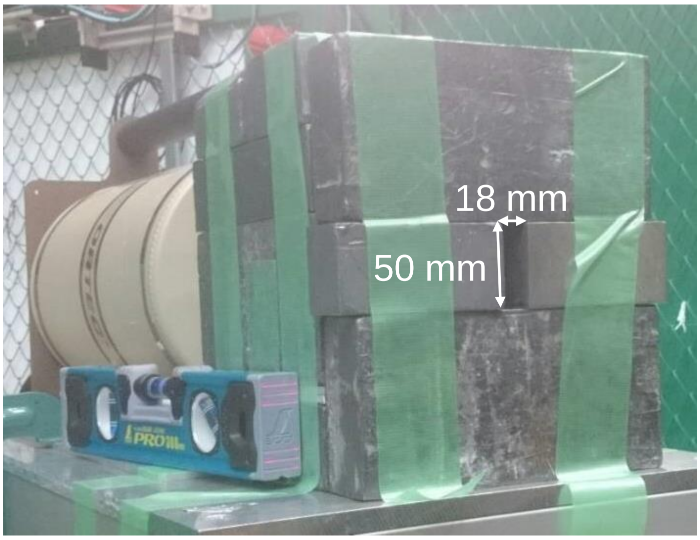

Figure 2.17: 50-mm thick shielding lead blocks with a 50 mm $\times$ 18 mm square-shaped slit.

Beam Profile Monitor

The beam profile monitor [37] developed at J-PARC MUSE was adopted to obtain a two-dimensional (2D) beam profile of incident muons. Figures 2.18 and 2.19 show a photograph and a schematic drawing of the beam profile monitor, respectively. A scintillation screen and UVT acrylic blocks were contained in a light-tight polyvinyl chloride (PVC) tube for light-shielding. The upstream side of the scintillation screen was covered with a 0.16 mm-thick black-colored PVC sheet to shield light from the outside. The black PVC sheet was also used for the light-tight connection between the PVC tube and a large aperture lens. A round-shaped scintillation screen (Φ130 mm and t2 mm) was made of an EJ-212 plastic scintillator. When the muons interact with the scintillation screen, the scintillation light is produced from the deposited energy. The scintillation light emitted downstream passed through the UVT acrylic blocks and focused on a photocathode of a gated II via the large aperture lens with a 2 mm macro ring. The intensified light from the output window of the gated II was directed to a cooled CCD unit via a relay lens and finally captured by a 1/2 in. CCD image sensor. Thus, the 2D muon beam distribution can be measured as a CCD camera image.

Figure 2.20 shows a photograph of the profile monitor arrangement in the measurement. During the beam profile measurement, the device board was removed, and the profile monitor was placed behind the beam collimator. The beam profiles were obtained with negative and positive muon beams having several incident kinetic energies. The CCD camera shutter was opened for 30 s in each beam condition, and the beam profile was obtained.

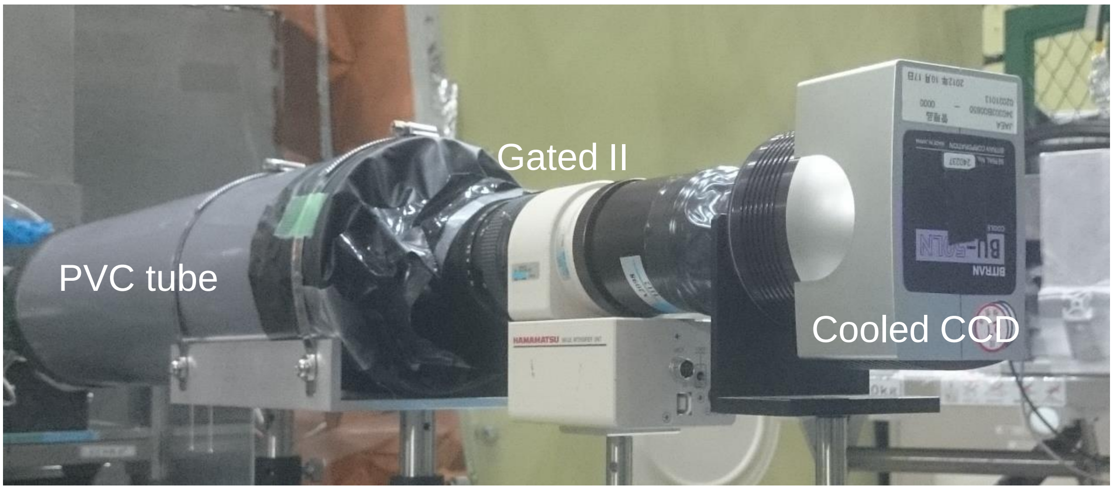

Figure 2.18: Photograph of the beam profile monitor.

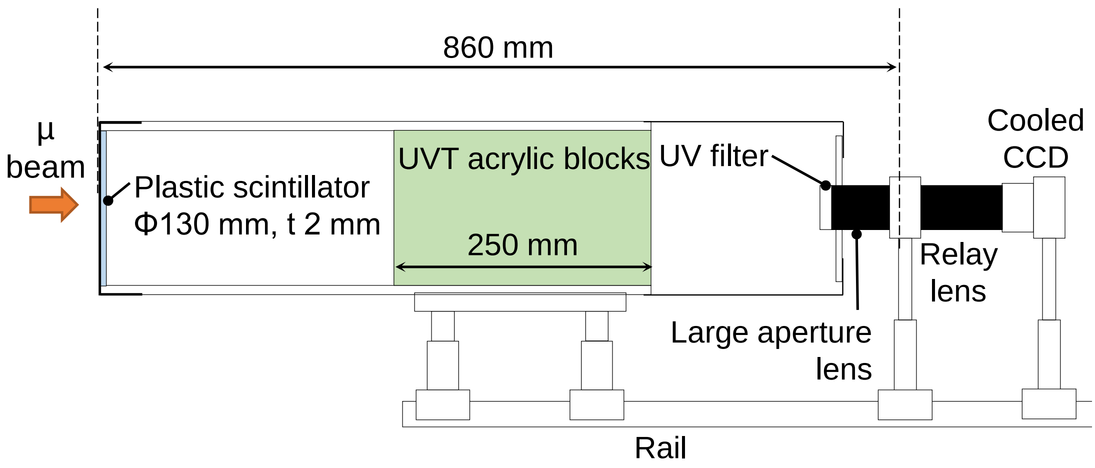

Figure 2.19: Schematic drawing of the beam profile monitor.

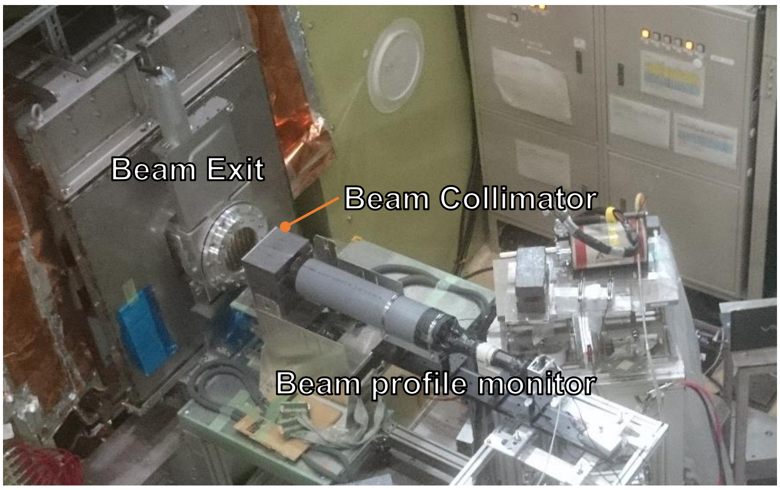

Figure 2.20: Arrangement of the beam profile monitor during the measurement of beam profiles.

2.3 Data Analysis

This section describes the data analysis method of the present experiment. The measured data of the plastic scintillators are analyzed to obtain the muon beam flux. Moreover, the data from the beam profile monitor is analyzed to validate the derived beam flux.

2.3.1 Beam Flux

The fluxes were measured as a function of the incident kinetic energy by placing a pure aluminum plate as the target. The muon beam flux per proton beam pulse F is given by

$$F = \frac{C_e}{f_{\mathrm{co}} \cdot R_{\mathrm{det}} \cdot f_{\mathrm{conv}}} \quad \text{[muon/pulse]}, \tag{2.2}$$

where, C_e represents the number of detected decay electron/positron per proton beam pulse, f_{co} and R_{det} are the correction coefficient and the detection efficiency for the decay electrons/positrons as derived later in this subsection, respectively. f_{conv} is decay rate of muons. Under positive muon irradiation, f_{conv} is equal to unity because all positive muons decay into positrons. However, under negative muon irradiation, f_{conv} is not equal to unity because some of negative muons do not decay due to the nuclear negative muon capture reaction by nuclei. The decay rate of negative muons in aluminum was assumed to be 41 % based on the experimental values [8]. C_e was measured for all kinetic energy used in the experiment as shown in Fig. 2.21. In each measurement, the count of decay electrons/positron was over thousand. Hence, the statistical errors of the measurements are under 3 %. First, the temporal distribution of the events detected by the plastic scintillator will be discussed to check that the events were caused by the incident muons. Next, the derivations of f_{co} and R_{det} will be described.

Temporal Distribution of Coincident Events

Figure 2.22 shows the temporal distribution of the coincident events measured by the two plastic scintillators in the case of irradiation of 6.6 MeV negative and positive muons on the device board. Both the counts decrease exponentially with time. The mean lifetime of positive muons is 2.2 μsec, while that of negative muons is 1.7 μsec and smaller than that of positive muons because a certain fraction of negative muons is captured by nuclei. Here, the mean lifetime is defined by the time for the number of muons to reduce to 1/e of the initial number. To determine the mean lifetime by curve fitting of the measured temporal distribution, the coincident events were counted over enough longer time compared to the mean

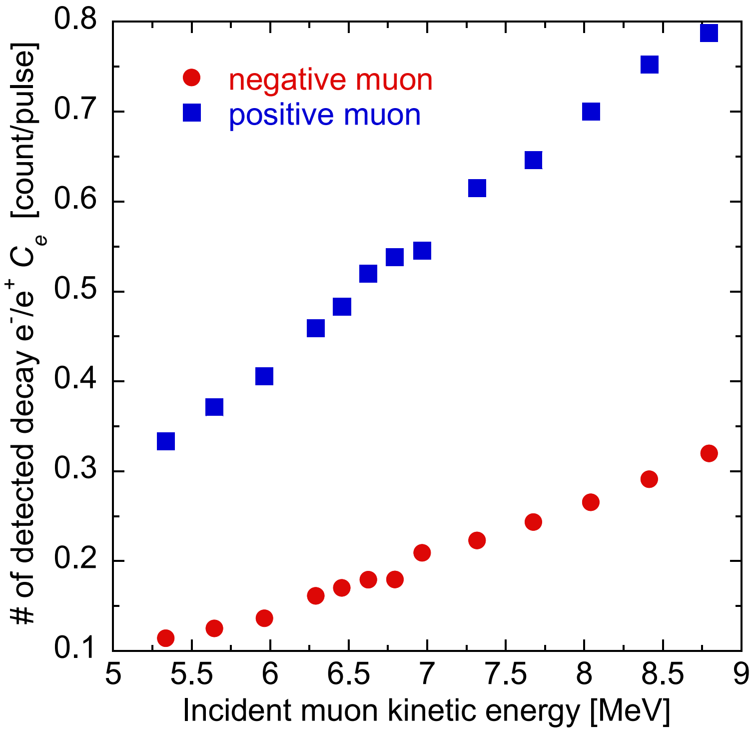

Figure 2.21: Number of decay electron/positron detected by the plastic scintillators per proton beam pulse. The statistical error for each measurement is below 3%.

lifetime of muon. Thus, we concluded that the measured electrons/positrons came from decays of muons.

Correction for the Angular Distribution of Decay Positrons/Electrons

The decay electrons/positrons are distributed asymmetrically with respect to the muon polarization as a result of parity violation [38]. The positron and the electron have tendency to be emitted to the similar and reverse directions of the muon spin, respectively. Figure 2.23 illustrates the angular distribution of the emitted decay electrons/positrons in our experiment setup. Both electrons and positrons tended to be emitted to the plastic scintillators placed downstream. However, the polarization ratios were different between the negative and positive muons. Approximately 80% of the positive muons was polarized during the experiment. In contrast, approximately only 15% of the negative muons was polarized because the negative muons interacted with the nuclei. Hence, the incident amounts of the emitted electrons/positrons bombarded on the plastic scintillators were different between negative and positive muon irradiation.

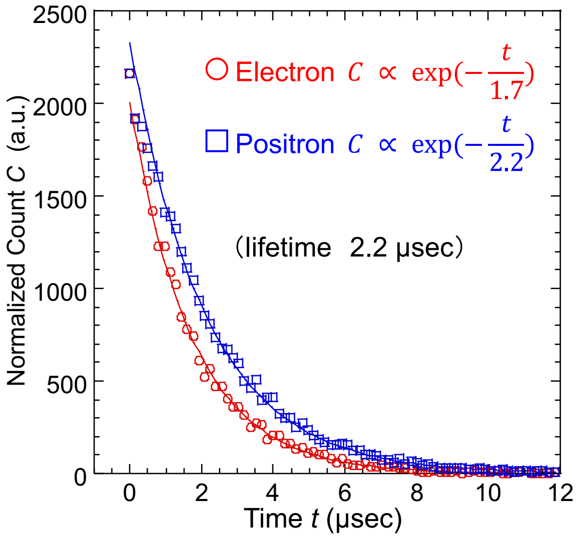

Figure 2.22: Normalized number of coincident events of the two plastic scintillators as a function of time.

The correction coefficient $f_{\rm co}$ for the difference is derived. The coefficient is defined as the ratio of the incident rates of the emitted electrons/positrons on the plastic scintillators with the angular distribution R and the one with an isotropic distribution $R_{\rm iso}$ given by the following equation:

$$f_{\rm co} = \frac{R}{R_{\rm iso}}, \tag{2.3}$$

R is calculated with the angular distribution $W(\theta, \varepsilon)$,which was derived in [39], given as follows:

$$W(\theta,\varepsilon)d(cos\theta)d\varepsilon = \varepsilon^2(3-2\varepsilon)(1+p\frac{2\varepsilon-1}{3-2\varepsilon}cos\theta)d(cos\theta)d\varepsilon, \tag{2.4}$$

$$\varepsilon = \frac{E}{E_{\rm max}}, \tag{2.5}$$

where θ is an angle between the muon spin and the emission angle of a decay electron/positron, and ε represents the ratio of the maximum energy $E_{\rm max}$ of decay electron/positron (52.32 MeV) to an energy E of an emitted electron/positron. The quantity of p is the polarization rate. The incident rate R was calculated by integrating $W(\theta, \varepsilon)$ from $\theta = 0.646$ rad to $\theta = 0.682$ rad and from $\varepsilon = 0$ to

$\varepsilon = 1$. Thus, we obtained $R = 0.0110 + p \cdot 2.89 \times 10^{-3}$. The isotropic angular distribution W_{iso} is given by the following equation:

$$W_{iso}(\theta, \varepsilon)d(cos\theta)d\varepsilon \quad = \quad \varepsilon^2(3 - 2\varepsilon)d(cos\theta)d\varepsilon. \tag{2.6}$$

R_{iso} is derived by integrating W_{iso} over the same range as R. We obtained R_{iso} = 0.0110. The correlation coefficient f_{co} is derived from the Eq. (2.3). f_{co} was $1 + p \cdot 0.263$. In this analysis, p_{μ^+} (polarization rate for positive muon) is assumed as 0.8 and p_{μ^-} (polarization rate for negative muon) is assumed as 0.15. Hence, we obtained the correction coefficient for positive muon $f_{\text{co\_}\mu^+} = 1.21 \pm 0.053$ and that for the negative muon $f_{\text{co\_}\mu^-} = 1.04 \pm 0.014$. The uncertainty is caused by the uncertainty of the muon beam polarity. The result indicates that the count rates on the plastic scintillator increases by 21% and 4% compared to that with an isotropic distribution under positive and negative muon irradiation, respectively.

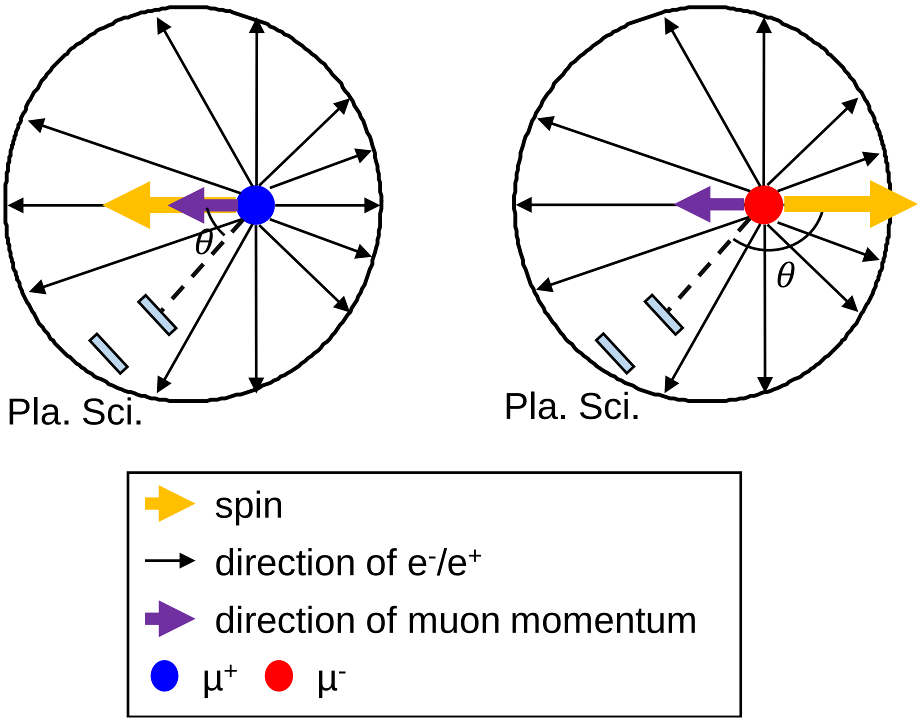

Figure 2.23: Angular distribution of decay positron/electron from decay of muons.

Detection Efficiency of the Plastic Scintillators

The energy threshold for the two plastic scintillators must be considered to derive the detection efficiency in addition to the geometrical efficiency. Hence, the transport and energy deposition simulation of the decay electrons/positrons was performed with PHITS [9] to calculate the detection efficiency of the scintillators. First, the counting ratio of the backward plastic scintillator to the forward scintillator was found to be 1.95 ± 0.2 from the experimental result. Next, the experimental setup shown in Figure 2.12 was reproduced in the PHITS simulation. The transport simulation of the decay electrons/positrons and the energy depositions in the two scintillators were then calculated. The energy thresholds for the scintillators were chosen to reproduce the counting ratio based on the voltage thresholds (129 and 37 mV for the forward and backward scintillators, respectively). The energy thresholds for the forward and backward scintillators were selected as 0.35 and 0.11 MeV, respectively. Finally, R_{det} was found to be $(4.19 \pm 1.30) \times 10^{-5}$ by calculating the coincidence probability of the energy deposition over the thresholds in the two scintillators.

Derived Muon Beam Flux

Figure 2.24 presents the fluxes of the negative and positive muon beams. The positive and negative muon fluxes were almost the same in magnitude and monotonically increase with the kinetic energy. The systematic uncertainty of the derived flux was assumed to be 30%. The uncertainty mainly arose from the R_{det} derivation as discussed above. The systematic uncertainty of the experimental SEU cross-section derived in Section 2.4 thus is estimated to be 30%.

2.3.2 Validation of the Derived Muon Beam Flux

We performed the measurement of the beam profile in addition to the measurement with plastic scintillators to validate the derived beam flux. The ratio of the negative and positive muon beam fluxes was validated by the beam profiles. Moreover, an additional measurement [40] of the SEU cross-sections was performed at MuSIC [32] to validate the absolute flux values.

Beam Profile Monitor

The beam profile monitor can obtain a 2D distribution of the muon beam intensity, as shown in Figure 2.25. The beam intensity tended to increase toward the center. The beam was shaped like a square because of the beam collimator slit. We confirmed the ratio of the negative and positive muon fluxes of the same kinetic energy by analyzing the obtained images. First, the brightness values in the integration area were integrated by

$$B_{\mathrm{SUM}} = \sum_{x}\sum_{y} B_{x,y}, \tag{2.7}$$

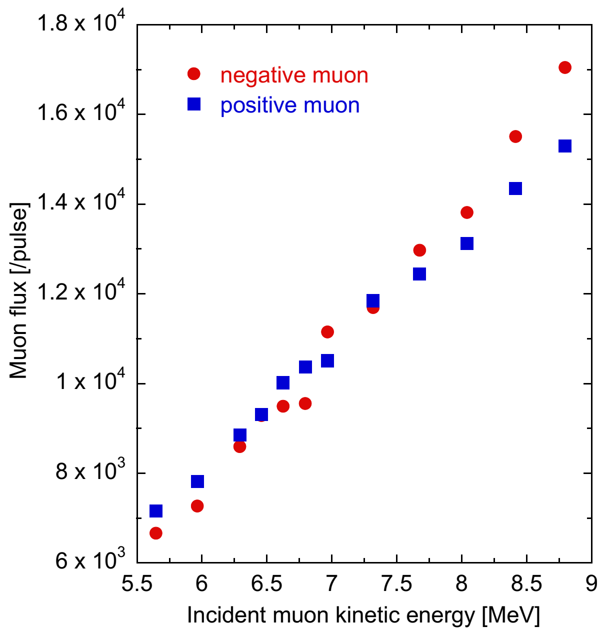

Figure 2.24: Flux of positive and negative muon beam as a function of the incident muon kinetic energy. The statistical error for each measurement is below 3%.

where B_{SUM} is the sum of the brightness values in the area, and $B_{x,y}$ is the brightness value in the position (x, y). The sum of the brightness values is then compared to that obtained from the muon beam image with another polarity given as

$$P = \frac{B_{\mathrm{SUM\_positive}}}{B_{\mathrm{SUM\_negative}}}, \tag{2.8}$$

where, $B_{\mathrm{SUM\_positive}}$ and $B_{\mathrm{SUM\_negative}}$ are the sum of the brightness values for the positive and negative beam with the same kinetic energy, respectively. Beam fluxes with different kinetic energies cannot be compared because the timing of opening shutters was different. The ratios of the negative and positive muons obtained from the beam profile image were compared to those obtained from the measurement of the decay electrons/positrons in Figure 2.26. The positive muon beam flux was approximately only 5% larger than the negative one. Both fluxes are almost the same. The ratios of the negative and positive muons obtained from the plastic scintillators were consistent with those from the beam profile monitor.

Assessment of Absolute Value of Flux

An additional experiment [40] was performed at MuSIC to validate the beam flux derived in the present study. As mentioned in Section 1.6, a DC muon beam

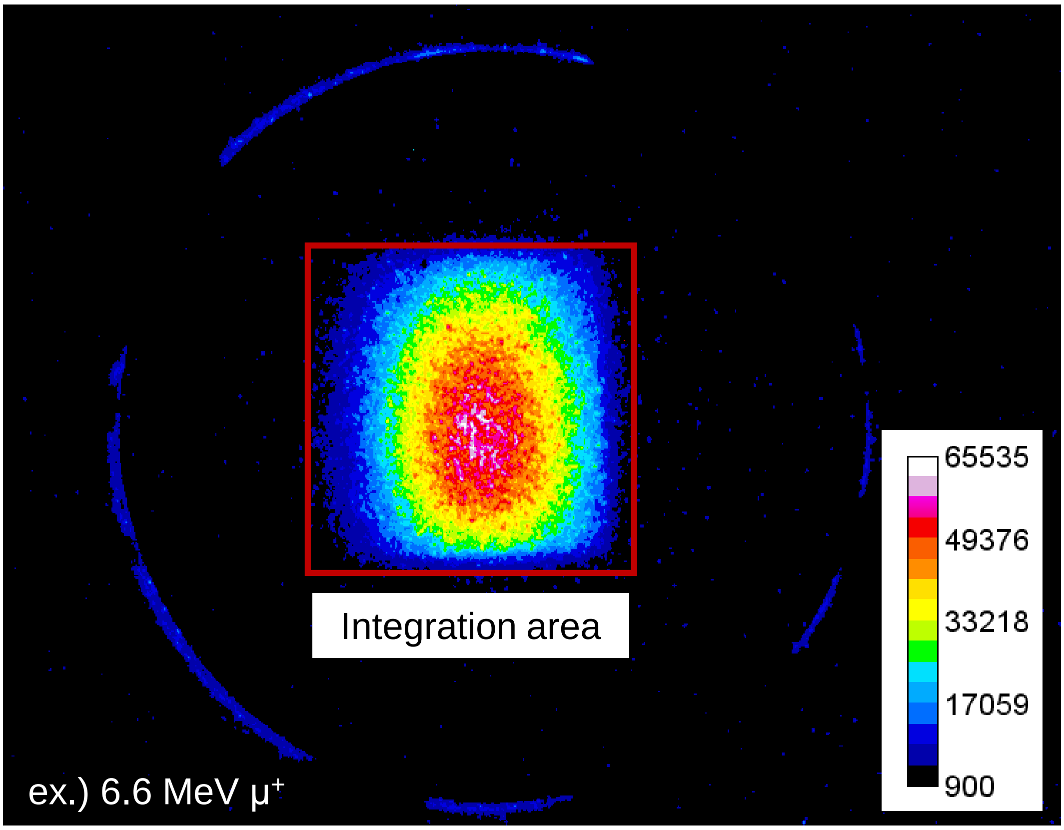

Figure 2.25: 2D distribution of the muon beam observed by the beam profile monitor. The image with the positive muon beam with 6.6 MeV kinetic energy (38 MeV/c in momentum) is shown here as an example. The profile shape represented the slit of the beam collimator.

is available at MuSIC. Reliable muon fluxes can be obtained at MuSIC because a single muon can be detected individually. The systematic uncertainty of the derived beam flux was assumed to be 2% [40]. The experimental SEU cross-sections for the bulk SRAM measured at the MUSE were compared to those at MuSIC. The measurement of the cross-sections at MUSE was performed with the same setup for the SOTB SRAM, as described in this section. The comparison showed that the cross-sections measured at MUSE were in a good agreement with those at MuSIC, indicating that the fluxes used to derive the experimental SEU cross-sections herein were properly determined.

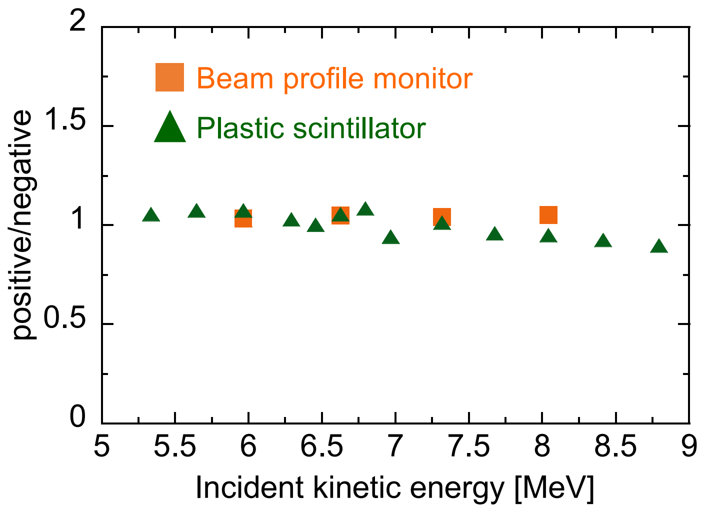

Figure 2.26: Ratio of negative and positive muon beams obtained by two measurement method: beam profile monitor and plastic scintillator. The tendency of the plastic scintillator corresponds to the ratio of negative and positive muon flux in Figure 2.24.

2.4 Experimental Results and Discussion

The incident kinetic energy dependence and the supply voltage dependence of the experimental negative and positive muon-induced SEU cross-sections were measured in the experiment. Here, the experimental results are discussed and compared to those of the previous works.

2.4.1 Kinetic Energy Dependence

Irradiation tests with negative and positive muons were performed in the kinetic energy range from 5.3 to 8.8 MeV. All SRAMs were operated at a supply voltage of 0.5 V during the tests. The measured SEU cross-sections were plotted Figure 2.27 as a function of the kinetic energy. The error bars show the statistical uncertainties.

Both the negative and positive muon SEU cross-sections had peaks around 6.6 MeV (Figure 2.27). Our simulation with PHITS [9] showed that the 6.6-MeV muon can stop in the vicinity of the sensitive volume as described later in Chapter 3. In other words, the muon deposits the maximum charge in the region localized at the end of its path, and the deposited charge leads to a high probability of SEU occurrence. The peak energy of 6.6 MeV depends on the experimental condition that determines the range of incident muons in the SRAM chip (i.e., geometry and composition of the chip and the device board).

Next, the experimental negative muon SEU cross-sections found to be approximately two to four times larger than the positive muon SEU ones in the kinetic energy range from 5.6 to 7.0 MeV. From this result, the secondary ions generated during the negative muon capture process are expected to dominate the SEU rates compared to the SEU induced by direct ionization. The incident muon energy was higher; thus, the difference between both muons in the SEU cross-section was smaller, and both were almost the same over 7.3 MeV. Most muons with an energy over 8.0 MeV passed through the device board, and the negative muon capture reaction seldom happened near the sensitive volume. The direct ionization mainly contributed to the SEU occurrence. Therefore, the difference between the positive and negative muon SEU cross-sections was approximately equivalent to the contribution from the secondary heavy and light ions generated by the negative muon capture reactions in the device.

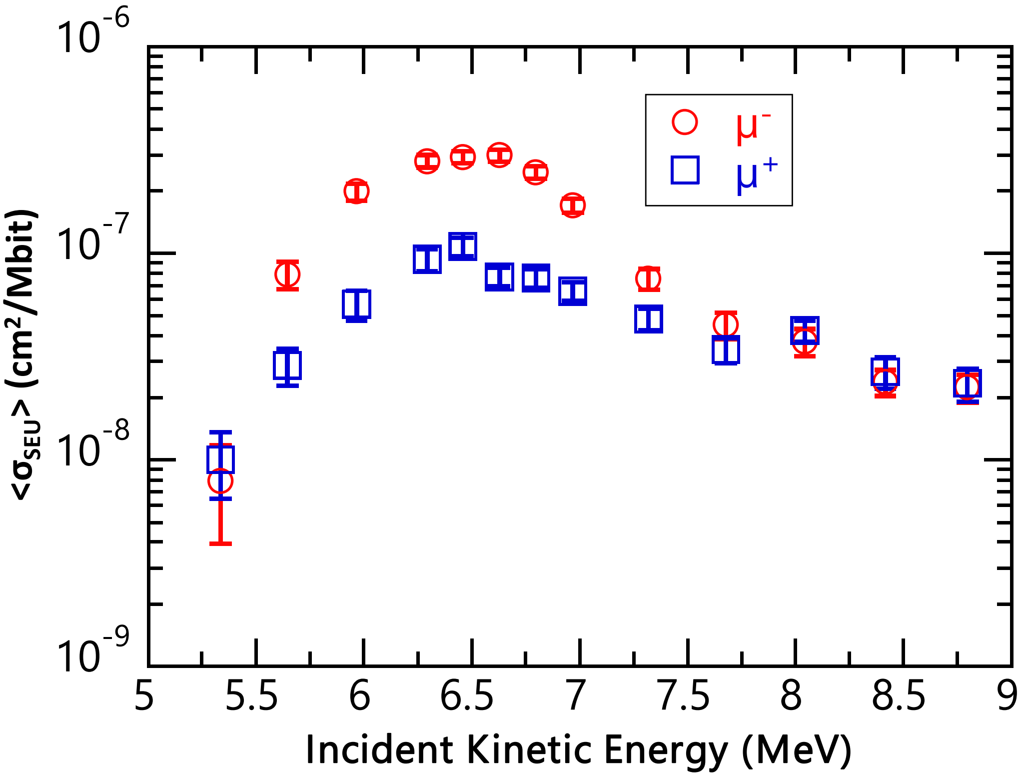

Figure 2.27: Measured cross sections of SEUs induced by negative and positive muons as a function of the kinetic energy. All SRAMs were operated with a supply voltage of 0.5 V.

2.4.2 Supply Voltage Dependence

Figure 2.28 shows a comparison of the SEU cross-sections between negative and positive 6.6 MeV muons as a function of the operating supply voltage. Both the mean SEU cross-sections decreased with the increasing supply voltage. However, the negative muon mean SEU cross-section was significantly larger than the positive muon SEU at a higher supply voltage above 0.4 V. Therefore, at a higher supply voltage (i.e., at a larger critical charge Q_c), the negative muon SEU is expected to occur more frequently than the positive muon SEU due to the larger amount of charge deposited by the negative muons. It can be understood from consideration that the charge deposited by the secondary ions generated from the negative muon capture is much larger than that deposited by the muon direct ionization.

A similar comparison is presented in Figure 2.29 for muons with a higher energy of 8.4 MeV, which can pass through the device board. As mentioned in Subsection 2.4.1, the direct ionization is expected to provide a predominant influence on the SEU occurrence mainly at 8.4 MeV. Therefore, it is reasonable that the negative and positive muon SEU cross-sections are almost the same over a wide range of supply voltage in this case.

2.4.3 Comparison with Previous Works

Section 1.5 provides some experimental results of positive muon SEU cross-sections [24–28]. The present result of the kinetic energy dependence of the SEU cross-sections was qualitatively similar to the previous results (e.g., Figure 1.9a). The mean SEU cross-sections showed a maximum value at a certain incident momentum (energy), although the momentum (energy) depended on the experimental conditions (the structure of devices under test, with/without package, and so on). Moreover, the strong supply voltage dependence shown in Figures. 2.28 and 2.29 was similar to the results in [24, 26] (e.g., Figure 1.9b).

With respect to the negative muon SEUs, only the numerical simulation result of Serre et al. [29] is available for the 65 nm bulk SRAMs. Figure 5 in [29] (Figure 1.10 in this thesis) can be compared with Figure 2.27 in the present result. The former provides the SEU cross sections in the kinetic energy range from 0.1 to 0.9 MeV. The difference of the kinetic energy range is caused by the SRAM structure that determines the relation of the muon kinetic energy and range in the chip. Both results had peaks near the kinetic energy, where the muons stop in the vicinity of the sensitive volume. However, the experimental peak was much broader than that of the simulation, because mono-energetic muons were assumed in the simulation and the muon beam having a normal momentum distribution were used in the experiment. The simulation also showed the relative fraction of

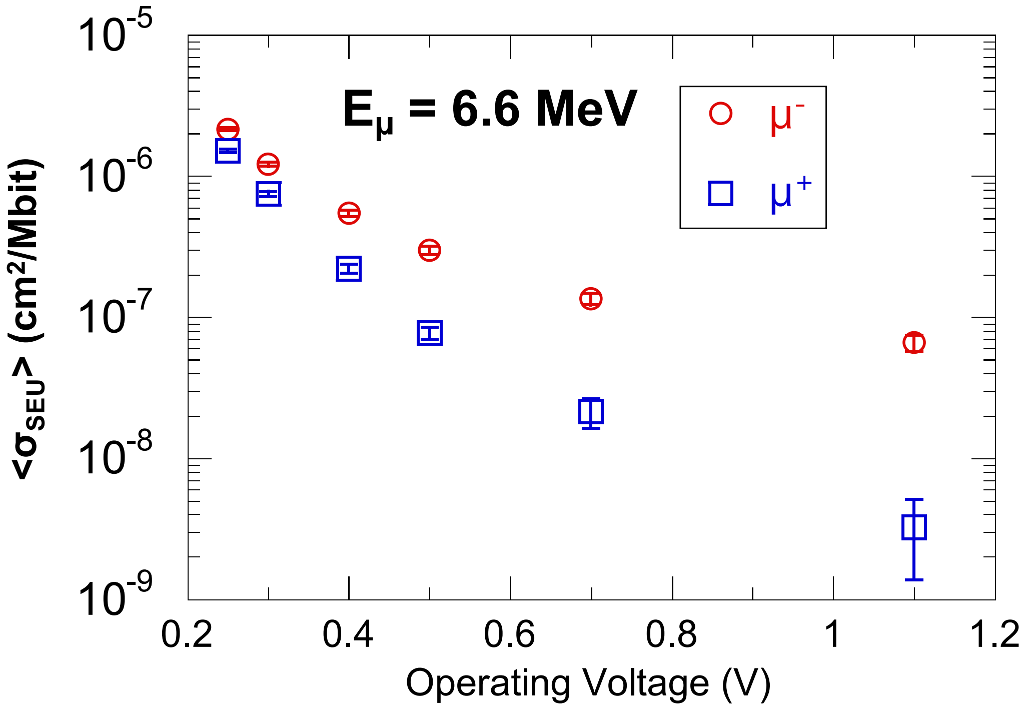

Figure 2.28: Supply voltage dependence of measured SEU cross sections at the incident muon energy of 6.6 MeV (38 MeV/c in momentum).

the muon capture and direct ionization in the SEUs separately. In the low kinetic energy range, including the maximum peak, the muon capture was a dominant process causing the SEUs. The direct ionization process becomes more dominant in SEU than the capture process as the kinetic energy increased. Our observation of the negative muon SEUs qualitatively supports the simulation result of Serre et al.

2.4.4 Comparison with the Measured SEU Cross Sections for Bulk SRAM

A comparison of the experimental SEU cross-sections for the SOTB and bulk SRAM is made to investigate the difference of the SEU occurrence depending on the SRAM structure. Irradiation tests with the bulk SRAM were also performed with the same procedure described above. The structure of the tested device board, SOTB, and bulk, was the same, except for the transistor volume. Hence, the ranges of the incident muons in the transistor in two types of chip were the

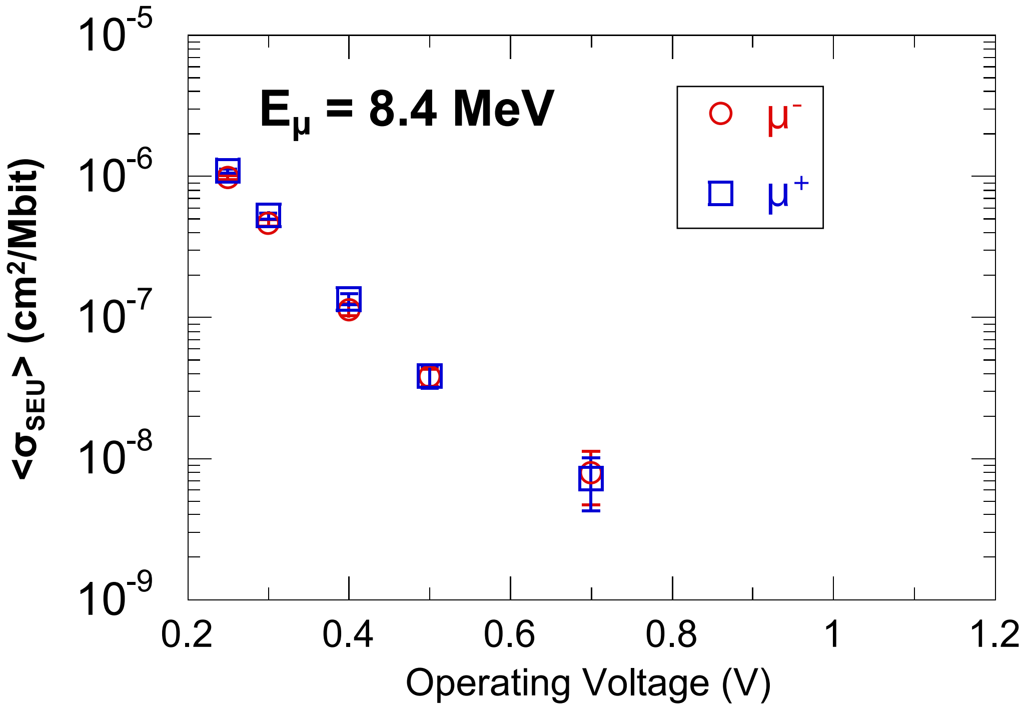

Figure 2.29: Supply voltage dependence of measured SEU cross sections at the incident muon energy of 8.4 MeV (43 MeV/c in momentum).

same. The results of the test with bulk were discussed in [41]. The incident kinetic energy and operating supply voltage dependence of the cross-sections was also investigated for the bulk SRAM.

Figure 2.30 depicts the observed operation voltage dependence for the two SRAMs by 6.6 MeV positive and negative muon irradiation. The positive muon SEU cross-sections for the bulk SRAM were approximately two to four times larger than those for the SOTB SRAM (Figure 2.30a), except at 1.1 V where the statistics is not enough. The positive muon SEU cross-sections for both the bulk and the SOTB SRAMs similarly and monotonically decreased with the increasing supply voltage. In contrast, the negative muon SEU cross-section for the SOTB SRAM more gradually decreased compared to the positive muon SEU with the increasing supply voltage. Moreover, the negative muon SEU cross-section for the bulk SRAM reached the minimum at 0.5 V and increased to a saturated value above 0.5 V because of a significant increase in the multiple cell upset (MCU) cross section caused by the parasitic bipolar action (PBA) effects. The PBA effect on the SEU occurrence was discussed in [41], in which the supply voltage dependence of PBA-induced SEUs was suggested. As shown in Figure 2.31, the PBA contribution to the SEU cross-section increases with the increasing the supply voltage, while the contribution of drift and diffusion charge collection ('critical charge dependence' in Figure 2.31) decreases. The PBA-induced MCU was caused by the large charge deposited to the transistor volume of the bulk SRAM. The simulation in [41] clarified that negative muons can deposit sufficient charge (above 5 fC) to cause PBA due to the secondary ions emitted from the negative muon capture reaction. In addition, the direct ionization of muons cannot cause a PBA because of the lower stopping power compared to that of the secondary ions. The PBA does not occur in the SOTB SRAM. Therefore, under the negative muon irradiation, the SEU cross-section for the bulk SRAM was at least 6.5 times larger than those for the SOTB SRAM shown (Figure 2.30b). Thus, our previous experiment demonstrated that the negative muons have a larger impact on the SEU occurrence compared to positive muons, especially in the bulk SRAM. The negative and positive muon-induced SEU rates under a terrestrial radiation environment are calculated in Chapter 3 to investigate the impact of negative muons on SERs on the ground level.

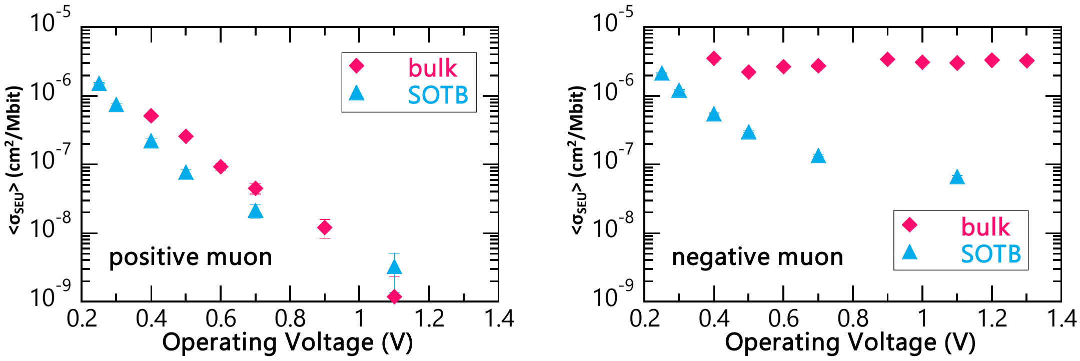

(a) positive muon

(b) negative muon

Figure 2.30: Measured SEU cross sections for the 65-nm bulk and SOTB SRAMs under 6.6 MeV (a) positive and (b) negative muon irradiation.

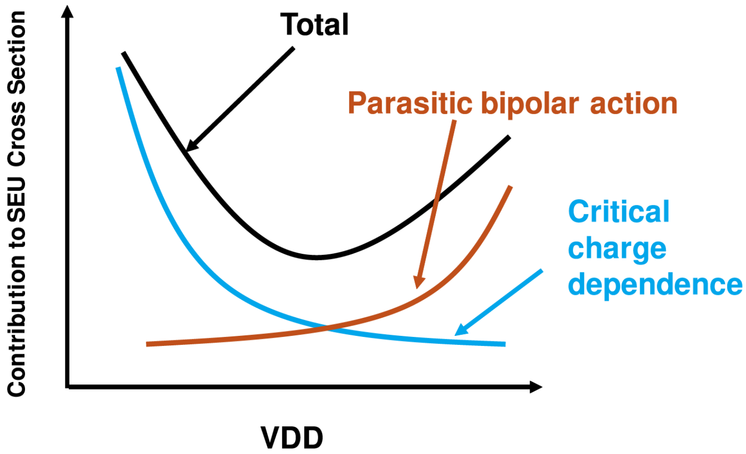

Figure 2.31: Conceptual illustration explaining the supply voltage dependence of negative muon-induced SEU cross-section for the bulk SRAM. The figure is taken from Figure 11 in [41].

2.5 Conclusion

We measured the kinetic energy and the supply voltage dependence of the SEUs induced by both negative and positive muons on 65 nm SOTB SRAMs in the incident muon kinetic energy range of 5.6–8.8 MeV. The accelerated SEU test using negative muons was performed with high statistics by means of an intense and high-quality negative muon beam at the J-PARC MUSE facility.

The experimental results showed that the negative muon experimental SEU cross sections are two to four times larger than the positive muon SEU in the case where the muons stop in the SRAM chips, and both SEU cross-sections had peaks around 6.6 MeV. The difference seen at 6.6 MeV became large with the increasing supply voltage. On the contrary, the negative and positive muon SEU cross-sections were almost the same, regardless of the supply voltage, at an incident kinetic energy over 8.0 MeV, where the fraction of muons passing through the device was large.

The measured negative and positive muon SEU cross-sections for the bulk and SOTB SRAMs were compared. The observed differences between the positive and negative muons were then discussed. The experimental results indicated that negative muons have a significantly larger impact on the SEU occurrence in the bulk SRAM compared to the SOTB SRAM due to the parasitic bipolar actions induced by the secondary ions generated from the negative muon capture reaction. The SEU cross-section for the bulk SRAM was at least 6.5 times larger than that for the SOTB SRAM. For the two SRAMs, the negative muon SEU cross-sections were larger than the positive muon SEU cross-sections.

The measured data were compared to the previous works [24–29]. We found that the present data qualitatively supported the kinetic energy (momentum) dependence of the positive muon SEU cross-sections measured in the previous works (e.g., Figure 1.9a). The measured negative muon SEU cross-sections were compared to the simulation result with the negative muon in [29] (Figure 1.10). The previous simulation indicated that the secondary particles from the nuclear negative muon capture reaction predominantly contributed to the SEU occurrence when the incident muons stopped near the sensitive volume region. The experimental results showed that the negative muon SEU cross-sections were much larger than the positive muon SEU cross-sections around the peak incident kinetic energy of 6.6 MeV due to the capture reaction near the SV. Thus, our observation of the negative muon SEUs supports the previous simulation result. The experimental results clarified that the nuclear negative muon capture by constituent atoms in the device considerably causes SEUs, as predicted in [29].

3 Estimation of the SEU Rates for the 65 nm Bulk and UTBB-SOI SRAMs

3.1 Introduction

As mentioned in the previous Chapter 2, we successfully measured the experimental negative and positive muon-induced SEU data. The simulation of the muon-induced SEU was performed to analyze the experimental data of the SOTB SRAM,

In addition to the analysis, the muon SEU rates for the 65 nm bulk and UTBB-SOI SRAMs were estimated using the experimental data of both negative and positive muons. Several reports in the literature are devoted to the muon-induced SEU rate. The SEU rates for different technology nodes (65, 45, 32, 22, and 16 nm) were predicted by the simulation [25]. The prediction indicated that the muon SEU rates might become significant for 16-nm technology node. To test this prediction, Seifert et al. [28] conducted an experiment with a positive muon beam for 32 nm planar and 22 and 14 nm 3D tri-gate technologies. However, the estimated muon SEU rates for the 14 and 22 nm devices were negligible compared to neutron SERs. Gasiot et al. [27] reported the positive muon SEU rates for the 28 nm ultra-thin body and thin buried oxide (UTBB) FD-silicon-on-insulator (SOI) and bulk SRAMs with the measured error cross sections. However, the computed positive muon SEU rates were below 0.1 FIT/Mbit (FIT: Fault in Time, the SEU per 10^9 h at the ground level radiation environment). Trippe et al. [42] recently predicted the muon-induced SEU rates for a 28 nm SRAM by using their ion-calibrated model. The model reproduced the experimental positive muon SEU results well and was used for the muon SER prediction. The result showed that the muon SEU rate contributed to less than 2% of the neutron SEU rates in the worst case. Thus, the muon SEU rates for various technology devices were predicted with only the positive muon irradiation tests and simulation in the past works. In the present work, the muon SEU rates for the 65-nm bulk and UTBB-SOI SRAMs were estimated by using the experimental data of both negative and positive muons. The SEU rates were calculated with the method of combining a simple sensitive volume (SV) model [43] and Monte Carlo simulation with the Particle and Heavy Ion Transport code System (PHITS) [9]. The experimental data were used to calibrate the calculated SEU rates. The estimated muon-induced SEU rates were compared to the neutron SEU rates measured with the white neutron beam [44] to investigate the fraction of the muon SEU rates to the neutron SEU rates.

Next, the muon transport simulation in a five-story building was performed to predict the muon SEU rates under a more realistic environment. The muon flux on each floor was then estimated. The muon SEU rate on the first floor was predicted. Moreover, the change in the ratio of the muon SEU rate to the neutron SEU rate is discussed in terms of the flux attenuation in the building.

First, we describe the simulation method and compare the results with the experimental result. Second, a method of predicting the SEU rates in the open air and the building is described, and the results are presented. Third, the predicted muon SEU rates are compared with the measured neutron SEU rates for the same device reported in [44] to clarify the contribution of muons to the overall SEU rates.

3.2 Simulation Method

The experimental data were analyzed based on the (SV) model [43] using the Monte Carlo simulation with PHITS code ver. 2.95 [9], which will be hereafter referred to as the PHITS-SV method. PHITS was successfully used in the recent simulations of neutron-induced soft errors [44–48]. We describe herein the model used in the present work, PHITS, and the simulation configuration.

3.2.1 PHITS

PHITS is a Monte Carlo particle transport simulation code widely used in various research fields. PHITS can simulate the transport of most particle species and the nuclear reactions using several nuclear reaction models and data libraries. Muon interaction models have recently been implemented in PHITS [10].

The calculation process of the negative muon capture reaction implemented in PHITS is described herein. As mentioned in Section 1.4, the captured negative muon cascaded down to the 1s orbital while emitting characteristic X-rays. The muonic atom cascade program [49] was employed to simulate the emission of the characteristic X-rays from the cascade of the captured muon in the atomic orbitals. After that, the fraction of the captured negative muons decays and the remaining negative muons are absorbed by the nucleus. The decay rate of the negative muon,

Λ_d, is calculated as follows:

$$\Lambda_\mathrm{d} = H \times \frac{1}{\tau_\mu}, \tag{3.1}$$

where, τ_μ represents the mean lifetime of the muon ($= 2.2 \times 10^{-6}$ s), and H represents the Huff factor. The H value is taken from [50]. For the nuclei whose experimental values are not available, H is calculated using the Goulard-Primakoff equation [51]. When a muon is captured by a nucleus, a proton in the nucleus is converted to a neutron through the following elementary process:

$$p + \mu^- \rightarrow n + \nu_\mu. \tag{3.2}$$

In PHITS, a proton in the nucleus is randomly selected and changed to a neutron with the added excitation energy of the nucleus. The time evolution of the nucleons is calculated by the JAERI quantum molecular dynamics (JQMD) model [11] The sequential evaporation process is calculated by the generalized evaporation model (GEM) [12]. Thus, the emission of the secondary ions from the capture reaction is simulated by PHITS. In this chapter, the simulation was performed with default QMD plus GEM. The QMD was improved by implementing a surface coalescence model (hereafter referred to as the modified-QMD, MQMD) in previous works [52, 53] to reproduce the experimental data of the neutron-induced nuclear reactions. The MQMD plus GEM will be applied to the simulation in Chapter 4.

The delta ray generation (i.e., secondary electrons with sufficient energy) can be considered in PHITS to accurately simulate the energy deposition in SV. Consequently, the energy deposition by the delta rays spread far away from the muon path. In PHITS, the delta ray generation with a kinetic energy over 1 keV is simulated using the model proposed by Butts and Katz [54]. The delta ray generation in the chip was considered in the present work.

3.2.2 Sensitive Volume (SV) Model

In this model, the sensitive volume is defined in each SRAM cell. All deposited charges in the SV were assumed to be collected to the drain node without the carrier simulation. The SEU occurrences were judged using the SV model, in which the SEU was assumed to occur when the total charge deposited in the defined SV exceeded the critical charge Q_c. In the PHITS simulation, the deposited energy in the SV was output, and the energy must be converted into charge. The minimum energy to generate an electron-hole pair is 3.6 eV. The deposited charge q is calculated as:

$$q \text{ [fC]} = \frac{e}{3.6 \times 10^{-6}} \times E_\mathrm{d} \text{ [MeV]} = 44.5 \times E_\mathrm{d} \text{ [MeV]}, \tag{3.3}$$

where, e represents the elementary charge ($= 1.602 \times 10^{-19}$ C) and E_{d} represents the deposited energy in the SV.

3.2.3 Geometry Used in PHITS Simulation

Figure 3.1 illustrates the configuration of the tested chip used in the PHITS simulation. A single chip was used in the simulation as a mock-up for the device board. The chip covered with resin was placed on the board layer. The planar muon source with a 10 mm × 10 mm area was placed in air 300 mm away from the board layer. The muons entered the test device vertically via a 75-μm-thick Kapton film located in the beam exit. The incident muon momentum was determined by sampling using a normal distribution with 5% standard deviation to reproduce the muon beam of the MUSE facility.

Figure 3.2 schematically depicted the inner structure of the chip. The chip had an area of 2800 μm × 2400 μm and consisted of 12-Mbits of SOTB SRAM cells. A single SRAM memory cell measured 1.04 μm × 0.52 μm × 0.012 μm. A total of 12-Mbit cells were configured in a 2D grid on a 0.010-μm-thick silicon dioxide insulation layer. A 300-μm-thick silicon substrate was located under a 0.010-μm-thick silicon dioxide insulation layer. A 0.35-μm-thick silicon dioxide insulation layer was also placed above the SRAM memory cells, and a 2.43-μm-thick metal layer consisting of copper and silicon dioxide was above a 0.35-μm-thick silicon dioxide insulation layer. With reference to the previous work [44, 45], the SV of the SRAM memory cell was defined as the source and drain regions, and the SOI layer under the gate of the off-state NMOS and PMOS. The SV size measured 0.34 μm × 0.08 μm and 0.26 μm × 0.12 μm for the NMOS and PMOS areas, respectively. The thickness of both SVs was 0.012 μm, which was equal to that of the SOI layer.

3.3 Simulation Results and Comparison with Experimental Results

The kinetic energy dependence and the Q_{c} dependence of the muon-induced SEU cross-section are calculated herein. The kinetic energy dependence is compared to the experimental dependence. The simulation results are shown and discussed.

3.3.1 Range of Muons in the Device Board

First, the range of positive muons with various momenta in the device board was calculated before the experiment to decide on the incident muon kinetic energy. In this calculation, the pencil beam of the mono-energetic muons was incident on

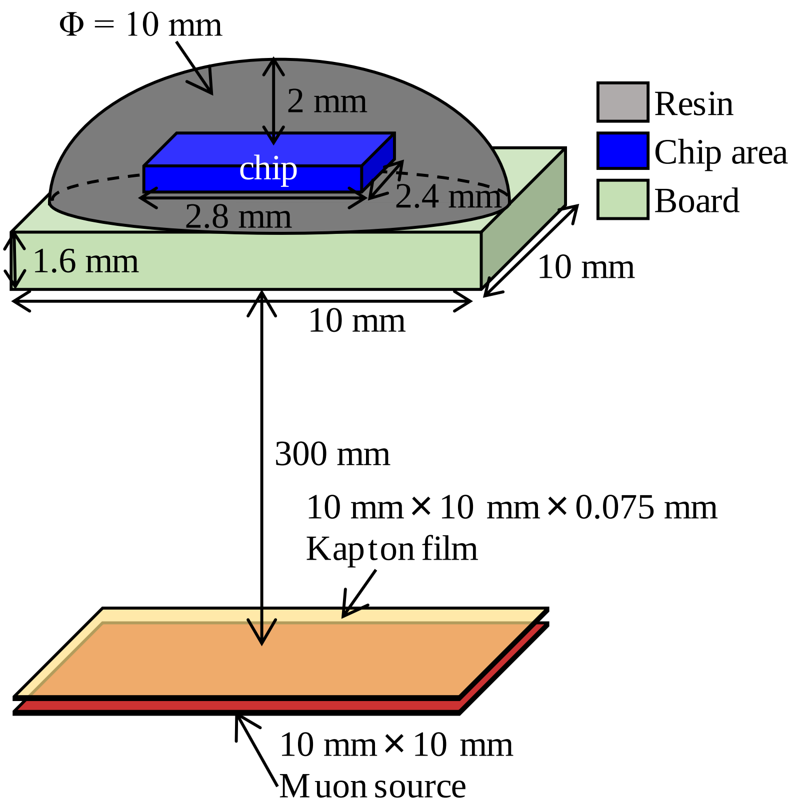

Figure 3.1: Configuration of the test device used in the PHITS simulation.

the center of the device board with the same direction(Figure 3.1). Figure 3.3 shows the calculated range of the muons in the device board. The ranges of the negative and positive muons were absolutely equivalent in the PHITS simulation. Hence, the results of the negative muons was not presented. The legend in the right side of the graph represents the materials in each depth. The SVs of the SRAMs with a 12 nm thickness were placed at the upper part of the chip. The result indicated that the muons with the kinetic energy of 6.6 MeV stopped near the SVs. The charged particles deposited the most of its energy before stopping, and the negative muons were captured by the nuclei when they stopped. Hence, the muons with the 6.6 MeV (38 MeV/c) were predicted to have a maximum effect on the SEU occurrence in this experimental setup.

3.3.2 Kinetic Energy Dependence

In Figure 3.4, the simulated kinetic energy dependence of the mean SEU cross-sections was compared with the experimental result. The critical charge Q_c in

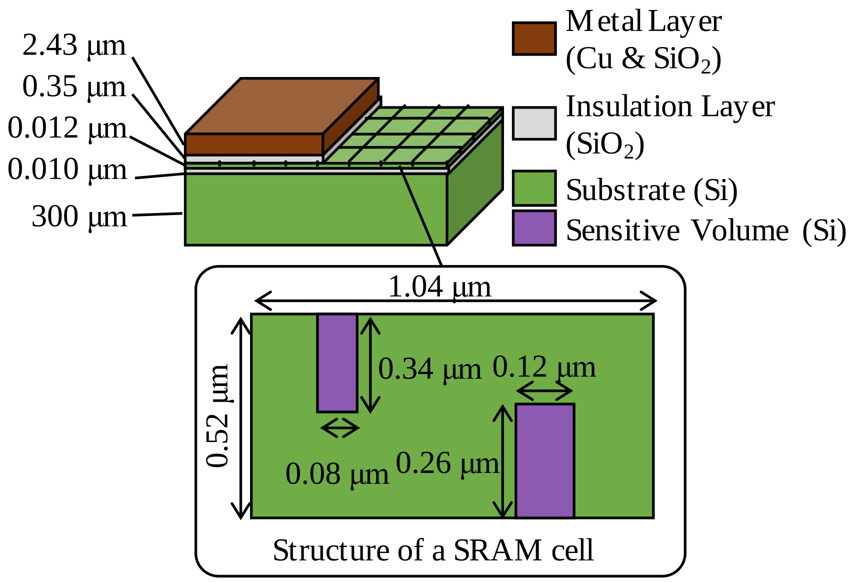

Figure 3.2: Configuration of the chip used in PHITS simulation. 12-Mbit SOTB SRAMs are placed on a chip. Thickness of the sensitive volume is 0.012 μm, and 0.010 μm insulation layer is placed just under the sensitive volume.

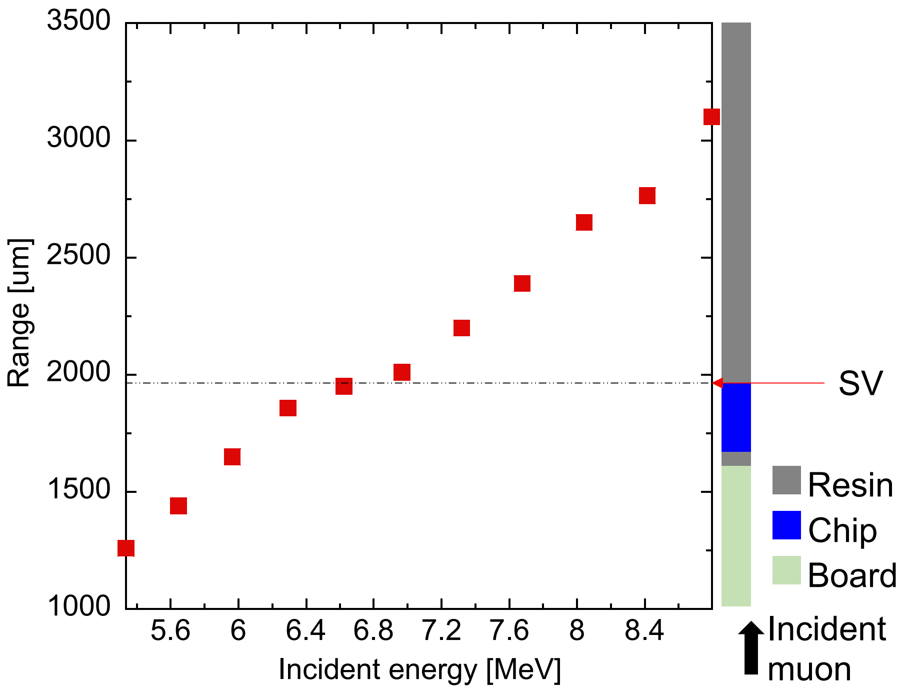

Figure 3.3: Range of muons in the device board.

the simulation was chosen as 0.08 fC (the deposit energy of 1.8×10^{-3} MeV in the SV) to reproduce the ratio of the negative and positive muon-induced SEU cross-sections at 6.6 MeV. The orange-full and green-dashed lines denote the simulated negative and positive muon SEU cross-sections, respectively. The simulated negative muon SEU cross-section at 6.6 MeV was normalized to the measured one. At first glance, the overall behavior of the SEU cross-section was reproduced generally well by the PHITS-SV simulation. Figure 3.5 shows the ratio of the negative and positive muon SEU cross-sections. The experimental ratio was reproduced reasonably well by the present simulation, except at 5.3 MeV, where the experimental statistics was not enough. The contribution ratio of the simulated negative muon-induced SEU was induced by the capture reactions or direct ionization as shown (Figure 3.6). The fraction of the SEUs induced by the muon capture rapidly decreased when the incident kinetic energy of the negative muons increased (i.e., the negative muon passed through the SV of the SRAMs). In this case, the SEUs became mainly induced by direct ionization. Figure 3.6 can be compared to the previous simulation shown in Figure 1.10 (Figure 5 of [29]). The simulation in the previous work generally showed a similar tendency in the kinetic energy dependence of the contribution of the direct ionization and capture reaction to the negative muon-induced SEUs. The maximum contribution to the SEUs was lower compared to that in the previous work because mono-energetic muons were assumed in the previous work, and the muon beam with a normal momentum distribution was used in our simulation.

Next, we examined the species of the charged particles and the secondary ions influencing the low-energy muon-induced SEUs using the present PHITS-SV simulation. Figure 3.7 shows the results at two typical incident kinetic energies, 6.6 and 8.4 MeV. The contribution of the electrons included both the decay electrons and the delta rays in the negative muon incidence, while only the delta rays are the electron source in the positive muon incidence. Some obvious differences between negative and positive muons were seen in the charged particles and secondary ions influencing the SEUs.

As shown in Figure 3.7a, the direct ionization of the negative muons contributed to the SEUs by approximately 20%, while approximately 70% of the SEUs was caused by the secondary charged particles and heavy recoils generated by the negative muon capture reaction at 6.6 MeV, where the incident muons stopped near the SV of the SRAM. Helium ion has the predominant contribution among all particle and ion species. By contrast, direct ionization was predominant in the positive muon incidence, and the influence of the decay positrons was negligibly small in Figure 3.7b. This suggests that the electron contribution in the negative muon incidence mainly came from the delta rays, but not from the decay electrons.

In Figures 3.7c and 3.7d, show that the electrons dominantly contribute to the

SEUs induced by both negative and positive muons at 8.4 MeV, where the muons passed through the SV of the SRAM. The electrons were expected to be the delta rays in both case, because the effect of the decay positrons was negligible in the positive muon incidence. In addition, the relative contribution of the secondary ions and the heavy recoils in the negative muon incidence was much lower than that at 6.6 MeV. This is consistent with the experimental result that the measured negative and positive muon SEU cross-sections were almost the same at the incident momenta higher than 7.7 MeV. These analyses confirmed that the delta rays predominantly contributed to the SEUs when the muons passed through the SV of the SRAM. If the delta ray generation is neglected in the PHITS-SV simulation, the calculated SEU cross-sections will become much smaller at high momenta compared to the result of Figure 3.4 and cannot reproduce the measured kinetic energy dependence. In other words, it is important to consider the delta ray generation in the SEU simulation, especially in a device with a low Q_c.

Thus, the PHITS-SV simulation with $Q_c = 0.08$ fC was found to reproduce well the kinetic energy dependence of the measured muon-induced SEU cross-sections (Figure 3.4). The Q_c value was estimated by fitting the PHITS simulation to the experimental ratio of the negative and positive muon SEU cross-sections at 6.6 MeV. Hence, the Q_c value depends on the accuracy of the physics models implemented in PHITS and the SV assumption in the simulation. In addition, the Q_c value is considerably low compared to the general Q_c trend of the 65-nm technology SRAMs. In the present simulation, we approximated the charge collection process by the simple SV model and have not simulated it accurately after the initial charge deposition. The previous work on SOI devices pointed out the importance of parasitic bipolar effects leading to the enhancement of the charge collection at the drain [55]. Therefore, device simulation will be necessary for a further detailed discussion.

3.3.3 Critical Charge Dependence

The critical charge dependence of the SEU cross-sections were calculated at the two incident kinetic energies of 6.6 and 8.4 MeV. Figures 3.8 and 3.9 show the Q_c dependence of the SEU cross-sections and the contribution ratio of the charged particles to the SEU as a function of Q_c at the incident kinetic energy of 6.6 MeV. The muons and electrons (i.e. direct ionization of muons) mainly contributes to the SEU occurrence below a Q_c of 0.05 fC. In contrast, above a Q_c of 0.3 fC, the muon direct ionization did not contribute to the SEU occurrence. The contribution of the secondary ions became larger with the increase because they can deposit sufficient charges to induce the SEUs due to their higher stopping power compared to the muon direct ionization. This result showed a good agreement with the measured supply voltage dependence at the same kinetic energy shown in Figure 2.28.

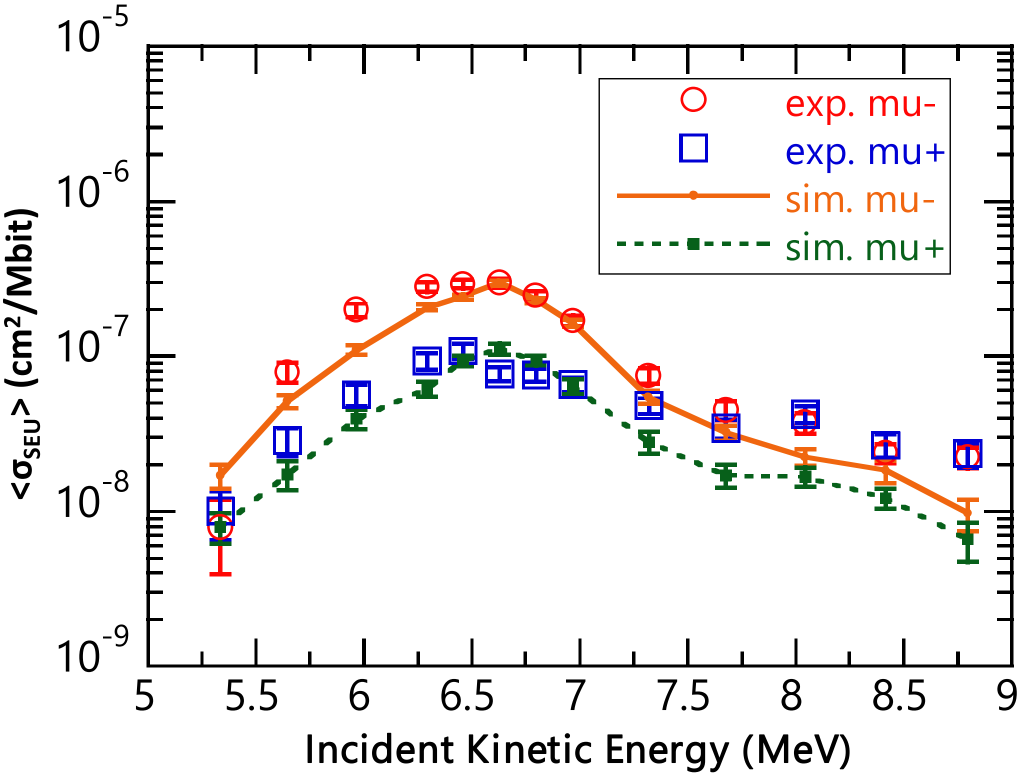

Figure 3.4: Comparison between the simulated kinetic energy dependence and the measured one.

In the experiment, the negative muon SEU cross-sections were significantly larger than that of the positive muon in the higher voltage corresponding to the high Q_c. Our simulation result clearly illustrated that the difference in the experiment was caused by the negative muon capture reaction by the nuclei.

The same result at the incident kinetic energy of 8.4 MeV are shown in Figures. 3.10 and 3.11. The electrons, which are the delta rays discussed in Subsection 3.3.2, were predominant to the SEU occurrences below 0.1 fC, indicating that considering the delta rays plays an important role in simulating SEUs, especially in a device with a low Q_c. Above 0.2 fC, only helium and aluminum ions contributed to the SEU. However, this did not agree with the experimental result as (Figure 2.29) because the effect of the negative muon capture reaction by the nuclei was not observed in the kinetic energy of 8.4 MeV during the experiment. This disagreement was likely caused by the difference of the kinetic energy distribution between the simulation and the experiment. Hence, it is desirable to measure the kinetic energy distribution of the muon beam used in the experiment for a more

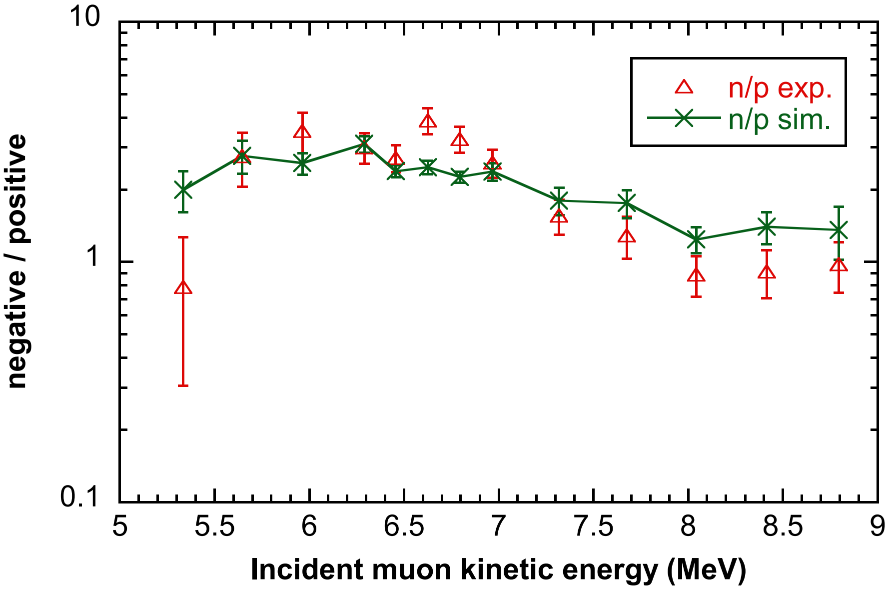

Figure 3.5: Ratio of negative muon SEU cross sections to positive muon ones as a function of incident kinetic energy.

accurate simulation.

3.4 Muon-induced SEU Rates

We proposed the PHITS-SV method to predict the SEU cross-sections. The same kinetic energy distribution of the incident muons in the measurement was used for a comparison with the measured mean SEU cross-section given by Eq. (2.1).

Figures 3.4 and 3.12 show comparisons of the simulated and measured mean SEU cross-sections as a function of the incident kinetic energy for the SOTB and bulk SRAMs, respectively. The critical charge Q_c, which is an adjustable parameter in the PHITS-SV method, was chosen to reproduce the ratio of the negative and positive muon-induced SEU cross-sections measured at 6.6 MeV. Consequently, the Q_c value was found to be 0.08 and 1.5 fC at the operating supply voltage of 0.5 V for SOTB and bulk SRAMs, respectively. The overall behavior of the measured SEU cross-section was reproduced well by the simulation (Figure. 3.4 and 3.12) by normalizing the simulated mean SEU cross-section to the measured cross-section at 6.6 MeV. The normalization factor was used to estimate the SEU rates at the ground level.

The PHITS-SV method can also be applied to estimate the negative and positive muon SEU rates for 65-nm bulk and SOTB SRAM at ground level. The

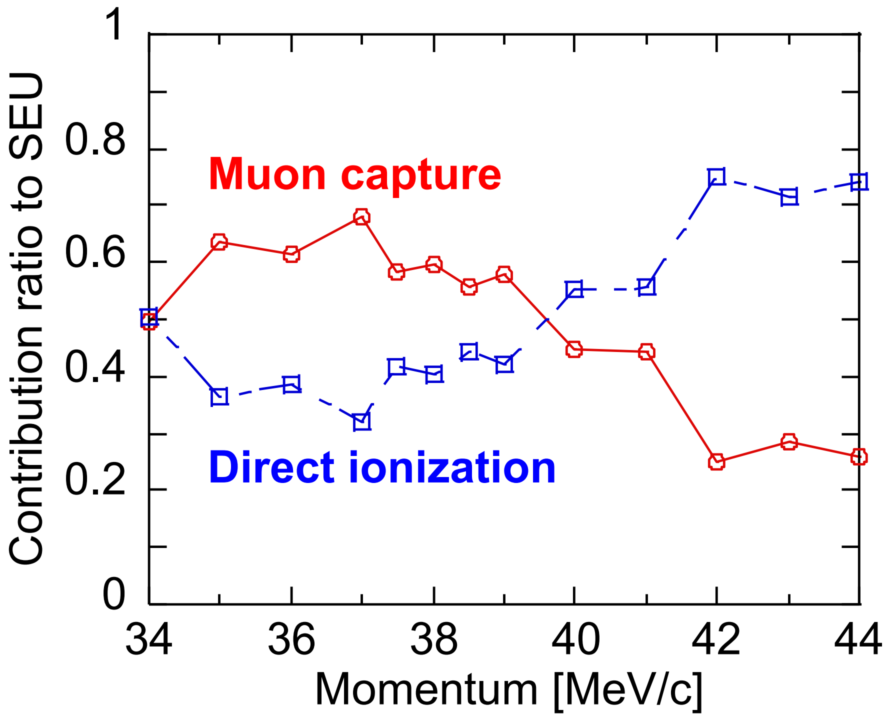

Figure 3.6: Contribution of the muon capture reaction and direct ionization to simulated negative muon-induced SEUs.

PHITS-SV simulation was performed by the following procedure to calculate the muon SEU rate at the ground level: the muon energy spectrum at ground level is obtained by the PHITS-based analytical radiation model in the atmosphere (PARMA) model [5–7]. Figure 1.4 shows the calculated omnidirectional energy spectra of muons and neutrons in Tokyo, Japan. Muons with the PARMA energy spectrum are then vertically injected on the 65-nm SRAM chip. The number of upset events, $N(q)dq$, with the charge deposited in the SV in $[q, q + dq]$ is obtained. Subsequently, the SEU rate is calculated as a function of the operating supply voltage V_{op} by choosing Q_c as follows:

$$SEU\ rate(V_{\mathrm{op}}) = C_{\mathrm{nor}} \times \frac{F \times A}{N_{\mathrm{in}} \times N_{\mathrm{bit}}} \int_{Q_c(V_{\mathrm{op}})}^{\infty} N(q)dq \tag{3.4}$$

where, F is the total flux of the incident muons in units of cm^{-2}sec^{-1}; A is the surface area of the test board; N_{in} is the number of the incident muons; N_{bit} is the number of bit cells in the device; and C_{nor} is the normalization factor given by the ratio of the measured mean negative muon SEU cross-section to the simulated one at the incident kinetic energy of 6.6 MeV.

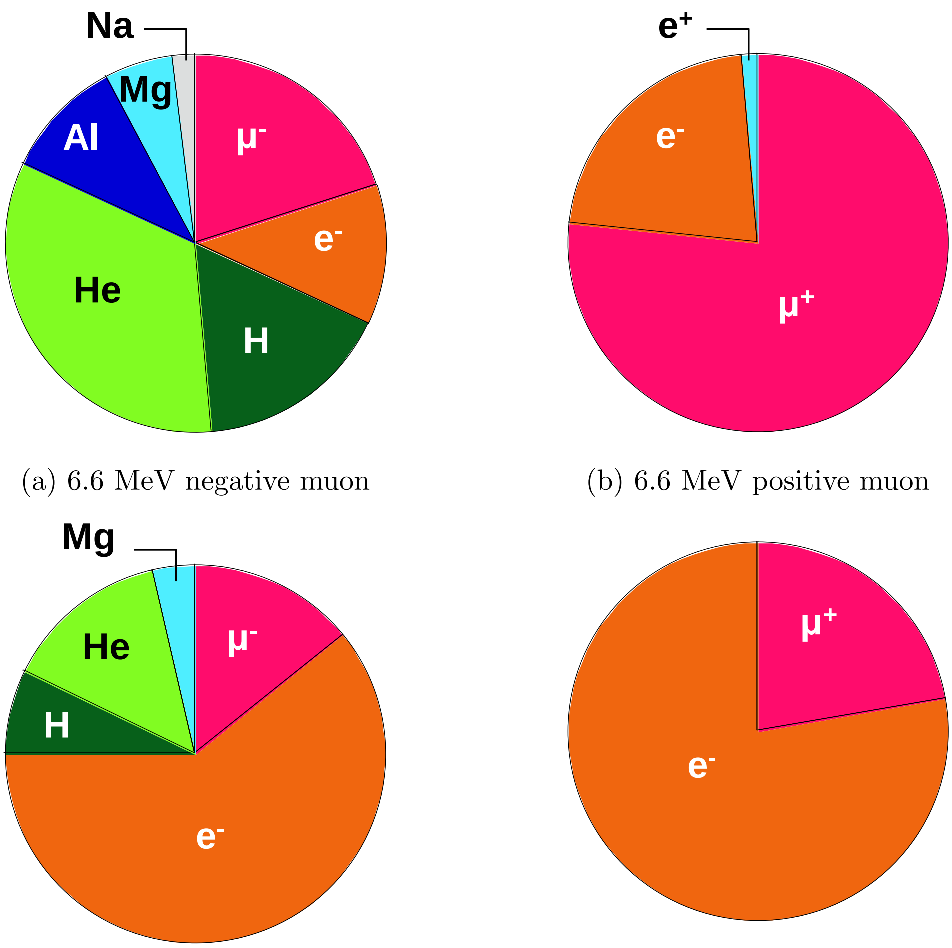

(a) 6.6 MeV negative muon

(b) 6.6 MeV positive muon

(c) 8.4 MeV negative muon

(d) 8.4 MeV positive muon

Figure 3.7: Contribution of individual charged particles and secondary ions to negative and positive muon induced SEUs.

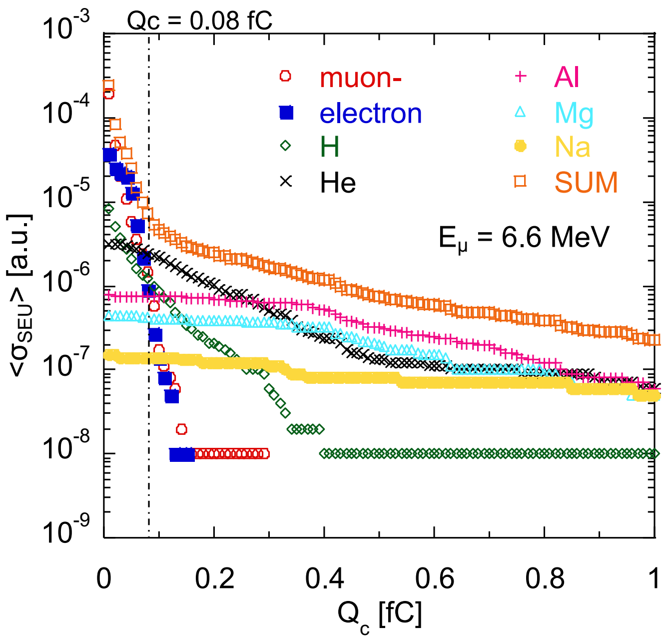

Figure 3.8: Simulated critical charge dependence of SEU cross sections at an incident kinetic energy of 6.6 MeV.

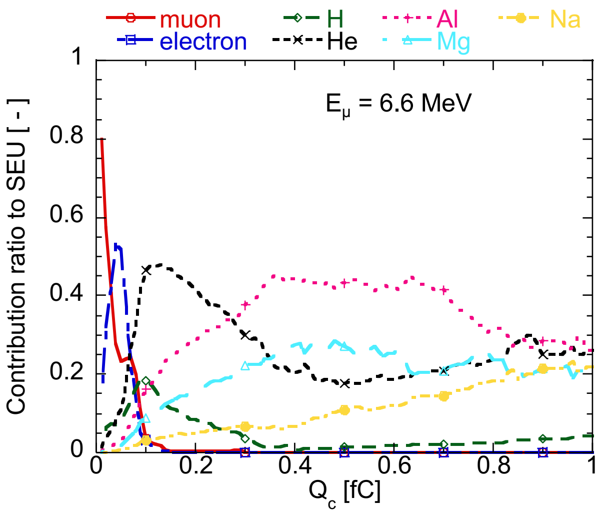

Figure 3.9: Contribution of individual charged particles and secondary ions to negative muon induced SEUs at the incident kinetic energy of 6.6 MeV.

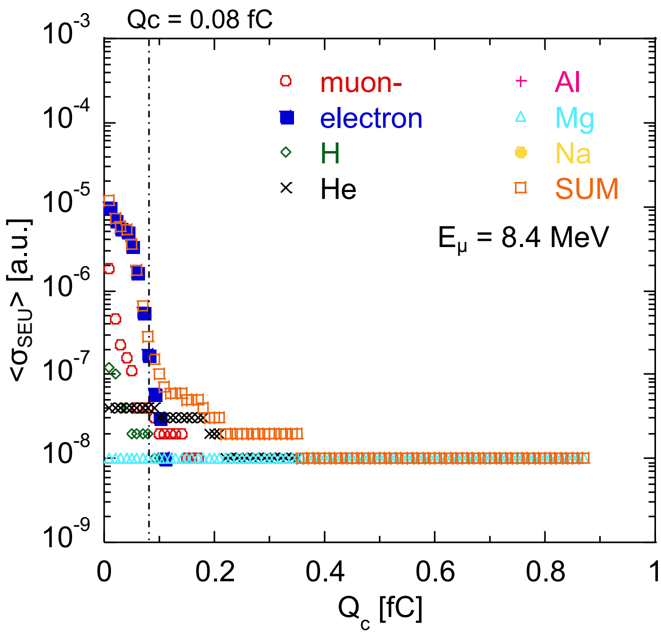

Figure 3.10: Simulated critical charge dependence of SEU cross sections at an incident kinetic energy of 8.4 MeV.

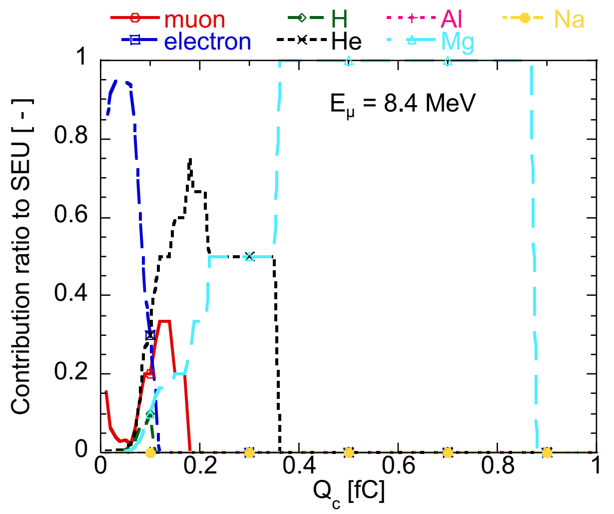

Figure 3.11: Contribution of individual charged particles and secondary ions to negative muon induced SEUs at the incident kinetic energy of 8.4 MeV.

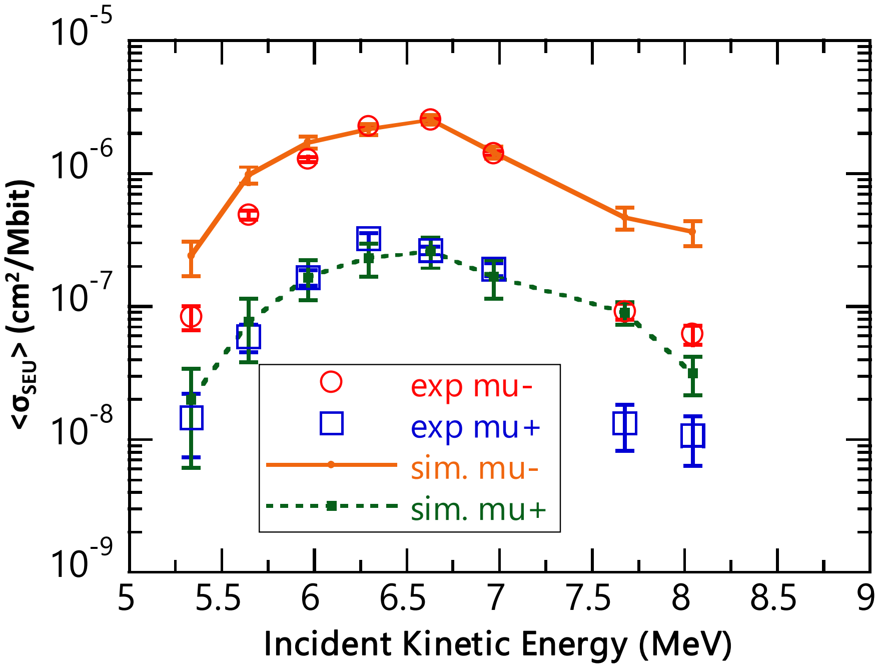

Figure 3.12: Comparison between the simulated kinetic energy dependence and the measured one of bulk SRAM.

3.4.1 Open-air SEU Rate

The estimated muon SEU rates for the SOTB and bulk SRAMs were compared to the neutron SEU rates measured for the same SRAMs in Figures 3.13 and 3.14, respectively. The neutron SEU rates were measured using a white neutron beam at the RCNP in Osaka University. The measurement details were described in [44].

First, we evaluated the negative and positive muon SEU rates for the two SRAMs. The negative muon SEU rates were larger than the positive muon SEU rates because of the larger SEU cross-sections caused by the negative muon capture process in Figures 3.13 and 3.14. The ratios of the negative muon SEU rates for the SOTB SRAM to the positive muon SEU rates were 3.6 and 5.8 times at 0.5 and 0.7 V operating supply voltages, respectively. The charge deposited by the secondary ions generated from the negative muon capture was much larger than that deposited by muon direct ionization. This shows that negative muons can deposit sufficient charge to cause SEUs, even at a higher operation voltage (i.e., at a larger critical charge). Consequently, the difference between the negative and positive muon SEU rates became larger for higher-voltage operation. This result indicates that a careful consideration of the negative muon capture reactions plays an important role in properly and accurately estimating the muon SEU rates. However, in lower operating voltages of 0.3 and 0.25 V, both the SEU rates were almost the same because the direct ionization of the muons caused SEUs mainly in the low critical charge. Meanwhile, for the bulk SRAM, the negative muon SEU rates were approximately 8 and 247 times larger than the positive muon SEU rates at the operating voltages of 0.5 and 0.9 V, respectively. This significant difference between the bulk and SOTB SRAMs can be explained straightforwardly by the difference in the supply voltage dependence of negative and positive muon SEU cross-sections (Figure 2.30). The present result indicates that the impact of the negative muon capture reaction for the bulk SRAM is much more significant than that for the SOTB SRAM.

Next, the estimated muon SEU rates were compared to the neutron SEU rates in Figures 3.13 and 3.14. The PHITS-SV method can be also applied to estimate the neutron SEU rates. For a further validation of the method, the neutron SEU rate was calculated for the bulk SRAM using the same values of Q_c and C_{nor} as in the muon SEU rate estimation. Consequently, the calculated neutron SEU rate underestimated the experimental rate by a factor of approximately two (Figure 3.14). However, this was not serious in terms of the comparison between the neutron and muon SEU rates in Figures 3.13 and 3.14 because the difference between them was significantly large. The muon SEU rate for the SOTB SRAM had the highest contribution at the operating voltage of 0.3 V among those estimated in the present work. Even in this case, we found that the contribution from the muons was approximately 1%.

The muon-induced SEU probability has a peak around 6.6 MeV as shown in Figures 3.13 and 3.14. The flux of such low-energy negative muons is 2.8×10^{-7} /cm^2/s at the ground level, while that of neutrons in the energy range 1-1000 MeV is 4.0×10^{-3} /cm^2/s as shown in Figure 1.4. The low-energy negative muon flux is thus approximately 0.007% of the neutron flux with the energy of 1-1000 MeV; however, the negative muon SEU rate was approximately 1%. This suggests that the negative muons have higher SEU cross-sections compared to the neutrons. We additionally calculated the SEU cross-sections of the mono-energetic low-energy negative muons with the calibrated PHITS-SV model to check this speculation. The calculated muon SEU cross-sections were compared to the neutron SEU ones in Figure 3.15. The neutron SEU cross-sections were calculated by means of the multiple SV (MSV) model for the same 65-nm bulk SRAM as used in this work [56]. In the MSV model, the sensitive volume was divided in several volumes, and the charge collection efficiency for each volume was determined by a device simulator. The neutron SEU cross-section has a steep slope around several MeV, and gradually increases with increasing the incident energy. In contrast, the negative muon with only a narrow energy region affects the SEU occurrence, and

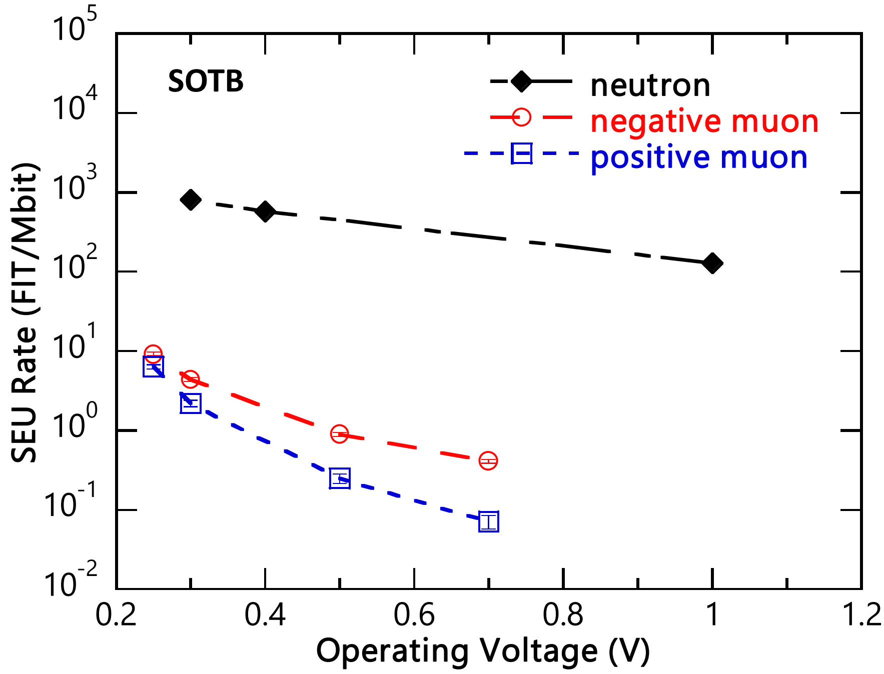

Figure 3.13: Open-air ground level SEU rate induced by cosmic-ray neutron, negative muon, and positive muon on the 65-nm SOTB SRAM.

its cross-section was considerably higher than the neutron. It is because that the stopping muon in the SV can conclusively deposit the charge which exceeds Q_c in the SV with the direct ionization, and the nuclear reaction (i.e., the nuclear muon capture reaction) probability is higher than that of neutrons.

3.4.2 Indoor SEU Rate

We performed a muon transport simulation in a five-story building using PHITS to evaluate the muon SEU rates in a realistic radiation environment, where the SRAM devices are operated. Figure 3.16 shows the structure of the building made of concrete and room air, which is the same as in [57]. The floor and the wall were 15 and 20 cm thick, respectively. The building height was 19.3 m, and the width and length were 53.6 and 15.8 m, respectively. The building was irradiated by muons having the energy and zenith angular distributions on the ground given by the PARAMA model. The fluxes of the negative and positive muons on each floor were calculated.

The calculated energy spectrum on the first floor was compared to that in the open air in Figure 3.17. The flux on the first floor above 100 MeV was lower than

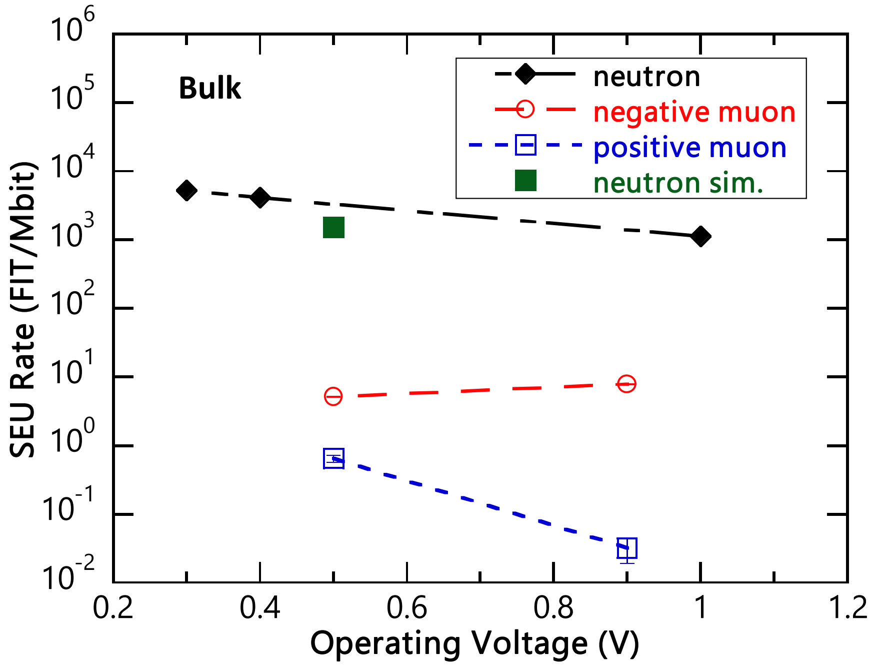

Figure 3.14: Open-air ground level SEU rate induced by cosmic-ray neutron, negative muon, and positive muon on the 65-nm bulk SRAM.

that in the open air due to the energy loss in the building. Hence, the flux on the first floor less than 100 MeV slightly increased compared to that in the open air. Our previous experimental result indicated that the SEU cross-section for the device board peaked around the incident kinetic energy of 6.6 MeV (Figures 3.4 and 3.12). Thus, the muon flux below 10 MeV is crucially important for the SEU occurrence. Figure 3.18 shows the muon fluxes below 10 MeV on each floor and in the open air. The fluxes in the building were larger than the open-air flux, and the floor dependence was weak. Although the maximum flux value was given on the third floor, the difference from the open-air flux value was less than approximately 20%. The simulation result indicates that it is difficult to reduce the low-energy muon flux by shielding materials because the high-energy muons slowed down to the low-energy region due to the energy loss in shielding materials. Consequently, the muon SEU rate was found to be almost constant, regardless of the floor number. On the contrary, the previous simulation [57] presented that the neutron SEU rate on the first floor decreases to 13% of that in the open air. Based on the prediction [57], we conclude that the muon SEU rate on the first floor was at most 10% of the neutron SEU rate for the 65-nm SOTB SRAM with an operating voltage of 0.3 V, at which the muon has the highest contribution

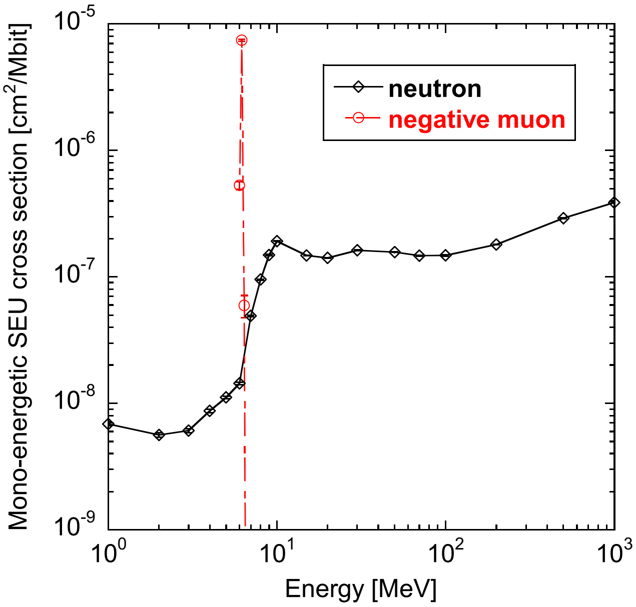

Figure 3.15: Mono-energetic negative muon and neutron-induced SEU cross-section for the 65-nm bulk SRAM. The neutron SEU cross-sections were taken from [56]. The operation voltage was 0.9-V in the calculation.

among the estimated SEU rates (Figure 3.13).

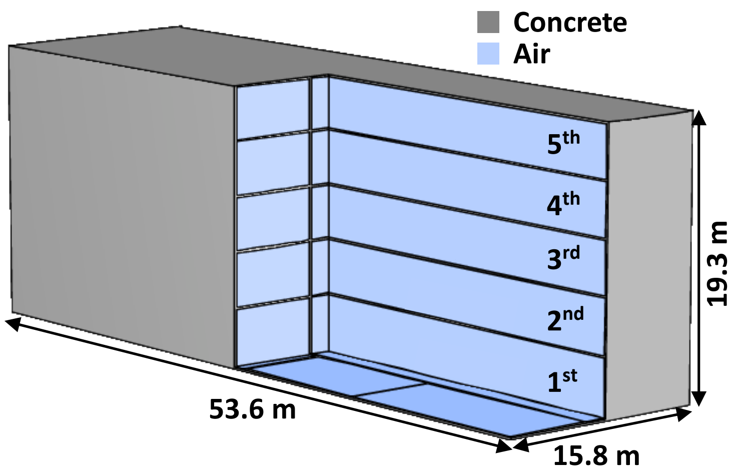

Figure 3.16: Simulation structure of five-story building made of concrete and room air.

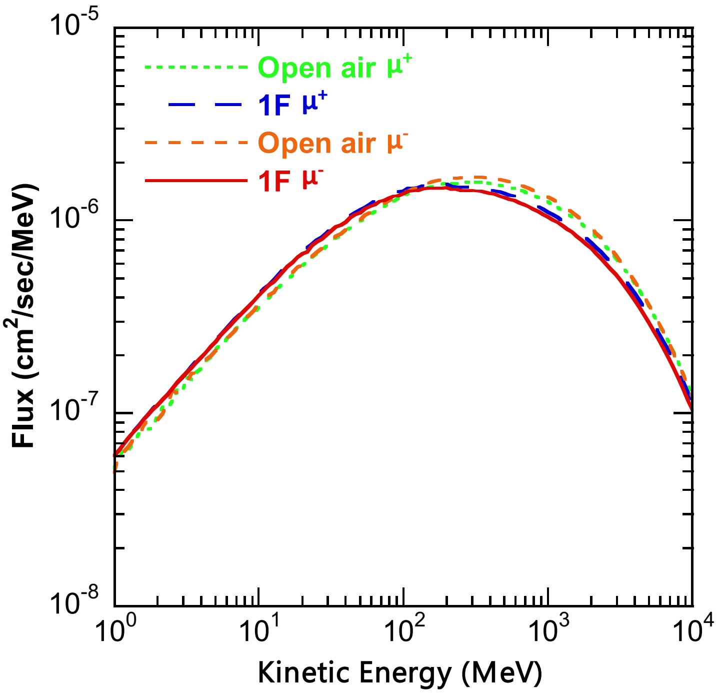

Figure 3.17: Comparison of the calculated negative and positive muon energy spectra of the first floor and in the open-air.

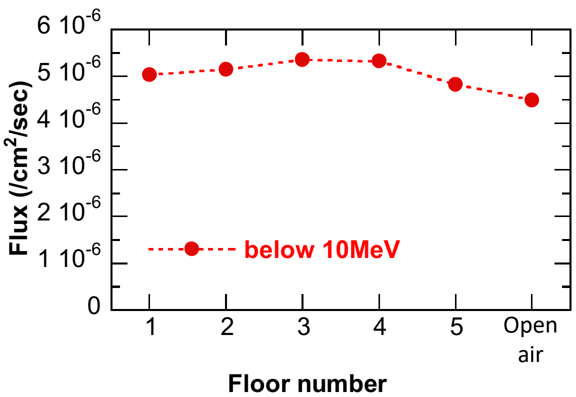

Figure 3.18: Calculated muon fluxes below 10 MeV on each floor and in the open air.

3.5 Conclusion

The analysis of the experimental muon-induced SEU cross-sections was performed by means of the Monte Carlo simulation PHITS plus the simple SV model. The simulation showed a generally good agreement with the kinetic energy dependence of the measured SEU cross-sections for both the positive and negative muons. In addition, we examined the species of the charged particles and the secondary ions that influenced the low-energy muon-induced SEUs. These simulation results clarified that the negative muon capture by the constituent atoms in the device considerably causes SEUs. Hydrogen and helium ions have the predominant contribution among all particles and ion species.

Furthermore, the negative and positive muon-induced SEU rates for the 65-nm bulk and SOTB SRAMs in the terrestrial radiation environment were estimated using the PHITS-SV simulation based on the experimental SEU cross-sections. For the two SRAMs, the negative muon SEU rates were found to be larger than the positive muon SEU rates. It should be emphasized that the negative muon SEU rate was 247 times larger than the positive muon SEU rate for the 0.9 V bulk SRAM. Hence, it is important to consider the effect of the negative muons on the SEU appropriately for the accurate prediction of the muon-induced SEU rates. The estimated muon SEU rate was also compared to the measured neutron SEU rate. In conclusion, the muon SEU rates for the 65-nm technology devices were almost negligibly small compared to the neutron SEU rates, even if the contribution from the negative muons is considered. This result is generally consistent with other predictions by the previous works [25, 27, 28, 42].

The muon transport simulation in the five-story building was performed to evaluate the muon SEU rates in a realistic radiation environment. The result showed that the indoor muon flux below 10 MeV is almost constant, regardless of the floor number. Meanwhile, the simulation in [57] demonstrated that the neutron SEU rate on the first floor is 13% of the open-air SEU rate. Consequently, the muon SEU rate was estimated to be at most 10% of the neutron SEU rate on the first floor.

4 Measurement of Energy Spectra of Hydrogen Isotopes from Nuclear Muon Capture Reaction in ^{nat}Si

4.1 Introduction

As mentioned in Chapter 3, a series of simulations with the PHITS-SV method were performed to estimate the SEU rates at ground level for the 65-nm technology SRAMs in addition to the analysis of the experimental SEU data. The results clearly showed that the secondary light ions from the nuclear negative muon capture reaction on silicon nuclei have the predominant contribution to the occurrence of the muon-induced SEUs.

Our recent experiment [58] investigated the technology scaling of negative and positive muon-induced SEU cross-section. A 28 nm technology planar SRAM was tested at MUSE following the same procedure described in Chapter 2. The test demonstrated that the increasing rate of the negative muon-induced SEU cross-sections was 3.6 times from 65 to 28 nm technology, illustrating that the muon-induced SEU rate at the ground level increased with downscaling. On the contrary, the neutron-induced SEU rate per SRAM bit showed an opposite trend. Seifert et al. [59] experimentally predicted that the neutron SEU rate decreased to 0.6 times with one generation technology downscaling. The two tendencies of muons and neutrons indicate the possibility of the muon becoming the main cause of the soft error at the ground level in the future. Therefore, the muon-induced SEU rate for the future technology SRAMs must be estimated with a high accuracy.

Under these situations, the experiment was performed to accumulate the basic data of the fundamental physical process of the muon-induced SEU (i.e., the secondary light ions from the nuclear muon capture). The process is one of the most important parts of the muon-induced SEU simulation. In addition to the experiment, a validation of the model calculation implemented in PHITS was made by comparing the experimental data and the simulation. Finally, the effect of the model calculation on the SEU simulation was examined.

4.2 Previous Works on the Nuclear Negative Muon Capture Reaction

Many papers were devoted to the investigation on the charged particle emission from the nuclear muon capture reaction. Lifshitz and Singer [60, 61] developed a theoretical model to calculate the proton emission probability and the energy spectrum. The model considered both preequilibrium and compound-nucleus processes.

The experiments with photographic emulsions [62, 63] measured the spectra and the yield of the emitted charged particles; however, the selection of the target nucleus was limited due to the measurement method. Activation experiments [64, 65] measured the reactions (i.e., (μ^-, p), (μ^-, pn), (μ^-, $p2n$), (μ^-, α), and so on) probabilities by measuring radioisotopes induced by the nuclear muon capture reactions in various nuclei.

More recently, a experiment [66] with a tracking spectrometer was performed to measure the momentum spectra of protons and deuterons from the nuclear muon capture on the aluminum nucleus to estimate a noise rate during the experiment to discover the neutrino-less muon to electron conversion. The precision of the measured proton spectrum was better than 10% in the momentum range 100-190 MeV/c (5.3-19 MeV in the kinetic energy). For deuteron, the precision was better than 20% in 145-250 MeV/c (5.6-16 MeV in kinetic energy). Thus, the proton and deuteron emissions from the muon capture on aluminum was precisely investigated.

A few experimental data of the nuclear muon capture reaction on silicon, which is a main element of semiconductor devices, have been reported. S. Sobottka and E. Wills conducted an experiment to investigate the energy spectra of these ions [67]. A 3 mm^t Si(Li) detector was irradiated by a muon beam. Moreover, a spectrum of the energy deposition by the light ions and recoiled nuclei in the detector was measured (Figure 4.1). They suggested a charged-particle emission probability per muon capture of 0.15 ± 0.02. The particle identification (PID) of the emitted ions was not performed in the experiment. Following their experiment, Y. Budyashov et al. measured the energy spectra of the protons and deuterons in the emission energy range above 15 and 18 MeV, respectively [68]. A 50 mg/cm^2-thick Si detector and a 2.2 cm thick CsI(Tl) detector were used as a ΔE-E telescope. The authors investigated the dependence of the emission probability of the charged particle on the atomic number (Figure 4.2).

Based on these experimental data, Hungerford estimated the proton emission spectrum by fitting the experimental data [69] (Figure 4.3). The data[67] were fitted with a function of the form:

$$W(T) = A_1(1 - \frac{T_{th}}{T})^{\alpha} e^{-\frac{T}{T_1}} \quad (T \leq 8 \text{ MeV}) \tag{4.1}$$

$$= A_2 e^{-\frac{T}{T_2}} \quad (8 \text{ MeV} \leq T \leq 20 \text{ MeV}) \tag{4.2}$$

$$= A_3 e^{-\frac{T}{T_3}} \quad (T \geq 20 \text{ MeV}), \tag{4.3}$$

where T is the kinetic energy. and Table 4.1 lists the fitted parameters. It has a low-energy cut-off at 1.4 MeV below the Coulomb barrier at 4.6 MeV.

Table 4.1: Fitting parameters of Eq. (4.1)to (4.3).

Parameter	Eq. (4.1)	Eq. (4.2)	Eq. (4.3)
A_i (MeV^{-1})	0.092405	5.4374^{-3}	5.1785^{-4}
T_i (MeV)	3.1	5.1	10.0
T_{th} (MeV)	1.4	-	-
α	1.3279	-	-

Thus, the experimental energy spectra of the proton and deuteron in the energy range from 15 to 50 MeV were available before the present experiment. The shape of the proton spectrum in the energy range from 1.4 to 50 MeV was estimated by fitting the limited experimental spectra. In this work, the experiment was performed to measure the spectra in the lower energy region from 8 to 35 MeV, where the estimated proton spectrum [69] has a boundary as expressed in Eqs. (4.1) to 4.3. Moreover, we made a comparison between the measured data and the model calculation implemented in PHITS. Finally, the effect of the nuclear reaction model on the muon-induced SEU simulation is discussed.

4.3 Experiment

The experiment was performed using the M1 beam line of the MuSIC [32] at the RCNP [70], Osaka University, Japan. The total beam time was 48 h, including 26 h irradiation to the silicon target and 7 h irradiation without the target to confirm the background noise. This section describes the details of the experimental facility, setup, detectors, and data acquisition system.

4.3.1 MUon Science Innovative muon beam Channel (MuSIC)

The overview of the accelerator facility is described here. Figure 4.4 shows an illustration of the bird's eye view of the RCNP. The RCNP has AVF and ring

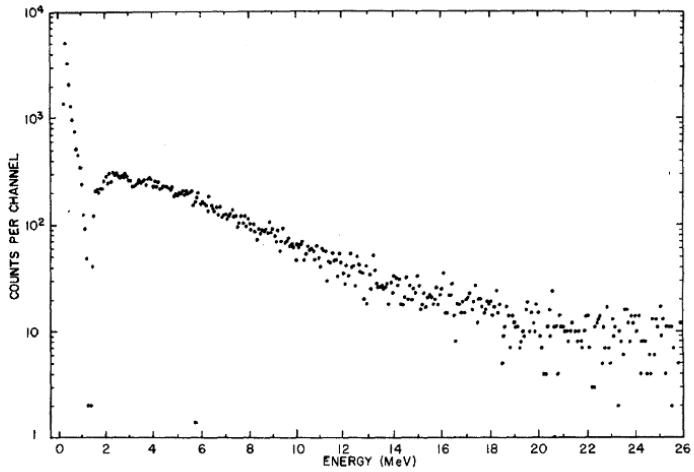

Figure 4.1: Spectrum of energy deposited in 3-mm^t thick Si(Li) detector by ions emitted from the muon nuclear capture reaction. The figure is taken from Figure 3 in [67].

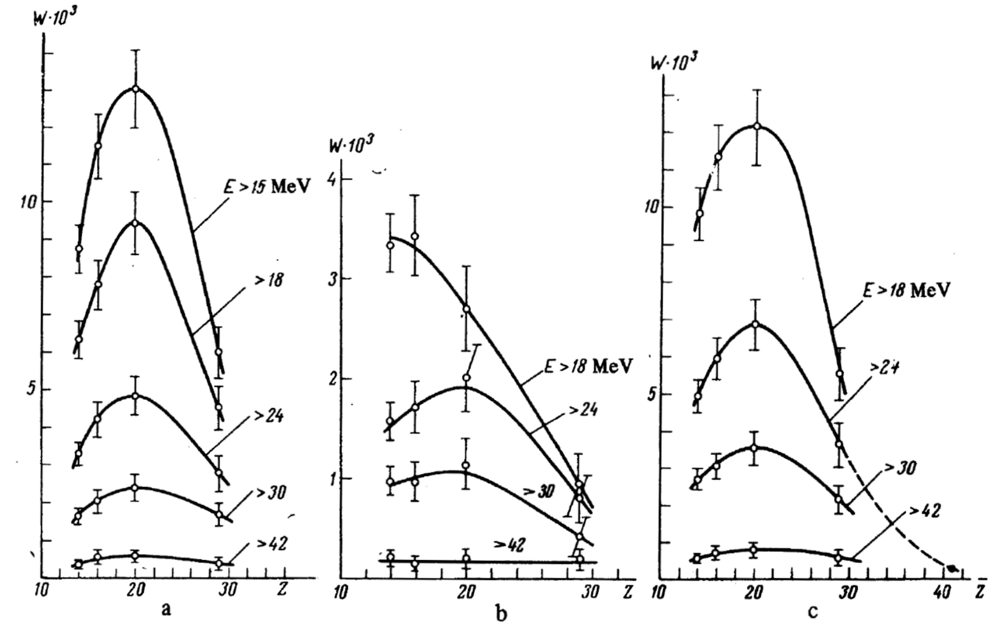

Figure 4.2: Atomic number dependence of emission probability of (a) proton, (b) deuteron and (c) all species of charged particles. W in vertical axis indicates the particle emission per capture. The figure is taken from Figure 7 in [68].

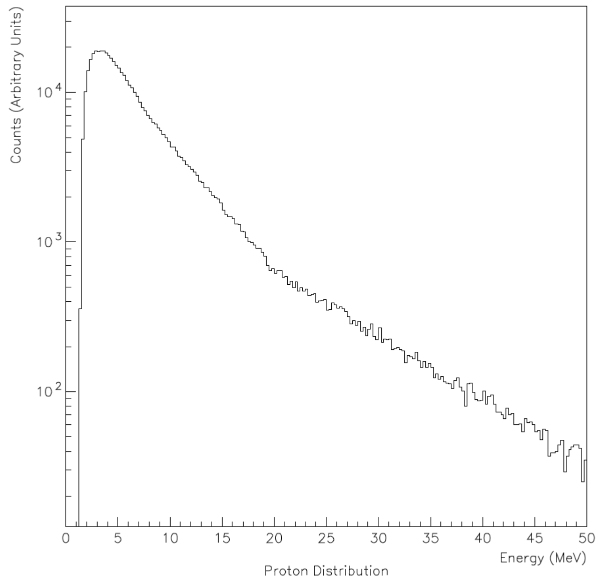

Figure 4.3: A plot of the suggested proton emission spectrum from the nuclear muon capture on silicon. This figure is taken from [69].

cyclotrons to produce a high-energy proton beam. The protons from the ion source is accelerated up to 65 MeV by the AVF cyclotron. The following ring cyclotron accelerates them up to 392 MeV. The proton beam is then finally transported to the West experiment room, where MuSIC is placed through the WSS beam line.

Figure 4.5 shows the beam line of the M1-course at MuSIC. The proton beam was injected to a cylindrical target graphite (4 cm diameter and 20 cm thickness) inside the solenoid coil in the pion capture system to generate pions. The pions were collected by a 3.5 T capture solenoid magnet and transported to the M1 beam line by 36° curved solenoid while they decay into muons following Eqs. (1.1) and (1.2). The polarity and the momentum of the muons were selectable by a solenoid magnet by adjusting the polarity and the current value of the capture solenoid. The momentum distribution of the muon beam at the beam exit was measured as a normal distribution with 7.0% standard deviation. The mean kinetic energy of muons was selected as 6.6 MeV to maximize the number of stopping muons in the target. The spatial distribution of the beam can be approximated as a normal distribution with a standard deviation of approximately 2.2 cm. The 392-MeV ring cyclotron was operated with the average current of 1.1 μA. The average muon intensity at the beam exit was 1800 s^{-1} during the experiment.

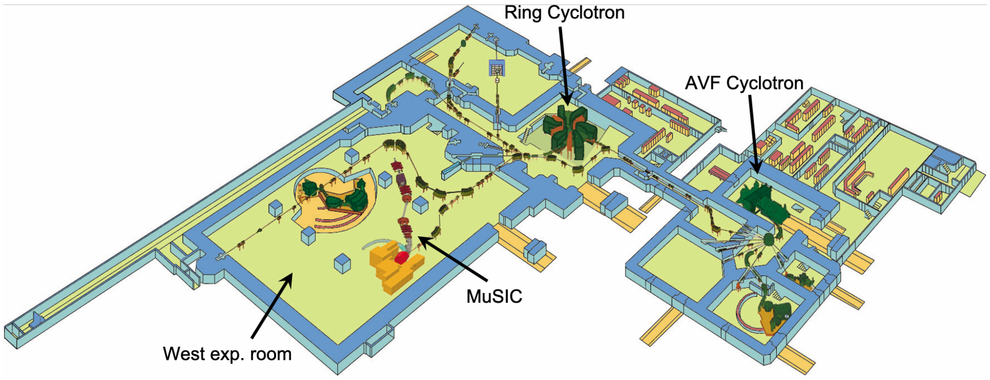

Figure 4.4: Bird's eye view of Research Center for Nuclear Physics (RCNP). The illustration was taken from [70]. Arrows and texts were added.

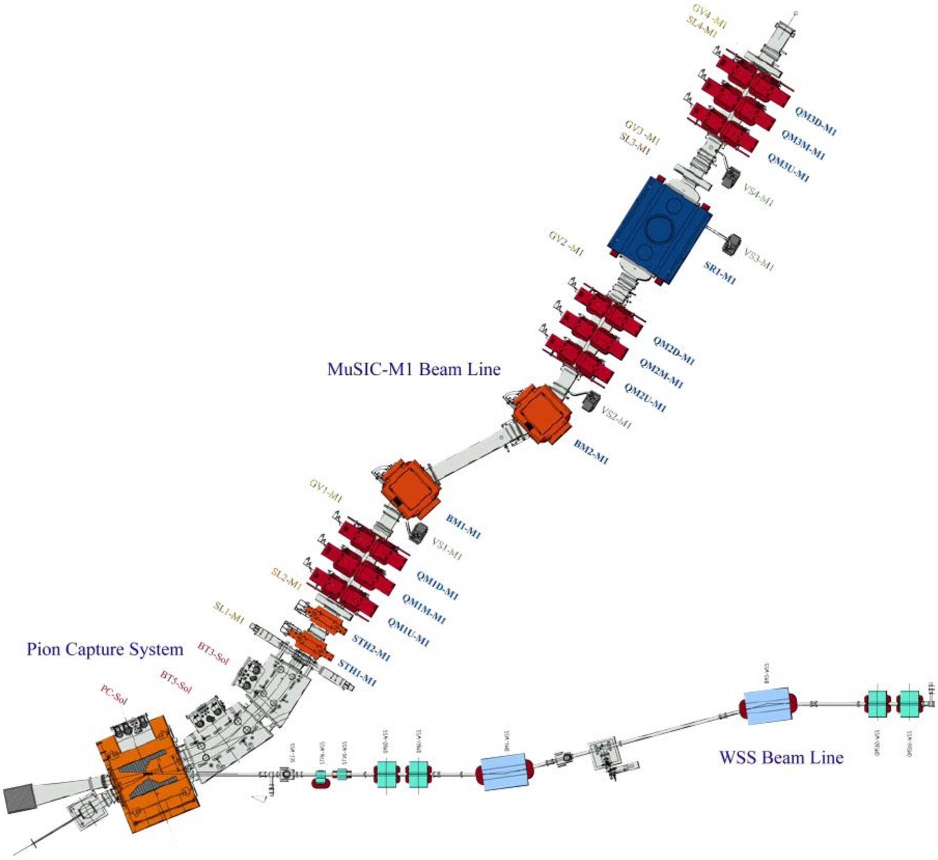

Figure 4.5: M1-course at MuSIC. The figure was taken from [32].

4.3.2 Experimental Setup and Detectors

The generated negative muons were finally transported to a vacuum chamber placed at the beam exit. The chamber was connected to the exit, but a 0.2 mm Kapton foil was used to separate the vacuum spaces inside the beam line and the chamber. The chamber was evacuated by a dry pump during the experiment. A vacuum level in the chamber was under 10 Pa, which was low enough to measure the energy of the ions.

Figure 4.6 shows the experimental setup in the chamber. Two plastic scintillators (Pla. 1 and 2) measuring 50 mm × 70 mm × 0.5 mm^t were used as an incident muon counter. The thickness of the Pla. 1 and 2 was so thin that the muons could pass thorough the incident muon counter. It is necessary to acquire the arrival timings of the muons to make triggers for the data acquisitions because the particle emissions from the nuclear negative muon capture happen in a short time of a few hundred ns after stopping muons, and the beam at MuSIC does not have a time structure. Moreover, the electron contamination in the beam can be excluded by these scintillators, as will be discussed in Section 4.4.

The stopping target was mounted at the center of the chamber. Two silicon detectors denoted as tgt. 1 and 2 in Figure 4.6 were used as active targets. The sensitive area of each detector was 50 mm × 50 mm, and the thickness was 0.1 mm. The energy depositions from emitted charged particles in a target can be reduced by using a thinner target, while an experimental statistics becomes low because the number of stopping muons decreases. The target thickness was chosen to obtain the sufficient statistics in a limited beam time. The energy spectra of the targets were used to cut the background noises, as discussed in Section 4.4. The target was placed at 45° tilt to the beam to reduce the amount of material which the emitted particle would have to pass through before reaching the telescopes.

Two telescopes were mounted in parallel to the target at both upstream and downstream of the target to detect the secondary ions and measure their kinetic energy. The distance between the target and the telescope was 150 mm. A telescope consisted of a 0.325 mm thick-silicon detector and a 25 mm thick-CsI(Tl) detector. The sensitive area of both detectors was 50 mm × 50 mm. The measurement energy range of protons was 8 to 35 MeV in the experiment. The detectors thicknesses determined the energy range. It is because the energy of a stopping particle in ΔE detector and a particle which passed through both ΔE and E detector cannot be properly measured. The thickness of ΔE detector was selected to be 0.325 mm which was so thin that 8 MeV protons could pass though. The thickness of E detector was chosen to be thick enough to fully stop 33 MeV protons.

Another plastic scintillator denoted as veto in Figure 4.6 was placed downstream of the target to reject the events which the muons pass thorough the target. The scintillator measured 150 mm × 150 mm × 15 mm^t.

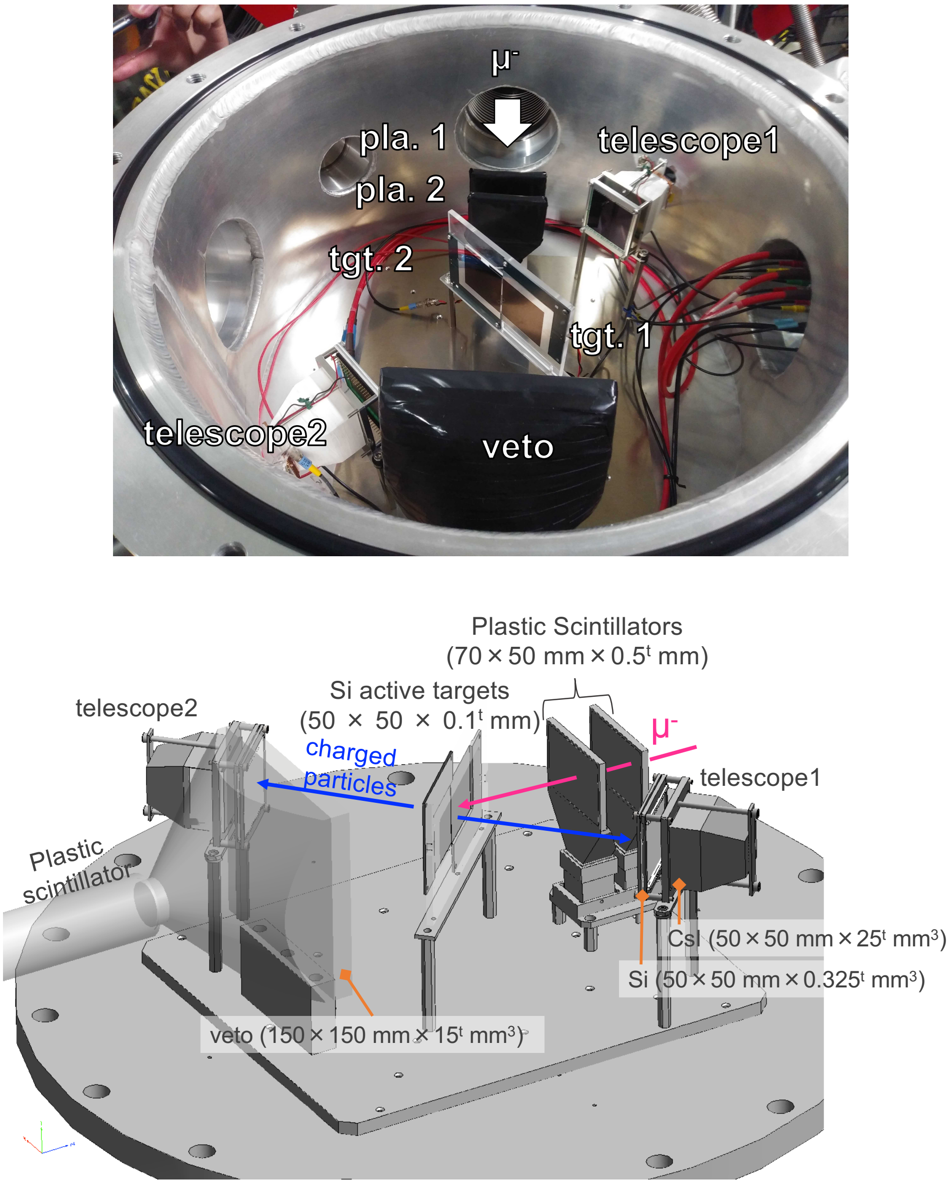

Figure 4.6: Photograph and schematic illustration of the experimental setup at MuSIC

4.3.3 Data Acquisition System

The electronics and data acquisition (DAQ) system for the experiment are described herein. Figures 4.7 and 4.8 illustrate the schema of the electronics for the plastic scintillators and the other detectors, respectively. The electronics were placed at the West experiment room and an underground passage of the RCNP. The shaping amplifiers and the circuits for generating the logic signal from the detector signals were placed in the West experiment room. The output signals from them were sent to the electronics at the underground passage where the analog-digital-converter (ADC) module, TDC module, and trigger circuit were placed. The VME modules of A3400 and V1290N were used as the ADC and TDC modules, respectively. The two modules were controlled by the VLUPO DAQ MASTER module. During the experiment, the coincidence signal of plastics 1 and 2 was input to VLUPO as a trigger signal of DAQ. When the triggers were accepted by the VLUPO module, the ADC and TDC modules took the signals.

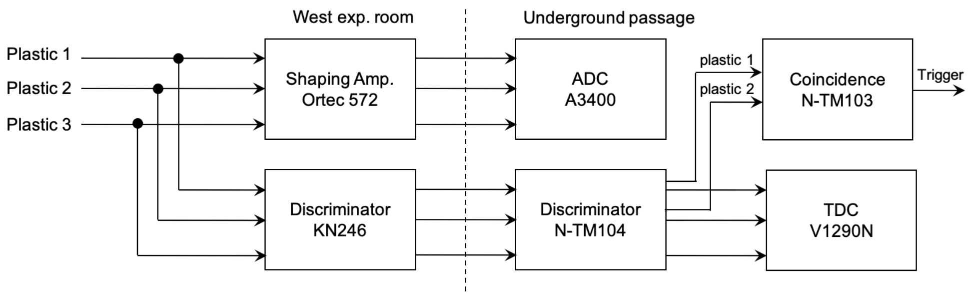

Figure 4.7: Electronics schema of the plastic scintillators

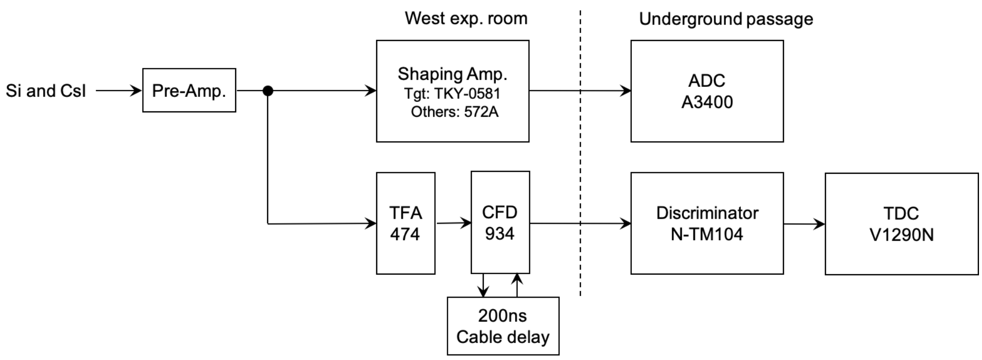

Figure 4.8: Electronics schema of the Si and CsI(Tl) detectors. TFA and CFD represent Timing Filter Amplifier and Constant Fraction Discriminator, respectively.

4.4 Data Analysis

The data analysis method is described. The ΔE-E method was applied using the two telescopes to obtain the energy spectra of the charged particle. The events of the telescopes were contaminated by the direct hit of the muons and the emission ions from the nuclear muon capture reaction on nuclei other than silicon. Therefore, some gates were set to cut background by using the outputs from the plastic scintillators and the target silicon detectors.

This section describes the energy calibration for the silicon detectors. The gate settings are then described. Finally, the result of background reduction is shown.

4.4.1 Energy Calibration

The energy calibration method for the detector is described herein. The ADC data of the plastic scintillators were only used to exclude the electron events contaminating the muon beam. The energy calibration for the plastic scintillators and the CsI(Tl) detectors was not necessary and not performed. The response of the CsI crystal is sensitive to the particle type. Therefore, it was difficult to calibrate the detectors. Thus, the CsI(Tl) detectors were used for identification purposes only, as will be described in Subsection 4.4.5.

The energy calibration for the silicon detectors was performed with a three alpha sources (i.e., ^{148}Gd, ^{241}Am, and ^{244}Cm). These nuclei are unstable and will decay with alpha particle emission with a specific energy presented (Table 4.2). The listed energy peaks were used to produce fit of the spectra and find the relation between the ADC output and the deposit energy. The relation between the ADC channel and the energy is linear. The calibration points obtained by the spectra are fit with a linear function.

$$E = m * ADC + c \tag{4.4}$$

where, m is the gradient, and c is the offset. Figure 4.9 shows the energy calibration result of 0.325-mm-thick silicon detector consisted in telescope 2. The linear fitting result is shown in (a). The fitted peaks of the alpha particle from each nucleus are shown from (b) to (d). For the Gd peak, a single normal distribution was used to fit because a mono-energetic alpha-ray can be obtained from the Gd. In contrast, the fitting with two normal distributions and the relative intensities were applied for (c) Am and (d) Cm considering the satellite peaks. The energy resolutions of the detector were then estimated. The energy calibration for the other silicon detectors was done with the procedure described earlier. Tables 4.3 and 4.4 summarize the calibration parameters and the energy resolutions for the silicon detectors.

Table 4.2: Three radioisotopes used as the alpha sources.

Nucleus	Half-life (y)	Energy (keV)	Relative intensity
^{148}Gd	74.6(30)	3182.690(24)	100
^{241}Am	432.6(6)	5442.80(13)	13.1(3)
		5485.56(12)	84.8(5)
^{244}Cm	18.10(3)	5762.64(3)	23.10(10)
		5804.77(5)	76.90(10)

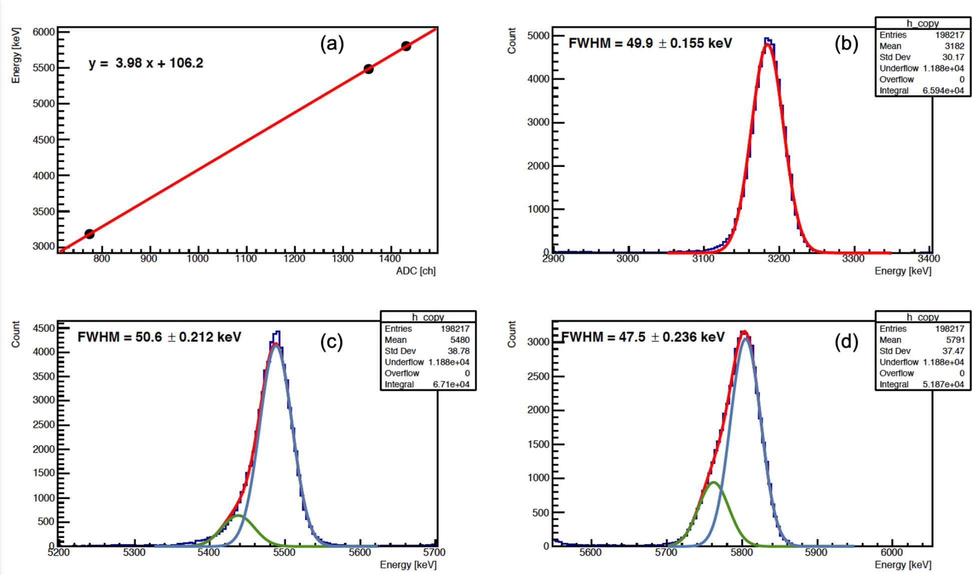

Figure 4.9: Fitting and energy calibration result of silicon detector. The results of 0.325 mm-thick silicon detector of telescope 2 is shown here as an example. (a) shows relationship of energies and ADC outputs. (b), (c), and (d) are the fitted results of Gd, Am, and Cm peaks, respectively.

Table 4.3: Calibration parameters for the silicon detectors.

Detector	Offset	Gradient
ΔE1	106.2	3.98
ΔE2	97.2	3.99
tgt1	45.5	0.92
tgt2	150.0	0.91

Table 4.4: Energy resolutions (FWHM) of the silicon detectors.

Detector	Energy resolution (keV)
ΔE1	106.7
ΔE2	49.3
tgt1	129.0
tgt2	135.1

4.4.2 Plastic Scintillators

Incident Muon Counter

Two plastic scintillators were placed upstream of the target to detect the incident muons. However, the muon beam was contaminated by electrons. We analyzed the signals of plastics 1 and 2 to exclude the electrons. Figure 4.10 shows the ADC spectra of each plastic scintillator. We assumed that the peaks around the 1200 ch for plastic 1 and 2000 ch for plastic 2 were muons. The events at the low-channel region included electrons and other noises. The ADC channels, where the spectra became the minimum (705 ch and 802 ch for plastics 1 and 2, respectively), were chosen as thresholds. The events above the thresholds were regarded as muons. Figure 4.11 shows the correlation plot of plastics 1 and 2. We define a hyperbolic curve passing through a point (802, 705) given by

$$Pla1 \geq \frac{705 * 802}{Pla2} \tag{4.5}$$

as a gate (hereafter referred as the 'muon gate') drawn in Figure 4.11 as a red line. Thus, 9.35×10^7 muons were detected during the physics runs.

Veto Detector

Another plastic scintillator was placed downstream of the target for veto counting. Figure 4.12 shows an ADC spectrum of the veto detector obtained during the physics runs. The blue and red lines represent events without any gate and with the muon gate, respectively. Two peaks existed around 750 and 1300 ch in the blue line. The muons and the electrons in the beam had the same velocity, and the electrons had a higher energy compared to the muons. Therefore, the electrons had a higher peak in the spectrum, which can be eliminated by the muon gate. The events in the channel lower than muon peak (i.e., pedestal peak) implied that the muons stopped in the target. Another gate hereafter referred to as the 'veto gate' to separate the muon and pedestal peak given by

$$Pla3 \leq 215. \tag{4.6}$$

The valley between the muon and pedestal had minimum in the 215 ch. The channel was applied to separate these peaks.

Note that steep increase in Figure 4.12 around 3200 ch does not indicate other particle bombardments, but a saturation of the shaping amplifiers. Similar increases were observed in the spectra of plastics 1 and 2 (Figure 4.11). These increases occurred at a sufficiently higher channel compared to the muon and the electron; therefore, they did not affect the analysis.

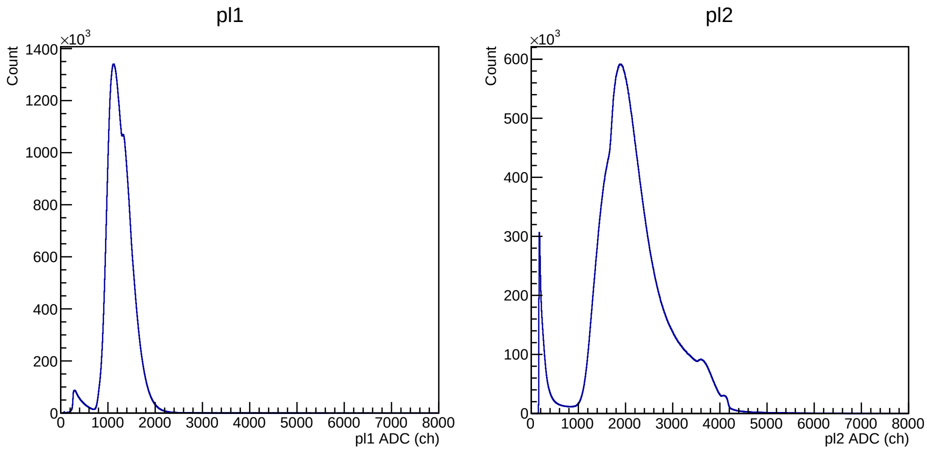

Figure 4.10: ADC spectra of plastics 1 (left) and 2(right)

4.4.3 Target Silicon Detector

Figure 4.13 shows the deposition energy spectra of the two target 0.1 mm-thick silicon detectors with the muon gate. A red line shows the spectrum with only the muon gate. The coincidence and anti-coincidence gates with the veto detector were applied to the spectrum drawn as green and black lines, respectively, to investigate the events with stopping muons. The coincidence events had a peak around 0.5 MeV, which corresponded to the energy deposited by the stopping power of the muons passing through the target. On the contrary, the anti-coincidence events had a higher-energy deposition compared to the coincidence event due to the emitted charged particles (light ions and recoiling nuclei) from the nuclear muon capture reaction. Thus, another gate (hereafter referred to as the 'target gate') was set as

$$tgt1 \geq 0.37 \text{ or } tgt2 \geq 0.29 \tag{4.7}$$

to exclude the pedestal peak in the case of anti-coincidence events.

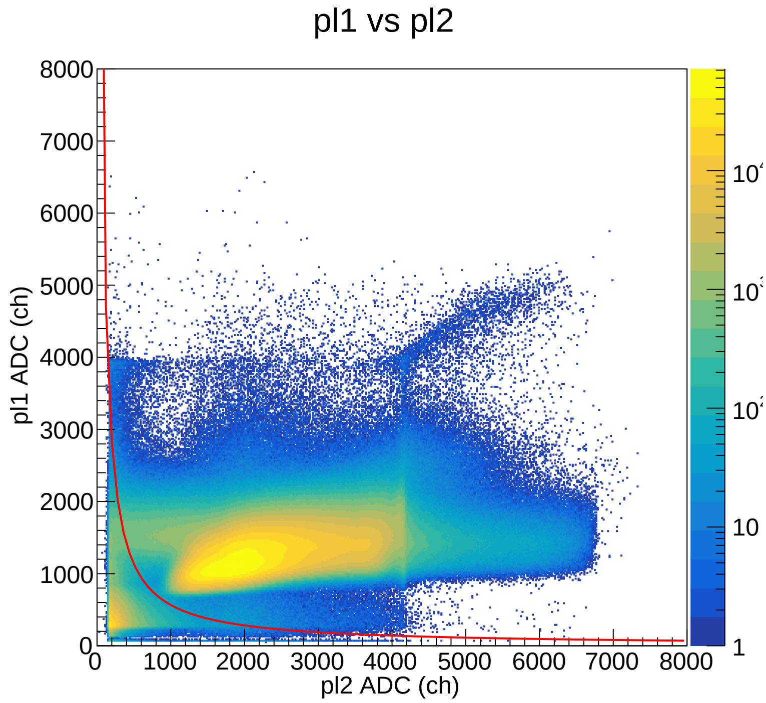

Figure 4.11: Correlation plot of ADC outputs from plastics 1 and 2.

4.4.4 Background Reduction

Figure 4.15 shows the ΔE-E plot of the telescopes. The bands made of protons, deuterons, and tritons were observed in the plot of the telescope 1. The plot of telescope 2 included a significant amount of noises, while a part of proton and deuteron bands appeared. The noises seemed to be mainly caused by the muons, which directly hit the telescope 2 because the telescope was placed downstream of the target. Figure 4.15 shows the distributions of the time from the timing of the signal of plastic scintillator 1 to the events in the ΔE detectors. The muons, which directly hit the telescope 2 appeared as a spike around 500 ns. The distributions were roughly fitted by an exponential function. When muons stop in silicon, they will decay or be absorbed by the nuclei with a lifetime of 758 ns. However, the decay time of the distributions was over 1800 ns, which was considerably longer than the lifetime on silicon. The lifetimes of muons on carbon and oxygen are 2028 and 1844 ns, respectively. The plastic scintillators and the target holder made of acrylic contained these nuclei. Hence, the raw data seemed contaminated by the events from the muons stopped in the plastic scintillators and/or the target holder.

The gates were set to exclude contamination and other noises from the ΔE-E plot. First, the muon gate described in Subsection 4.4.2 was applied to ensure

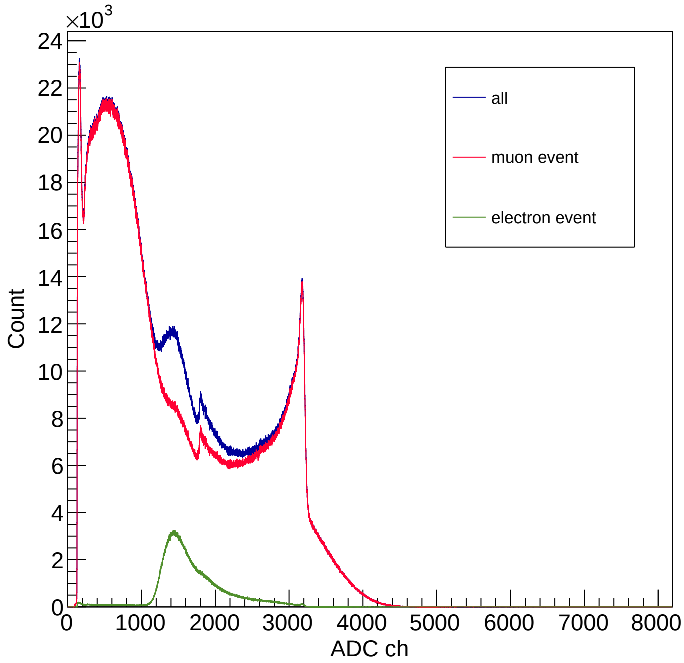

Figure 4.12: ADC spectrum of the plastic scintillator for veto counting.

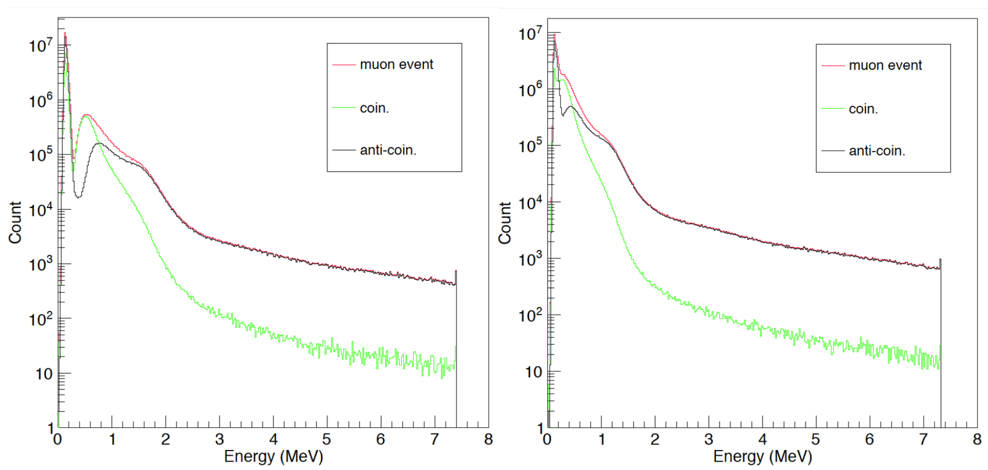

Figure 4.13: Energy spectrum of target silicon detectors 1(left) and 2(right).

the events caused by the muons. Next, the target and veto gates, as described in Subsections 4.4.3 and 4.4.2, were adopted to identify that the incident muons hits the target silicon detector and stopped in it. Finally, the events with the timing under 500 ns were removed events, indicating that the muons directly hit the telescope 2.

Figure 4.16 shows the ΔE-E plots with the gates described above. The muon-hit events observed in the low-deposition energy region (under 3 MeV) of telescope 2 were fairly removed. Figure 4.17 depicts the time distributions of the ΔE silicon detectors. The distributions were fitted again with an exponential function. The decay times for ΔE 1 and 2 are 777.5 ± 30 and 758.4 ± 25 ns, respectively, which were consistent with those of the muons on silicon within the fitting error. Therefore, we decided to identify the particles by using the ΔE-E plots shown in Figure 4.16.

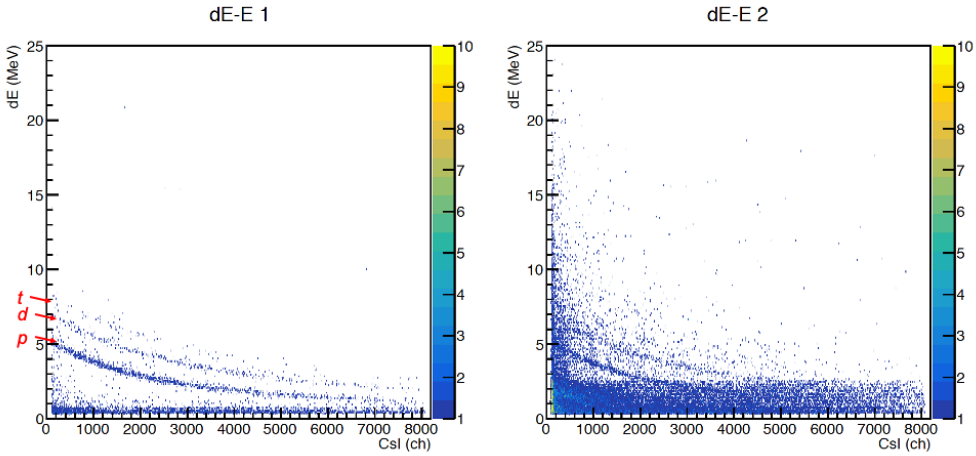

Figure 4.14: Raw ΔE-E plot of telescope 1 (left) and 2 (right).

4.4.5 Particle Identification

The particle identification of the emitted H ions was performed using the ΔE-E technique. The technique requires a transmission-type ΔE detector (0.325 mm-thick Si detector in this work) and a thick E detector (25 mm-thick CsI(Tl) detector in this work). The stopping power dE/dx can be calculated with the well-known Bethe-Bloch equation given as follows:

$$-\frac{dE}{dx} = \frac{4\pi n}{m_e}(\frac{e^2}{4\pi\epsilon_0})^2\frac{Z^2}{v^2}\ln(\frac{2m_e}{I}v^2) \tag{4.8}$$

where,

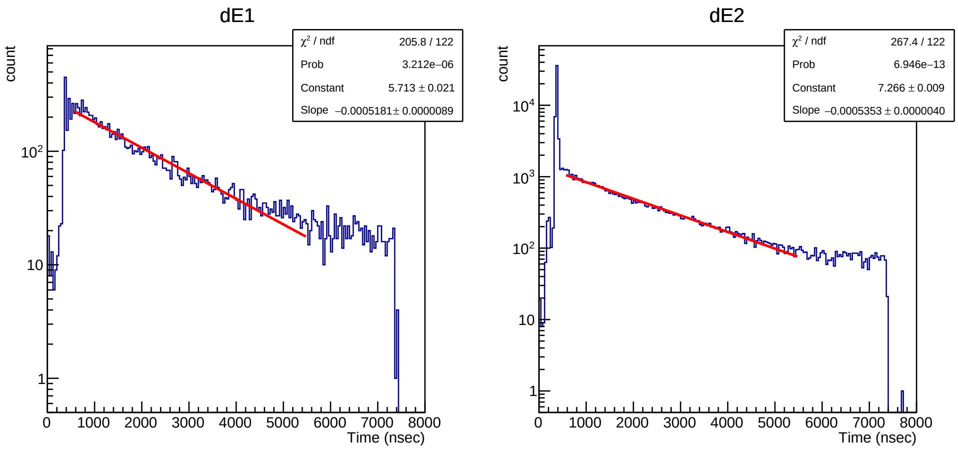

Figure 4.15: Raw time distribution of events of ΔE1 (left) and 2 (right) from the timing of the plastic scintillator 1.

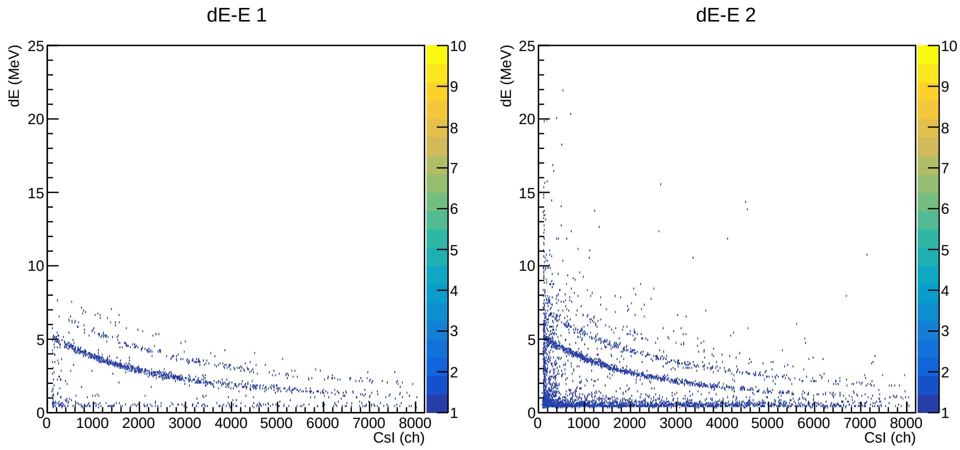

Figure 4.16: ΔE-E plot of telescope 1 (left) and 2 (right) with the gate to exclude background.

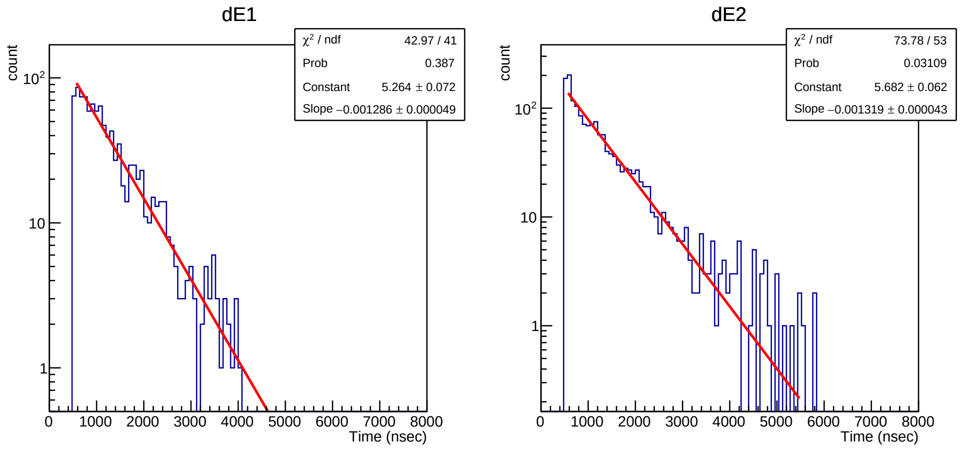

Figure 4.17: Time distribution of events of ΔE1(left) and 2(right) from the timing of the plastic scintillator 1 with the gate to exclude background.

n = electron density
m_e = electron mass
e = elementary charge ($1.602\ \times 10^{-19}$)
ϵ_0 = permittivity of vacuum
Z = particle atomic number
v = particle velocity
I = mean excitation potential of the material
Here, v^2 is replaced by $\frac{2E}{A}$ where E is kinetic energy, and A is the particle mass. We obtain the following:

$$-\frac{dE}{dx} = \frac{2\pi n}{m_e}(\frac{e^2}{4\pi\epsilon_0})^2 AZ^2\frac{1}{E}\ln(\frac{4m_e}{AI}E). \tag{4.9}$$

We obtain the following relation by ignoring the logarithms:

$$-\frac{dE}{dx} \times E \propto AZ^2. \tag{4.10}$$

The particle can be identified because the value of $\frac{dE}{dx} \times E$ is unique for the spices of particles. Consequently, we obtained the bands of charged particles (Figure 4.16) using this principle.

The bands of protons, deuterons, and tritons were cut from Figure 4.16 to obtain the energy spectra. Each band was fitted by a polynomial function to obtain the center of the band (Figure 4.18). The events within 5σ of the energy resolution of the 0.325 mm-thick silicon detector were regarded as the particle under the consideration. As a result, the events were selected, and the count of each particle is shown in Table 4.5. The ADC output from the CsI(Tl) detectors was not calibrated to energy. The total energy of each particle was then decided from the deposition energy in the ΔE detectors. The relationship between ΔE and the total energy was calculated by PHITS [9] (Figure 4.19). The cut spectrum was calculated in the energy spectrum using this relationship.

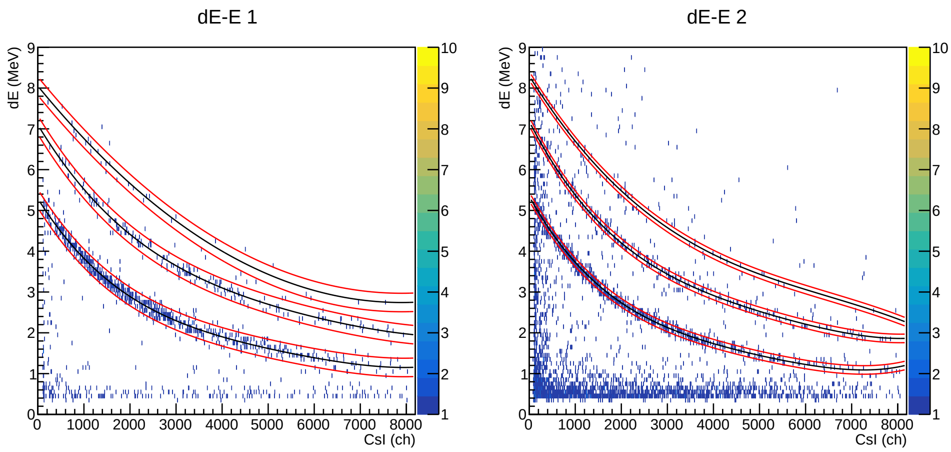

Figure 4.18: Event selection from ΔE-E plot. The left and right plots shows telescope 1 and 2, respectively. The black lines are the fitted polynomial function. The red lines indicate the limits of the PID.

Table 4.5: Total counts and counting rates of proton, deuteron and tririon observed during the physics run with the muon, target, and veto gates.

Particle	Count	Counting rate ($/10^7$ muon)
proton	1290	138.0±3.8
deuteron	389	41.6±2.1
triton	62	6.6±0.8

4.4.6 Empty Run

The muon irradiation without the silicon target was performed to investigate the amount of detected charged particles from other than the target. Figure 4.20 shows the ΔE-E plots with the muon and veto gates measured during the empty run. The events of the charged particles were observed, although the target was removed. The proton, deuteron, and triton events were obtained from the ΔE-E

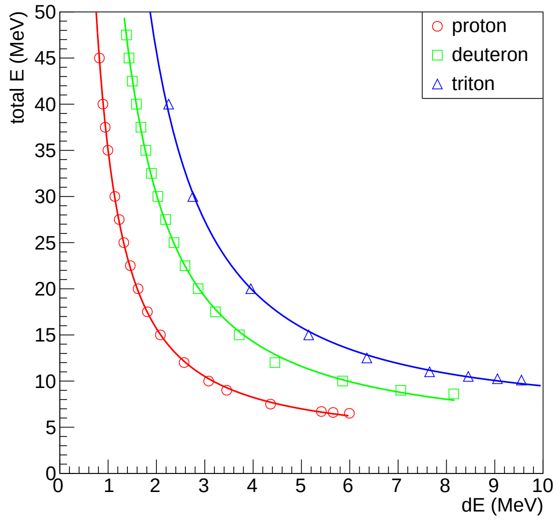

Figure 4.19: Relationship between total energy and deposition energy in 0.325 mm-thick silicon calculated by PHITS [9]. Each symbol represents calculation point and the lines show fitting curves.

plot with the same procedure as described in Subsection 4.4.5. Table 4.6 presents the count rates of the particles. The rates were 16% or more of those during the physics run shown in Table 4.5. These events seemed to be the charged particles from the capture reaction in the target holder; hence, we expected that the events could be reduced by the target gate. To examine this expectation, the count rates in the case of the physics run with only the muon and veto gates were derived and shown in Table 4.7. In this case, the counts included the events from the target holder. The sums of the count rates in the empty and physics run with all gates (count rates shown in Tables 4.6 and 4.5) were consistent with those of the physics run with the muon and veto gates. This comparison indicated that the target gate worked properly to reduce the events observed during the empty run. Consequently, we conclude that the background noise was reasonably reduced by applying the gate described in Subsection 4.4.4.

4.5 Results and Discussion

First, the energy spectra of the protons, deuterons, and triton emitted from the muon nuclear capture reactions on silicon are shown and compared. The present proton and deuteron data were then compared with the past data obtained in [68] to check the consistency between this and past works. Finally, the experimental

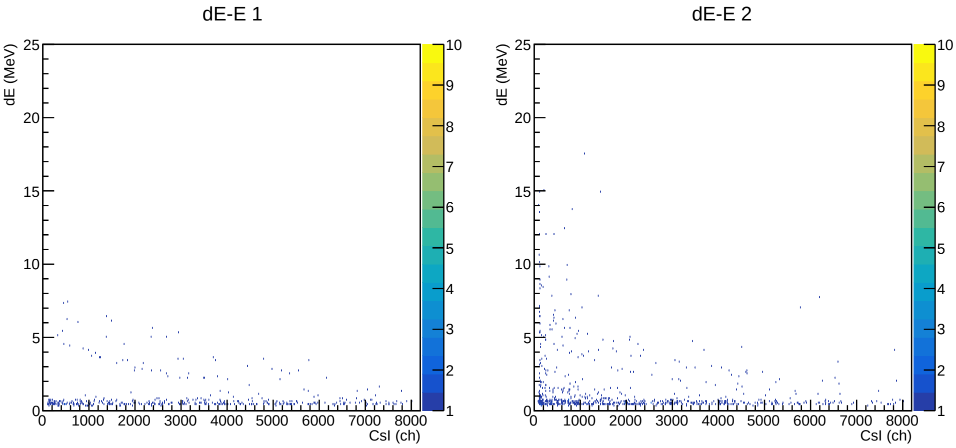

Figure 4.20: ΔE-E plot of telescope 1 (left) and 2 (right) obtained during the 7-hour empty run.

Table 4.6: Total counts and counting rates of proton, deuteron and triton observed during the empty run.

Particle	Count	Counting rate (/10^7 muon)
proton	43	21.9±3.3
deuteron	23	11.7±2.4
triton	7	3.5±1.3

Table 4.7: Total counts and counting rates of proton, deuteron and triton observed during the physics run with the muon and veto gates.

Particle	Count	Counting rate (/10^7 muon)
proton	1524	163.0±4.2
deuteron	475	50.8±2.3
triton	87	9.3±1.0

data were compared to the model calculation implemented in the PHITS code. Moreover, the impact of the nuclear reaction models on the muon-induced SEU simulation was investigated by using the PHITS-SV model.

4.5.1 Experimental Data

Figure 4.21 shows the energy spectra of the proton, deuteron, and triton in the energy range from 8 to 33 MeV. The spectra in the lower-energy region were successfully obtained compared to the past data [68]. The upper limits of the spectra were set to as 33 MeV for comparison with the past data. The error bars included only the statistical uncertainty. First, a comparison between the present and past data was made in Figure 4.22. The data of telescopes 1 and 2 were summed to make a comparison. The present experimental data were normalized to the past proton data [68] at 17 MeV. The measured spectra can be smoothly connected to the higher-energy region. Moreover, the emission ratio of the proton and the deuteron generally agreed with the past data. Consequently, the comparison demonstrated the consistency between the present and past data.

Next, the proton spectrum was fitted by the two exponential functions given in Eqs. (4.2) and (4.3) to compare with the estimated spectrum [69]. The measured spectra in the energy range from 8 to 29 MeV were used for the fitting. Above 29 MeV, the data are taken from the past data. The data were normalized at 17 MeV in a same manner of the above comparison. Figure 4.23 depicts the fitted spectrum. The solid line shows the summation of two exponential curves, and the dashed lines show each curve of Eqs. (4.2) and (4.3). The decay constants of T_2 and T_3 were derived as 4.5 ± 0.7 and 15 ± 5.5 MeV, respectively, and consistent with the values in Table 4.1 within the fitting errors. Furthermore, the two exponential functions intersected around 20 MeV, where the suggested spectrum was divided into two functions. The estimated energy dependence in [69] of the proton emission agreed with the experimental data.

4.5.2 Comparison with Model Calculation

As mentioned in Subsection 3.2.1, the muon nuclear reaction is described with QMD [11] for the dynamic process and GEM [12] for the statistical decay process. We performed benchmark tests of the reaction model implemented in PHITS. For the neutron-induced nuclear reactions, some studies made comparisons between the experimentally charged-particle emission and the simulation with the QMD plus GEM. Moreover, the QMD was improved by using the surface coalescence model (SCM) to reproduce the experimental result. Appendix A.1 describes the SCM. Watanabe et al. reported that the SCM implementation to the QMD (hereafter referred to as modified-QMD, MQMD) led to the enhancement of the produc-

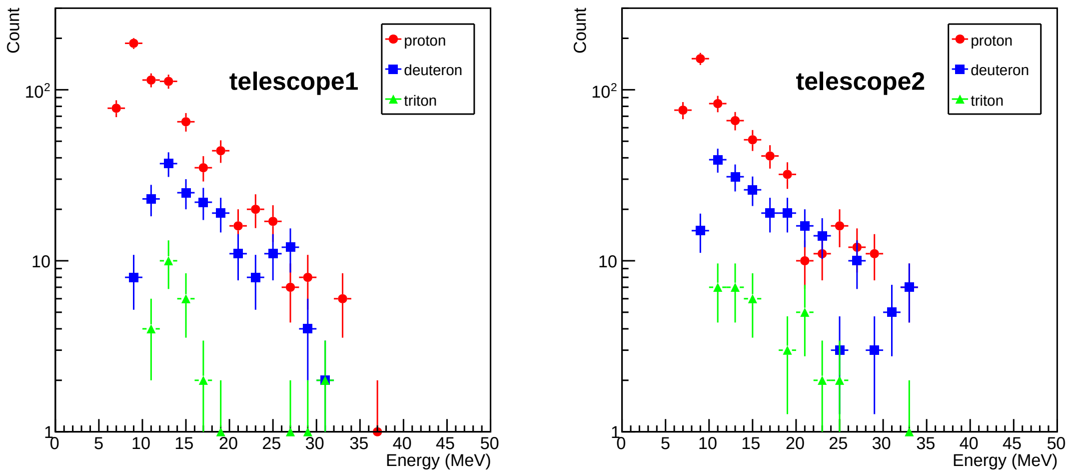

Figure 4.21: Measured energy spectra of proton, deuteron, and triton emitted from the muon nuclear capture reaction on silicon. The results of telescope 1 and 2 are shown in left and right panels, respectively.

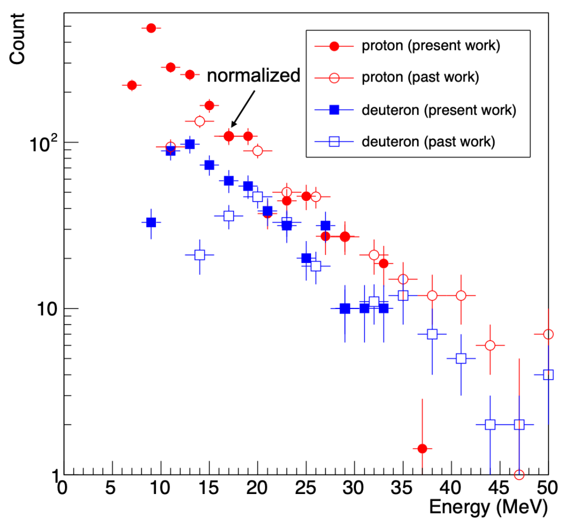

Figure 4.22: Comparison of the measured spectra of proton and deuteron and the past data taken from [68].

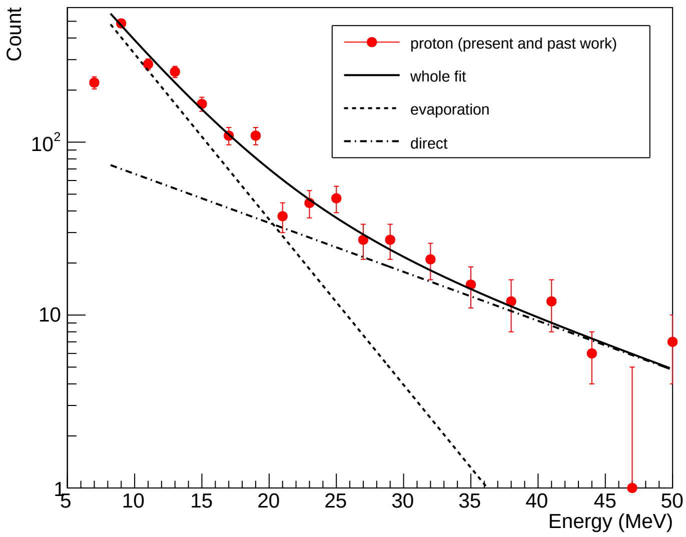

Figure 4.23: Proton spectra fitted by the two exponential curves. The measured data plotted from 8 to 29 MeV. Above 29 MeV, the data were taken from [68]. The data are normalized at 17 MeV.

tion of light complex particles (i.e., deuteron, triton, alpha particle, and ^{3}He) [52]. They found that the agreement with the experimental data was fairly improved due to the SCM. S. Abe et al. applied the MQMD to analyze the neutron-induced SEU simulation of a 25 nm NMOSFET and made a comparison with other nuclear reaction models implemented in PHITS [53]. They recommended the use of the MQMD plus GEM for the simulation of soft error induced by neutrons with the energy above 20 MeV.

Some works pointed out the advantage of the MQMD for the simulation of the neutron-induced reaction. The basic process of the muon capture reaction is similar to the neutron one in that the energetic neutron is generated following the Eq. (1.5). Hence, we expected that the MQMD improved the accuracy of the muon-induced reaction. We performed benchmark tests for the GEM with the default QMD and MQMD.

The simulation was performed with a total of 5×10^6 events for ^{nat}Si. To make a comparison, the muons were made to stop uniformly in the 0.1-mm thick silicon to reproduce the experimental condition. The emitted particles (i.e., proton, deuteron, and triton) from the silicon target were then counted. The emission probability per nuclear capture reaction was derived by dividing the number of the counted particle by the capture rate to the nucleus (= 0.66 in PHITS simulation) and the width of energy bin. Figure 4.24 plots the simulation results are plotted with the experimental data. The result clearly showed that the MQMD enhanced the deuterons and tritons production. The production ratios of the deuteron and the triton to proton were also improved (Table. 4.8). However, the MQMD simulations still underpredicted the emission of all particles, especially in the relatively higher-energy region.

The calculation of the neutron-induced nuclear reaction showed that the proton energy spectrum was reproduced well by using the QMD/GEM and MQMD/GEM [52, 53] because the reaction process of proton emission is relatively simple. In contrast, the spectrum of the proton from the muon capture reaction was underestimated, especially in the high-energy region. This underestimation was partly caused by the low excitation energy of the nuclei, which a neutron gains at the first step of the calculation of the muon capture reaction. Some papers [71–73] indicated that the high-energy proton and neutron emissions from the muon reaction were reproduced well by assuming the high nuclear excitation function caused by the other physical processes (i.e., captures on pairs of nucleons [71], three-body muon decay [72], and partially conserved axial vector current hypothesis [73]) not considered in the present PHIS simulation. Therefore, it is desirable to consider these processes in the PHITS for further improvement of the simulation of the muon reaction.

Table 4.8: Production ratio of deuteron and triton to proton in the energy range above 10 MeV.

	p/d	p/t
Exp.	2.11 ± 0.1	13.7 ± 1.8
MQMD	3.25	23.8
original QMD	46.5	422

4.5.3 Comparison with Neutron-induced Nuclear Reaction

In this subsection, we make a comparison between the particle emissions from the nuclear muon capture reaction on ^{nat}Si (^{28}Si is the most abundant isotope, at 92.23%) and the neutron-induced reaction on ^{27}Al to investigate the fundamental physical process of the muon reaction. As mentioned earlier, the nuclear muon capture reaction occurs when a muon bound by an atom reacts with a proton in a nucleus via a weak interaction following Eq. (3.2). The generated neutron gains the kinetic energy from the mass of the muon; thus, the excited nucleus is formed, and particles are emitted. The reaction is fundamentally caused by the energetic neutron. Therefore, we assumed that the nuclear muon capture reaction on ^{28}Si is

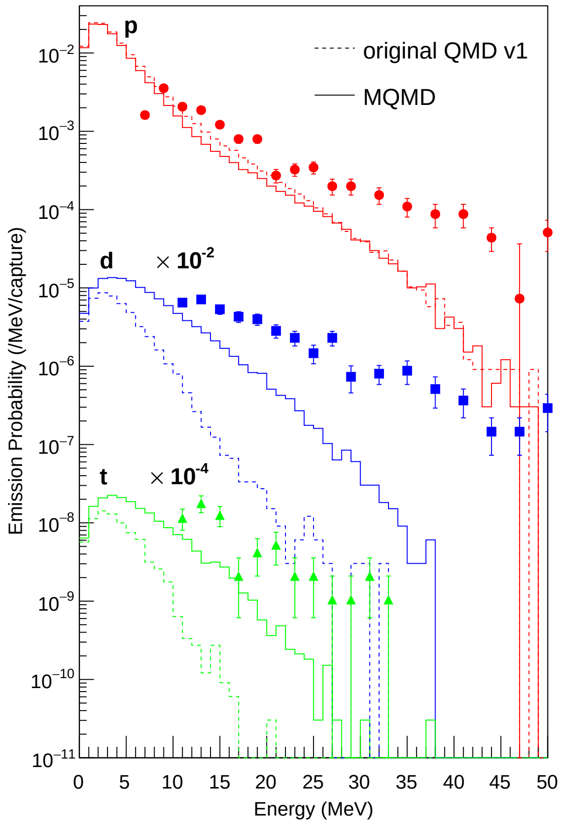

Figure 4.24: Energy spectra of proton, deuteron and triton from the muon nuclear capture reaction in ^{nat}Si. The horizontal and vertical axes indicate the energy of the emitted particle and the emission probability per the nuclear capture reaction, respectively.

roughly equivalent to the energetic neutron injection on one atomic number-less nucleus, ^{27}Al.

The existing data [74] with the incident neutron energy range from 28.5 to 62.7 MeV were chosen. The particle emission from the muon reaction was considered isotropic since the muon is captured by a nucleus after losing its kinetic energy. Therefore, the energy-differential cross-sections of the proton, deuteron, and triton were selected for comparison and plotted in Figure 4.25. The cross-sections were measured in the energy range above 6 MeV for proton and deuteron and 12 MeV for triton. In this comparison, we focused on the ratio of the emission energy integral of the cross-sections of the proton, deuteron, and triton because the absolute values cannot be directly compared to the muon data.

The production ratio of protons and deuterons is plotted as a function of the incident neutron energy in Figure 4.26. The solid circles correspond to the whole emission energy. The spectrum of the deutron emitted from the muon reaction is available above 10 MeV. Then, the ratio above 10 MeV is also plotted. The ratio in the muon case is 2.11±0.1 as shown in Table 4.8. The production ratio of proton to deuteron above 10 MeV agrees with that from the muon capture reaction except for the incident neutron energy 62.7 MeV. Thus, the result indicates that the fundamental physical process of the deuteron emission from the muon reaction is similar to that from the neutron reaction.

In contrast, the ratio of proton to triton (i.e., 13.7 ± 1.8) from the neutron reaction shows disagreement with that from the muon reaction (Table 4.8). The ratio was larger than 47 in the case of the neutron reaction, indicating possibility of an enhancement on the triton emission from the muon reaction on silicon by the specific phenomenon. For example, the muon is captured by the alpha cluster in the ground state of ^{28}Si; the triton is emitted by the following reaction process:

$$\mu^- +^4 \mathrm{He} \rightarrow t + n + \nu_\mu. \tag{4.11}$$

However, only the triton data with low statistics are available in the current situation. It is desirable to acquire higher statistical data for a further detailed discussion.

4.5.4 Impact of Nuclear Reaction Model on Muon-induced SEU Simulation

As mentioned in Subsection 4.5.2, the simulation with the MQMD plus GEM enhanced the emission of d and t from the nuclear muon capture reaction on $^{\mathrm{nat}}$Si, although a large discrepancy still exists between the simulation and experimental results. An SEU simulation with MQMD/GEM was newly performed to investigate the impact of the nuclear reaction models on the negative muon-induced

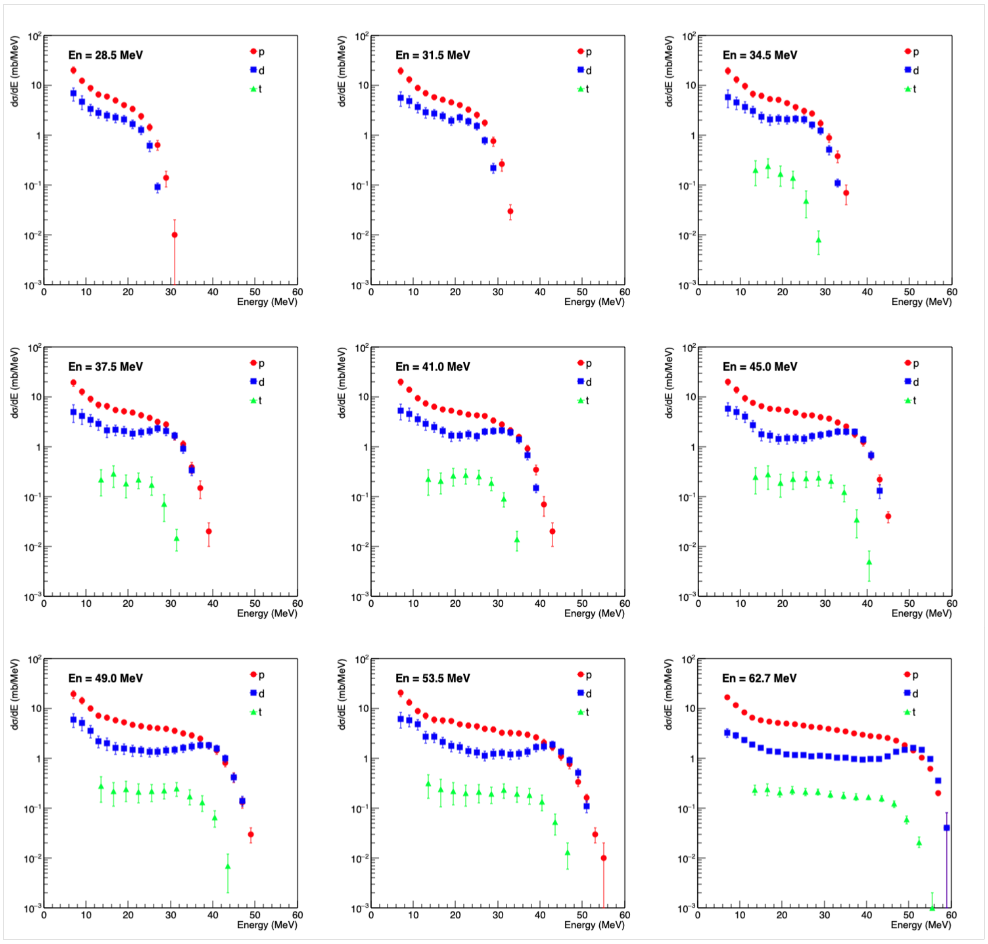

Figure 4.25: Energy-differential cross sections of proton, deuteron and triton from the n + ^{27}Al reaction with the incident energy from 28.5 to 62.7 MeV. The data are taken from [74].

SEU simulation. The simulation was conducted with the same manner as that in Chapter 3, except for the nuclear reaction model selection.

Figure 4.28 shows the comparisons of the mean SEU cross-sections induced by p, d, t and α emitted from the nuclear muon capture for the 65-nm SOTB SRAM. The cross-sections are plotted as a function of the critical charge Q_c. No large differences existed in the p- and α-induced cross-sections between the QMD and the MQMD. On the contrary, the d- and t-induced cross-section were increased by applying the MQMD. At the critical charge of 0.08 fC, the d- and t-induced cross-sections of the MQMD were 2.3 and 1.3 times larger than those of QMD, respectively. As shown in Fig. 4.24, the emissions of d and t, especially in the high energy region, are enhanced due to the SCM implementation to the QMD. Thus,

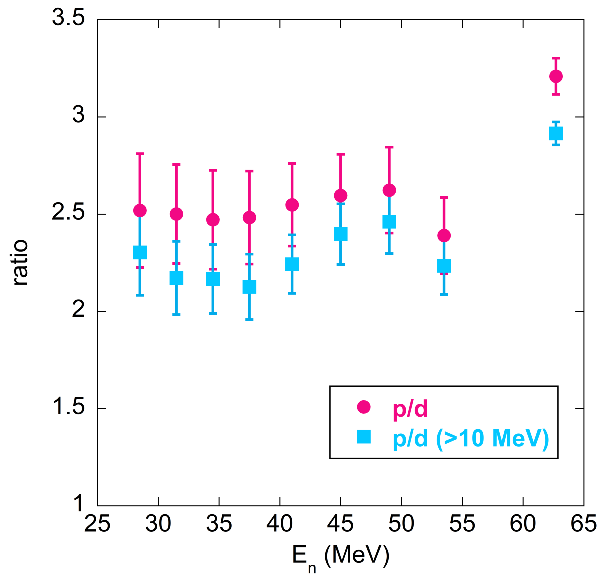

Figure 4.26: Production ratio of proton to deuteron as a function of the incident neutron energy from the n + ^{27}Al reaction. The data is taken from [74].

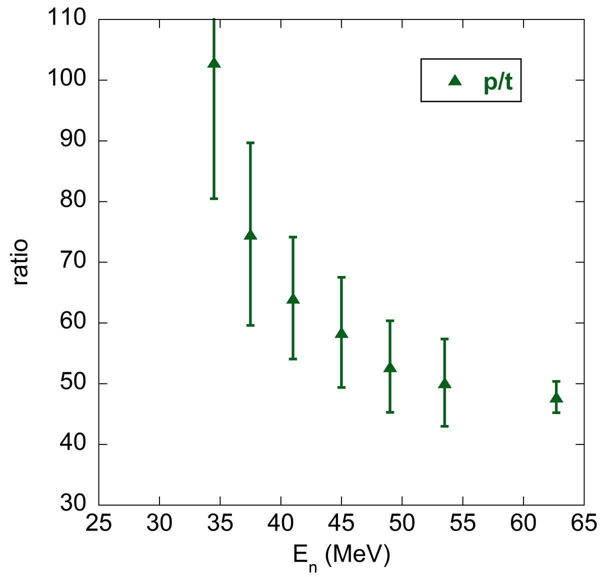

Figure 4.27: Production ratio of proton to triton as a function of the incident neutron energy from the n + ^{27}Al reaction. The data is taken from [74].

d and t have longer ranges in the SRAM device board compared to the those calculated by the QMD. This indicates that the capture reaction that happens farther away from the SV influences on the SEU occurrence compared to that in the simulation with the QMD. As a result, the MQMD enhanced the emitted d- and t-induced SEU. However, the increase of the total SEU cross-section was negligibly small because α has the main contribution to the SEU occurrence, and its spectrum was not improved in the present work.

The above observation suggests that the increase of the secondary ions in the high-energy region expanded the energy region of the negative muons, which affected the SEU occurrence. The accuracy of the nuclear reaction model influenced the SEU rate prediction at the ground level. In the present situation, the spectra of p, d, and t were not reproduced sufficiently well, and the α spectrum was not yet validated. Hence, further improvements of the spectra, especially in the high-energy region, are necessary to make a reliable SEU rate simulation framework.

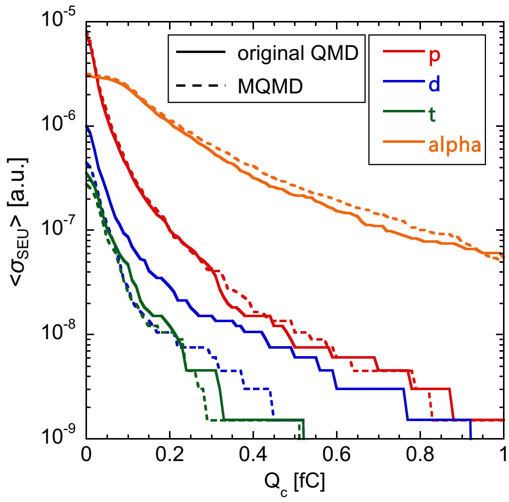

Figure 4.28: Comparison of the secondary p-, d-, t-, and α-induced mean SEU cross-section for the 65-nm SOTB SRAM calculated with QMD/GEM and MQMD/GEM. The muon was irradiated with an mean incident kinetic energy of 6.6 MeV. The calculation result with QMD/GEM is the same as the one in Figure 3.8; however, the H ion in Figure 3.8 was divided in p, d and t here.

4.6 Conclusion

The energy spectra of the protons, deuterons, and tritons emitted from the nuclear negative muon capture reaction on ^{nat}Si were successfully measured using the ΔE (0.325 mm-thick silicon)-E (25 mm-thick CsI(Tl)) telescope. The spectra of p and d in the energy range of 8-15 MeV and t spectrum were first measured in the present work.

First, the measured data were compared to those of the past works. The comparison demonstrated the consistency between the present and past data. Next, a benchmark test of the QMD/GEM and the MQMD/GEM implemented in the PHITS code was performed. The test indicated that the MQMD/GEM has higher yields of d and t compared to the QMD/GEM due to the implementation of the SCM similar to the simulation of the neutron-induced nuclear reaction. However, both models still significantly underestimated the spectra in the high-energy region. Next, we performed a comparison of the yield ratios of p to d and t with the neutron-induced nuclear reaction. The result suggested the similarity of the fundamental physical process of the deuteron emission from the muon and neutron reactions. Finally, the impact of the nuclear reaction models on the SEU simulation was examined. The MQMD enhanced the emitted d- and t-induced SEU. However, an increase of the total SEU cross-section was negligibly small. The examination suggested that further improvements of the simulated spectra are necessary to make a reliable SEU rate simulation system.

5 Summary and Conclusions

A modern and future information society is sustained by a great number of electronic equipment. The equipment that demands safety more than ever (e.g. autonomous driving, payment and medical application) is appearing. The semiconductor device is one of the most important infrastructures in our society. The main threat to the device reliability at the ground level is known as the secondary cosmic-ray-induced soft error. Among the cosmic-ray species, the muon has recently drawn attention as a new cause of the soft error due to the reduction of the critical charge of the SRAM. Many works on the muon-induced soft error have been reported since 2010. Moreover, the negative muon is presumed to have more significant effects on the occurrence of the soft error compared to the positive one in the previous work due to the secondary charged-particle emission from the nuclear capture reaction. However, the effect of the negative muon on soft error is not yet well understood because the experimental investigation has not been performed. Under these circumstances, the investigation on the negative muon induced SEU was performed with the experiment and simulation in this thesis. Furthermore, the fundamental nuclear data of the capture reaction were measured to improve the accuracy of the muon-induced soft error estimation at the ground level. In this thesis, two experiments were performed at two muon beam facilities and described in Chapters 2 and 4. These experiments were conducted by taking advantage of the two muon beams available in Japan which have different time structure.

Chapter 2 described the measurement of negative- and positive-induced SEU cross-sections for the 65-nm SOTB SRAM. The negative muon-induced SEU data for the deep-submicron technology SRAM were measured for the first time. The kinetic energy and the supply voltage dependence of the SEUs were measured in the incident muon kinetic energy range of 5.6-8.8 MeV. The nuclear muon capture reaction is unique for the negative muon, while the positive muon induces SEUs with only its direct ionization. Hence, the impact of the nuclear reaction on the SEU could be investigated by comparing the data of positive and negative muons. The nuclear negative muon capture reaction with the constituent atoms in the device caused SEUs considerably. Next, the measured data were compared with those of the previous works. The kinetic energy dependence of the SEU qualitatively agreed with the past experimental data of the positive muon-induced SEU. Moreover, we confirmed that our experimental data supported the negative muon-induced SEU simulation with the 65-nm SRAM performed in the previous work.

In Chapter 3, the experimental data for the 65-nm SOTB SRAM were analyzed with the PHITS-SV simulation to investigate the fundamental physical mechanism of the negative muon-induced SEU. The simulation reproduced the experimental kinetic energy dependence reasonably well by choosing the critical charge. Next, the species of the charged particles affecting the low-energy negative muon-induced SEUs were examined. The result indicated that hydrogen and helium ion has predominant contributions among all particles and ion species. Based on the analysis, the negative and positive muon-induced SEU rates for the 65-nm bulk and SOTB SRAMs in the terrestrial radiation environment were estimated by means of the PHITS-SV simulation. The estimation clearly showed the importance of the nuclear negative muon capture reaction on appropriate SEU rate prediction. In addition, the estimated SEU rate was compared to those of neutron. The muon SEU rates for the 65-nm SRAMs were almost negligibly small compared to the neutron SEU rates in the open-air radiation environment. Moreover, a muon transport simulation in the five-story concrete building was performed to investigate the indoor SEU rate. As a result, the muon SEU rate relatively increased up to 10% of the neutron one in on the first floor due to the difference of the attenuation effects of the muons and neutrons in the building.

Chapter 4 described the measurement of the energy spectra of the hydrogen isotopes generated via the nuclear muon capture reaction on ^{nat}Si. The experiment was performed using the M1 beam line of MuSIC-RCNP in Osaka University. A 0.1 mm-thick silicon active target was irradiated by the negative muon beam. The emitted protons, deuterons, and tritons from the silicon target were successfully measured using the two ΔE-E telescopes comprising a 0.325 mm-thick silicon detector and a 25 mm-thick CsI(Tl) detector. The energy spectra of the hydrogen isotopes were obtained in the energy range of 8-33 MeV. We measured the spectra of proton and deuteron in the energy range of 8-15 MeV and the triton spectrum for the first time. The measured spectra were compared to the existing experimental data and the proton spectrum estimated in the previous work. The comparison confirmed the consistency of the present and past data. Next, the benchmark test of the model calculation (QMD/GEM and MQMD/GEM) implemented in the PHITS code was performed. MQMD/GEM reproduced the experimental deuteron and triton spectra better than QMD/GEM especially in the relatively higher-energy region. However, a large discrepancy still existed between the experimental and simulated spectra. The model calculation was presumed to underestimate the spectra due to the small energy that a neutron gains at thr first process of the model calculation. Finally, the impact of the model selection on the SEU simulation was discussed using the PHITS-SV simulation. The emitted deuteron and triton-induced SEU cross-section increased approximately 30%, but the increase of the total SEU cross-section wass almost negligible.

Some issue remains for investigation in the future to establish a reliable simulation system of the muon-induced soft error at the ground level. First, the energy spectrum of the α-particle emitted from the nuclear muon capture reaction on silicon nuclei is required to more deeply understand the negative muon-induced soft error. The spectrum data are not yet available, while the α-particle is expected to provide predominant influence on the SEU occurrence among the secondary ions from the capture reaction, as mentioned in Chapter 3. Thus, the data of the α-particle and the spectra of the hydrogen isotopes measured in this thesis will be valuable in improving the model calculation accuracy. Therefore, more experimental data are necessary to establish a reliable simulation system. Note that only a few α-like events were observed during the experiment described in Chapter 4 due to low statistics and the high energy threshold of 25 MeV for α-particle. Next, the experimental SEU data for a more advanced-technology device with a fin field-effect transistor (Fin-FET) structure is required to investigate the effect of scaling on the negative muon-induced soft error. As mentioned in Chapter 4, our research group already measured the SEU cross-section for a 28-nm planar SRAM. In contrast, the FinFET SRAM has been commercialized with the technology node under a 22-nm technology. The effect of the negative muon on the FinFET SRAM is still unclear and should be investigated to predict the future trend of the muon-induced soft error.

A Appendix

A.1 Surface Coalescence Model (SCM)

Here, we briefly describe the SCM implemented to improve the QMD. In this model, a leading nucleon, which is ready to leave the composite nucleus, is assumed to be involved in the formation of light complex particles (LCPs). Figure A.1 shows a schematic drawing of the SCM. When the fast nucleon passes the border defined by a distance d outside the sphere of radius R_0, it is regarded as the leading nucleon. The following checks for formation and emission of LCPs are then performed. The candidate LCP is chosen when the following phase space condition is satisfied:

$$R_{im} \times P_{im} \leq h_0, \tag{A.1}$$

where R_{im} and P_{im} are the relative spatial and momentum coordinates, respectively, of the considered ith nucleon with respect to the intermediate cluster m. An additional constraint is that the center of mass of the cluster should be located far from the radius R_0 to ensure that the candidate cluster is formed in the surface layer region. Finally, the emitted LCP is determined with respect to the kinetic energy and the Coulomb barrier penetration:

$$\epsilon_c = \sum_{j=1}^{A_c} (E_j + V_j) + B_c, \tag{A.2}$$

where, ϵ_c is the kinetic energy of the LCP; E_j and V_j are the kinetic and potential energy of the constituent nucleon, respectively; A_c and B_c are the mass number and the binding energy of the LCP, respectively. The LCP will be emitted when the ϵ_c is positive. If the test for emission fails for all LCP candidates, the leading nucleon under consideration is emitted. d, h_0, and R_0 are adjustable parameters. d and h_0 are set to 2.3 fm and 260 MeV fm/c, respectively, with reference to [52], respectively. For the radius R_0, 3.1124 fm was chosen from the table of nuclear ground-state charge radii [75].

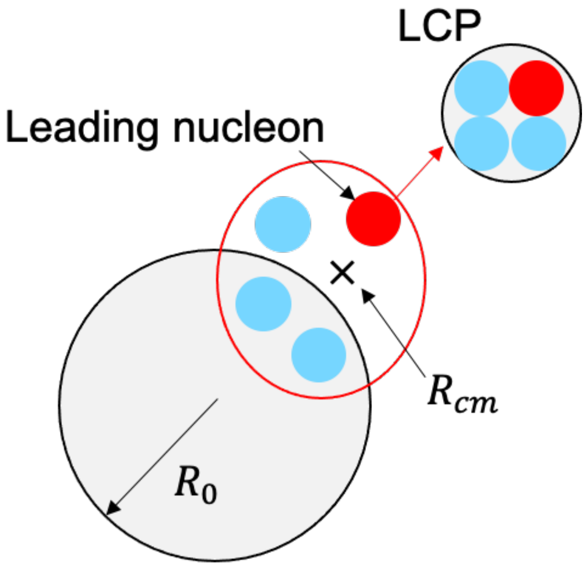

Figure A.1: Schematic drawing of Surface Coalescence Model (SCM).

References

1. Council for Science, Technology and Innovation Cabinet Office, Government of Japan. *The 5th Science and Technology Basic Plan* http://www8.cao.go.jp/cstp/kihonkeikaku/5honbun.pdf. Jan. 2016.

2. For example: R. Baumann. Soft errors in advanced computer systems. *IEEE Design Test of Computers* **22,** 258–266. ISSN: 0740-7475 (2005).

3. Dodd, P. E. & Massengill, L. W. Basic mechanisms and modeling of single-event upset in digital microelectronics. *IEEE Transactions on Nuclear Science* **50,** 583–602. ISSN: 0018-9499 (2003).

4. Ministry of Internal Affairs and Communications, Japan. *Information and Communications in Japan WHITE PAPER 2019* https://www.soumu.go.jp/johotsusintokei/whitepaper/ja/r01/pdf/index.html (in Japanese). 2019.

5. Sato, T. *EXPACS* https://phits.jaea.go.jp/expacs/jpn.html.

6. Sato, T. Analytical Model for Estimating Terrestrial Cosmic Ray Fluxes Nearly Anytime and Anywhere in the World: Extension of PARMA/EXPACS. *PLOS ONE* **10,** 1–33. https://doi.org/10.1371/journal.pone.0144679 (2015).

7. Sato, T. Analytical Model for Estimating the Zenith Angle Dependence of Terrestrial Cosmic Ray Fluxes. *PLOS ONE* **11,** 1–22. https://doi.org/10.1371/journal.pone.0160390 (2016).

8. Measday, D. The nuclear physics of muon capture. *Physics Reports* **354,** 243–409. ISSN: 0370-1573. http://www.sciencedirect.com/science/article/pii/S0370157301000126 (2001).

9. Sato, T. *et al.* Features of Particle and Heavy Ion Transport code System (PHITS) version 3.02. *Journal of Nuclear Science and Technology.* eprint: https://doi.org/10.1080/00223131.2017.1419890. https://doi.org/10.1080/00223131.2017.1419890 (2018).

10. Abe, S. & Sato, T. Implementation of muon interaction models in PHITS. *Journal of Nuclear Science and Technology* **54,** 101–110. eprint: https://doi.org/10.1080/00223131.2016.1210043. https://doi.org/10.1080/00223131.2016.1210043 (2017).

11. Niita, K. *et al.* Analysis of the (N,xN') reactions by quantum molecular dynamics plus statistical decay model. *Phys. Rev. C* **52,** 2620–2635. https://link.aps.org/doi/10.1103/PhysRevC.52.2620 (5 Nov. 1995).

12. Furihata, S. Statistical analysis of light fragment production from medium energy proton-induced reactions. *Nuclear Instruments and Methods in Physics Research Section B: Beam Interactions with Materials and Atoms* **171,** 251–258. ISSN: 0168-583X. http://www.sciencedirect.com/science/article/pii/S0168583X00003323 (2000).

13. Ziegler, J., Ziegler, M. & Biersack, J. SRIM - The stopping and range of ions in matter (2010). *Nuclear Instruments and Methods in Physics Research Section B: Beam Interactions with Materials and Atoms* **268,** 1818–1823. ISSN: 0168-583X. http://www.sciencedirect.com/science/article/pii/S0168583X10001862 (2010).

14. For example : P. Hazucha and C. Svensson. Impact of CMOS technology scaling on the atmospheric neutron soft error rate. *IEEE Transactions on Nuclear Science* **47,** 2586–2594. ISSN: 0018-9499 (2000).

15. JEDEC Solid State Technology Association. *Measurement and Reporting of Alpha Particle and Terrestrial Cosmic Ray-Induced Soft Errors in Semiconductor Devices* [Online]. Avialble: https://www.jedec.org/system/files/docs/JESD89A.pdf. Oct. 2006.

16. Telecommunication Standardization Sector of International Telecommunication Union. *Neutron irradiation test methods for telecommunication equipment* [Online]. Avialble: https://www.itu.int/rec/T-REC-K.130-201801-I/en. Jan. 2018.

17. Nippon Telegraph and Telephone Corporation. *"Soft error test service" commences to reproduce "soft errors" - abnormal operation of electronic equipment caused by cosmic rays* http://www.ntt.co.jp/news2016/1612e/161219a.html.

18. Ziegler, J. F. & Lanford, W. A. Effect of Cosmic Rays on Computer Memories. *Science* **206,** 776–788. ISSN: 0036-8075. eprint: http://science.sciencemag.org/content/206/4420/776.full.pdf. http://science.sciencemag.org/content/206/4420/776 (1979).

19. Dicello, J. F., McCabe, C. W., Doss, J. D. & Paciotti, M. The Relative Efficiency of Soft-Error Induction in 4K Static RAMS by Muons and Pions. *IEEE Transactions on Nuclear Science* **30,** 4613–4615. ISSN: 0018-9499 (1983).

20. Dicello, J. F. *et al.* Meson Interactions in NMOS and CMOS Static RAMs. *IEEE Transactions on Nuclear Science* **32,** 4201–4205. ISSN: 0018-9499 (1985).

21. Dicello, J. Microelectronics and microdosimetry. *Nuclear Instruments and Methods in Physics Research Section B: Beam Interactions with Materials and Atoms* **24-25,** 1044–1049. ISSN: 0168-583X. `http://www.sciencedirect.com/science/article/pii/S0168583X87803087` (1987).

22. Dicello, J., Paciotti, M. & Schillaci, M. An estimate of error rates in integrated circuits at aircraft altitudes and at sea level. *Nuclear Instruments and Methods in Physics Research Section B: Beam Interactions with Materials and Atoms* **40-41,** 1295–1299. ISSN: 0168-583X. `http://www.sciencedirect.com/science/article/pii/0168583X89906435` (1989).

23. Livingston, M. LAMPF, A Nuclear Research Facility. *Los Alamos National Laboratory report* **9,** LA-6878–MS (8 Sept. 1977).

24. Sierawski, B. D. *et al.* Muon-Induced Single Event Upsets in Deep-Submicron Technology. *IEEE Transactions on Nuclear Science* **57,** 3273–3278. ISSN: 0018-9499 (2010).

25. Sierawski, B. D. *et al. Effects of scaling on muon-induced soft errors* in *Proc. 2011 International Reliability Physics Symposium* (Apr. 2011), 3C.3.1–3C.3.6.

26. Sierawski, B. D. *et al. Bias dependence of muon-induced single event upsets in 28 nm static random access memories* in *Proc. 2014 IEEE International Reliability Physics Symposium* (June 2014), 2B.2.1–2B.2.5.

27. Gasiot, G., Soussan, D., Autran, J. L., Malherbe, V. & Roche, P. *Muons and thermal neutrons SEU characterization of 28nm UTBB FD-SOI and Bulk eS-RAMs* in *Proc.2015 IEEE International Reliability Physics Symposium* (Apr. 2015), 2C.2.1–2C.2.5.

28. Seifert, N., Jahinuzzaman, S., Velamala, J. & Patel, N. *Susceptibility of planar and 3D tri-gate technologies to muon-induced single event upsets* in *Proc. 2015 IEEE International Reliability Physics Symposium* (Apr. 2015), 2C.1.1–2C.1.6.

29. Serre, S. *et al. Effects of Low Energy Muons on Electronics: Physical Insights and Geant4 Simulation* in *Proc. 13th European Conference on Radiation and its Effects on Components and Systems (RADECS 2012)* (Sept. 2012).

30. Miyake, Y. *et al.* J-PARC muon source, MUSE. *Nuclear Instruments and Methods in Physics Research Section A: Accelerators, Spectrometers, Detectors and Associated Equipment* **600,** 22–24. ISSN: 0168-9002. http://www.sciencedirect.com/science/article/pii/S0168900208016471 (2009).

31. Miyake, Y. *et al.* J-PARC Muon Facility, MUSE. *Physics Procedia* **30,** 46–49. ISSN: 1875-3892. http://www.sciencedirect.com/science/article/pii/S1875389212012230 (2012).

32. Matsumoto, Y. *et al. A New DC Muon Beam Line at RCNP, Osaka University* in *Proc. 6th International Particle Accelerator Conference (IPAC)* (2015), 2537–2540.

33. Nagamiya, S. Introduction to J-PARC. *Progress of Theoretical and Experimental Physics* **2012,** 02B001. eprint: /oup/backfile/content_public/journal/ptep/2012/1/10.1093_ptep_pts025/1/pts025.pdf. http://dx.doi.org/10.1093/ptep/pts025 (2012).

34. Morita, Y. *et al. Smallest V_{th} variability achieved by intrinsic silicon on thin BOX (SOTB) CMOS with single metal gate* in *Proc.2008 Symposium on VLSI Technology* (June 2008), 166–167.

35. Hirokawa, S., Harada, R., Hashimoto, M. & Onoye, T. Characterizing Alpha- and Neutron-Induced SEU and MCU on SOTB and Bulk 0.4-V SRAMs. *IEEE Transactions on Nuclear Science* **62,** 420–427. ISSN: 0018-9499 (2015).

36. Hsieh, C. M., Murley, P. C. & O'Brien, R. R. A field-funneling effect on the collection of alpha-particle-generated carriers in silicon devices. *IEEE Electron Device Letters* **2,** 103–105. ISSN: 0741-3106 (1981).

37. Ito, T. *et al.* Online full two-dimensional imaging of pulsed muon beams at J-PARC MUSE using a gated image intensifier. *Nuclear Instruments and Methods in Physics Research Section A: Accelerators, Spectrometers, Detectors and Associated Equipment* **754.** ISSN: 0168-9002. http://www.sciencedirect.com/science/article/pii/S0168900214003921 (2014).

38. Nagamine, K. *Introductory Muon Science* (Cambridge University Press, 2003).

39. Watanabe, R., Fukui, M., Ohtsubo, H. & Morita, M. Angular Distribution of Electrons in Bound Muon Decay. *Progress of Theoretical Physics* **78,** 114–122. ISSN: 0033-068X. eprint: https://academic.oup.com/ptp/article-pdf/78/1/114/5437711/78-1-114.pdf. https://doi.org/10.1143/PTP.78.114 (July 1987).

40. Mahara, T. *et al.* Irradiation Test of 65-nm Bulk SRAMs With DC Muon Beam at RCNP-MuSIC Facility. *IEEE Transactions on Nuclear Science* **67,** 1555–1559 (2020).

41. Liao, W. *et al.* Measurement and Mechanism Investigation of Negative and Positive Muon-Induced Upsets in 65-nm Bulk SRAMs. *IEEE Transactions on Nuclear Science* **65,** 1734–1741 (2018).

42. Trippe, J. M. *et al.* Predicting Muon-Induced SEU Rates for a 28-nm SRAM Using Protons and Heavy Ions to Calibrate the Sensitive Volume Model. *IEEE Transactions on Nuclear Science* **65,** 712–718 (2018).

43. Tosaka, Y., Kanata, H., Satoh, S. & Itakura, T. Simple method for estimating neutron-induced soft error rates based on modified BGR model. *IEEE Electron Device Letters* **20,** 89–91. ISSN: 0741-3106 (1999).

44. Hirokawa, S., Harada, R., Sakuta, K., Watanabe, Y. & Hashimoto, M. *Multiple sensitive volume based soft error rate estimation with machine learning* in *Proc. 16th European Conference on Radiation and Its Effects on Components and Systems (RADECS 2016)* (Sept. 2016).

45. Hashimoto, M., Liao, W. & Hirokawa, S. *Soft error rate estimation with TCAD and machine learning* in *Proc. 2017 International Conference on Simulation of Semiconductor Processes and Devices (SISPAD)* (Sept. 2017), 129–132.

46. Abe, S. *et al.* Multi-Scale Monte Carlo Simulation of Soft Errors Using PHITS-HyENEXSS Code System. *IEEE Transactions on Nuclear Science* **59,** 965–970. ISSN: 0018-9499 (2012).

47. Harada, R. *et al.* Angular Dependency of Neutron-Induced Multiple Cell Upsets in 65-nm 10T Subthreshold SRAM. *IEEE Transactions on Nuclear Science* **59,** 2791–2795. ISSN: 0018-9499 (2012).

48. Abe, S. & Watanabe, Y. Analysis of Charge Deposition and Collection Caused by Low Energy Neutrons in a 25-nm Bulk CMOS Technology. *IEEE Transactions on Nuclear Science* **61,** 3519–3526. ISSN: 0018-9499 (2014).

49. Akylas, V. & Vogel, P. Muonic atom cascade program. *Computer Physics Communications* **15,** 291–302. ISSN: 0010-4655. `http://www.sciencedirect.com/science/article/pii/0010465578900991` (1978).

50. Suzuki, T., Measday, D. F. & Roalsvig, J. P. Total nuclear capture rates for negative muons. *Phys. Rev. C* **35,** 2212–2224. `https://link.aps.org/doi/10.1103/PhysRevC.35.2212` (6 1987).

51. Degtyarenko, P., Kossov, M. & Wellisch, H. *Chiral invariant phase space event generator: III. Modeling of real and virtual photon interactions with nuclei below pion production threshold* tech. rep. (Thomas Jefferson National Accelerator Facility, Newport News, VA (US), 2000).

52. Watanabe, Y. & Kadrev, D. *Extension of quantum molecular dynamics for production of light complex particles in nucleon-induced reactions* in *International Conference on Nuclear Data for Science and Technology 2007* (2008), 1–4.

53. Abe, S., Ogata, R. & Watanabe, Y. Impact of Nuclear Reaction Models on Neutron-Induced Soft Error Rate Analysis. *IEEE Transactions on Nuclear Science* **61,** 1806–1812 (2014).

54. Butts, J. J. & Katz, R. Theory of RBE for Heavy Ion Bombardment of Dry Enzymes and Viruses. *Radiation Research* **30,** 855–871. eprint: `http://www.rrjournal.org/doi/pdf/10.2307/3572151`. `http://www.rrjournal.org/doi/abs/10.2307/3572151` (1967).

55. Schwank, J., Ferlet-Cavrois, V., Shaneyfelt, M., Paillet, P. & Dodd, P. E. Radiation effects in SOI technologies. *IEEE Transactions on Nuclear Science* **50,** 522–538. ISSN: 0018-9499 (2003).

56. Abe, S.-i. *et al. Impact of Hydrided and Non-Hydrided Materials Near Transistors on Neutron-Induced Single Event Upsets* in *2020 IEEE International Reliability Physics Symposium (IRPS)* (2020), 1–7.

57. Abe, S. & Sato, T. *Shielding effect on secondary cosmic-ray neutron- and muon-induced soft errors* in *2016 16th European Conference on Radiation and Its Effects on Components and Systems (RADECS)* (2016), 1–5.

58. Liao, W. *et al. Negative and Positive Muon-Induced SEU Cross Sections in 28-nm and 65-nm Planar Bulk CMOS SRAMs* in *2019 IEEE International Reliability Physics Symposium (IRPS)* (2019), 1–5.

59. Seifert, N. *et al.* Soft Error Rate Improvements in 14-nm Technology Featuring Second-Generation 3D Tri-Gate Transistors. *IEEE Transactions on Nuclear Science* **62,** 2570–2577 (2015).

60. Lifshitz, M. & Singer, P. Charged-Particle Emission Following Muon Capture in Complex Nuclei. *Phys. Rev. Lett.* **41,** 18–21 (1 July 1978).

61. Lifshitz, M. & Singer, P. Nuclear excitation function and particle emission from complex nuclei following muon capture. *Phys. Rev. C* **22,** 2135–2150 (5 Nov. 1980).

62. Morinaga, H. & Fry, W. Nuclear capture of negative μ mesons in photographic emulsions. *Il Nuovo Cimento (1943-1954)* **10,** 308–318 (1953).

63. Kotelchuck, D. & Tyler, J. V. Search for a Conserved-Vector-Current Mechanism in the Emission of Protons from μ^- Stars in Emulsion. *Phys. Rev.* **165,** 1190–1194 (4 Jan. 1968).

64. Heusser, G. & Kirsten, T. Radioisotope production rates by muon capture. *Nuclear Physics A* **195,** 369–378. ISSN: 0375-9474 (1972).

65. Wyttenbach, A. *et al.* Probabilities of muon induced nuclear reactions involving charged particle emission. *Nuclear Physics A* **294,** 278–292. ISSN: 0375-9474 (1978).

66. Gaponenko, A. *et al.* Charged-particle spectra from μ- capture on Al. *Physical Review C* **101,** 035502 (2020).

67. Sobottka, S. E. & Wills, E. L. Energy Spectrum of Charged Particles Emitted Following Muon Capture in Si^{28}. *Phys. Rev. Lett.* **20,** 596–598. https://link.aps.org/doi/10.1103/PhysRevLett.20.596 (12 Mar. 1968).

68. Budyashov, Y. G., Zinov, V., Konin, A., Mukhin, A. & Chatrchyan, A. Charged Particles from the Capture of Negative Muons by the Nuclei ^{28}Si, ^{32}S, ^{40}Ca and ^{64}Cu. *Journal of Experimental and Theoretical Physics* **33,** 11–15 (July 1971).

69. Hungerford, V. Comments on Proton Emission after Muon Capture. arXiv: 1803.08403 [nucl-ex] (Mar. 2018).

70. RCNP homepage. http://www.rcnp.osaka-u.ac.jp/.

71. Lifshitz, M. & Singer, P. Meson-exchange currents and energetic particle emission from μ^- capture. *Nuclear Physics A* **476,** 684–700. ISSN: 0375-9474. http://www.sciencedirect.com/science/article/pii/0375947488903302 (1988).

72. Kossov, M. V. Chiral invariant phase space event generator Nuclear muon capture at rest. *The European Physical Journal A* **33,** 7–10 (2007).

73. Bernabéu, J., Ericson, T. & Jarlskog, C. Muon capture at large energy transfer. *Physics Letters B* **69,** 161–166. ISSN: 0370-2693. http://www.sciencedirect.com/science/article/pii/0370269377906347 (1977).

74. Benck, S., Slypen, I., Meulders, J.-P., Corcalciuc, V. & Chadwick, M. B. Fast Neutron–Induced Emission of Light Charged Particles on Aluminum (E_n = 25 to 55 MeV). *Nuclear Science and Engineering* **140,** 86–95 (2002).

75. Angeli, I. & Marinova, K. Table of experimental nuclear ground state charge radii: An update. *Atomic Data and Nuclear Data Tables* **99,** 69–95. ISSN: 0092-640X. http://www.sciencedirect.com/science/article/pii/S0092640X12000265 (2013).

Acknowledgments

This work was carried out at the Department of Advanced Energy Engineering Science, Interdisciplinary Graduate School of Engineering Sciences, Kyushu University, under the supervision of Professor Yukinobu Watanabe. I would like to express a gratitude to many people for their help in the present work.

First of all, I would like to express my deepest gratitude to Professor Yukinobu Watanabe for supervising me enthusiastically. His guidance and fruitful advise always led me to the achievements of the researches. Moreover, I have learned a lot from him, such as sincere attitude for researches, a sense of responsibility of a researcher, and so on, in addition to the contents of the research itself. I will keep learning and studying hard by making use of the knowledge and experiences received from him.

My great thanks are also expressed to Professors Hironao Sakaki, Tsuyoshi Yoshitake, and Kenya M. Kubo for careful reading of this manuscript and valuable comments.

I also wish to thank very much Professor Masanori Hashimoto and Assistant Professor Wang Liao for providing the device board, their helpful comments about device physics and supports on the soft error experiments and data analysis.

I would like to express my great thanks to Professor Yasuhiro Miyake, Dr. Motonobu Tampo, Koji Hamada, and Shogo Doiuchi at KEK for great supports on the experiment at MUSE, providing the high quality muon beam and advise on the data analysis.

I would like to thank very much Dr. Shin-ichiro Abe for helpful advise on the simulation of transport and nuclear reaction of muons.

I would like to appreciate Assistant Professor Megumi Niikura, Takeshi Y. Saito, Dr. Daisuke Suzuki, Yoshitaka Kawashima, Dr. Dai Tomono, and Assistant Professor Akira Sato for supports on the experiment at MuSIC. I have received a lot of knowledge on nuclear reaction experiments from them. Thanks to their collaboration, the contents of this thesis were enriched.

My appreciation also goes to Assistant Professor Shoichiro Kawase for valuable comments on the experimental analysis and the consideration on the results.

I am greatly thankful to Dr. Keita Nakano for his fruitful advise on writing this thesis and great co-operation on the experiment.

It has been a big pleasure for me to work hard together with Takumi Mahara, Jyunya Kuroda, Takuya Murota, Yu Horai, Naoki Yamaguchi, Hiroya Fukuda, Kodai Tamura, and Hirotaka Tanaka at soft error research group in our laboratory.

My thanks are expressed to Rumiko Koga for her help in office work. I also would like to thank all other members in the Watanabe-Kin laboratory, Associate Professor Tadahiro Kin, Hikaru Sato, Katsumi Aoki, Hayato Takeshita, Tomoko Kamei, Hamid Basiri, Miyuki Uematsu, Naoya Okamoto, Yuji Shinjo, Tatsuhiko Miyatake, Masaya Yamaguchi, Mary Alfonse, Misaki Saitsu, Ryohei Takahashi, Yuichiro Takaya, and Wataru Sekiguchi.

This work was supported by JST-OPERA Program Grant Number JPMJOP172, JAPAN, Grant-in-Aid for Scientific Research (B) (No.16H03906) and JSPS Fellows (No.19J12649) from the Japan Society for the Promotion of Science (JSPS), and Kyushu University Platform of Inter/Transdisciplinary Energy Research (Q-PIT). The muon experiment described in Chapter 2 was performed at Materials and Life Science Experimental Facility of the J-PARC under user programs Nos. 2016B0046 and 2017A0139.

Finally, I would like to express my gratitude to my family for permitting me to continue the research at the graduate school and supporting me during these five years. Without their support, I could not complete this work.